Title

Digital Linearization and Wideband Measurements in Optical Links

Permalink

https://escholarship.org/uc/item/464955x7

Author

Lam, Daniel

Publication Date

2014

Peer reviewed|Thesis/dissertation

UNIVERSITY OF CALIFORNIA

Los Angeles

Digital Linearization and

Wideband Measurements

in Optical Links

A dissertation submitted in partial satisfaction of the

requirements for the degree Doctor of Philosophy

in Electrical Engineering

by

Daniel Wai Chuen Lam

2014

ABSTRACT OF THE DISSERTATION

Digital Linearization and

Wideband Measurements

in Optical Links

by

Daniel Wai Chuen Lam

Doctor of Philosophy in Electrical Engineering

University of California, Los Angeles, 2014

Professor Bahram Jalali, Co-Chair

Professor Asad M. Madni, Co-Chair

Optical fiber networks have been in use for many decades to transport large amounts of data across long distances. Internet traffic grows at an exponential rate and demand for increased bandwidth and faster data rates is higher than ever. Radio frequency over fiber is used for a plethora of applications such as providing wireless access to remote and rural areas, phased array radars, and cable television to name a few. As signals are transmitted over longer distances, nonlinearities are incurred which degrades the performance and sensitivity of the link. Moreover as the data rates increase, it becomes a challenge to measure and monitor the signal integrity.

This dissertation will cover two main topics: digital broadband linearization and performing wideband high speed measurements using time-stretch technology. Over the last few

years there has been considerable interest in reducing the intermodulation distortions in optical links. The intermodulation distortions are caused by the nonlinear transfer function of the optical link. To reduce the nonlinearities, linearization of the optical link is performed. A novel digital post-processing algorithm has been developed to suppress nonlinearities and increase the dynamic range of the link. Digital broadband linearization algorithm has been implemented and demonstrated a record 120 dB.Hz$^{2/3}$ Spurious Free Dynamic Range (SFDR) over 6 GHz of bandwidth and is shown to suppress third order intermodulation products by 35 dB. By reducing the nonlinearities and improving SFDR, we have increased the sensitivity of the receiver. Afterwards, simulation of the real-time implementation of the digital broadband linearization algorithm onto a field-programmable gate array was performed by designing the architecture and translating the code into Verilog HDL. Simulations on collected data show comparable results in both Matlab and iSim which were used to evaluate the performance.

In the second part of this dissertation, two applications using time-stretch are demonstrated: ultra-wideband instantaneous frequency estimation and high speed signal analysis measurements. By combining time-stretch technology and windowing and quadratic interpolation, ultra-wideband frequency measurements with improved frequency estimation are demonstrated. Moreover, multiple signal measurements are performed, and the frequency resolution can be tuned to measure signals close together. Lastly, time-stretch is used for measuring high speed signal integrity parameters such as bit error rate, jitter, and rise and fall times by taking advantage of the high sampling throughput and the ability to generate and analyze eye diagrams. In addition, we were able to integrate this technology into a test-bed for aggregate optical networks and use it for an optical performance monitoring application.

The dissertation of Daniel Wai-Chuen Lam is approved.

Carlos Portera-Cailliau

Asad M. Madni, Committee Co-chair

Bahram Jalali, Committee Co-chair

University of California, Los Angeles

2014

For my family

And for all those who persevere and strive for their dreams…

TABLE OF CONTENTS

LIST OF FIGURES

LIST OF TABLES

ACKNOWLEDGMENTS

This degree would not be possible without the encouragement, support, and mentoring by many individuals. First, I would like to thank both of my advisors, Professor Bahram Jalali and Professor Asad Madni, for giving me the opportunity to study under them and work on really interesting and cutting edge projects. Both have been great supportive advisors who have pushed me and guided me to new heights as a professional. I am extremely grateful and appreciative of the time they spent and the advice they have shared with me over the years. I could not be any luckier to study under two world renowned professors and am proud to be their student.

I thank Professor Bahram Jalali for accepting me into his group and giving me an opportunity to pursue my degree at UCLA. Over the years, he has been a great support to me academically and professionally and has provided me with many opportunities to expand my knowledge and develop my skills through various projects. He has also taught me to always look for business opportunities. Two things I take away are that we should always be flexible in our approach to problems just like how time isn't always rigid and that "there is no free lunch."

I thank Professor Asad Madni for his desire to mentor me. His passion, energy, drive, and knowledge has helped me grow leaps and bounds. His dedication for his students is evident in the time he spends with us and how he pushes us to succeed. Under his tutelage, I have learned so much and to always continue learning and find ways to continually improve the world around me. I am grateful and appreciative of his insight and feedback for this body of work would not have been as successful without them.

I would like to thank Professor Oscar Stafsudd, Professor Frank Chang, and Professor Carlos Portera-Cailliau for taking the time to serve on my committee and providing me feedback.

I want to thank my lab mates who I have gotten to know and became great friends with over the years. They have helped me through useful discussions and for spending long hours in the lab with me. Without them, my time at UCLA would not have been as exciting or enjoyable. I especially want to thank Dr. Ali Fard, Dr. Peter DeVore, Dr. Brandon Buckley, and Cejo Konuparamban Lonappan. Getting to know these gentlemen in and out of the lab has been a blessing to me, and I will cherish the times we have spent together.

I am grateful to Northrop Grumman Aerospace Systems for giving me the opportunity to pursue a higher degree through their fellowship program. Without their support and funding, this would not have been possible.

I thank all my mentors and teachers throughout my life and during my career. Be it a small piece of advice or just taking the time to teach me, all these experiences have shaped me into the person I am today. I especially want to thank Professor Galina Khitrova and the late Professor Hyatt Gibbs for giving me my first opportunity to work in an optical lab and helping me find my passion for optics.

I am grateful for my friends who have given me moral support throughout these many years.

Most importantly, I want to thank my entire family. Their love, support, and encouragement gave me the strength to keep persevering to complete this degree. They celebrated my accomplishments with me and stood by me when I was discouraged. I especially thank my parents for providing me with so many opportunities in life and instilling in me the value of a good education. Thank you for always being there for me.

VITA

2011-2014	Graduate Student Researcher Department of Electrical Engineering University of California, Los Angeles Los Angeles, California, USA
2009-Present	Engineer Northrop Grumman Aerospace Systems El Segundo, California, USA
2008-2009	Master of Science in Electrical Engineering Stanford University Stanford, California, USA
2008	Engineering Intern Northrop Grumman Space Technologies Redondo Beach, California, USA
2007	Engineering Intern Raytheon Space and Airborne Systems El Segundo, California, USA
2005-2008	Undergraduate Research Assistant The University of Arizona College of Optical Sciences Tucson, Arizona, USA
2004-2008	Bachelor of Science in Optical Sciences and Engineering with Honors Minors in Electrical Engineering and Mathematics, Magna Cum Laude The University of Arizona Tucson, Arizona, USA

AWARDS

2010	Northrop Grumman Aerospace Systems Fellowship
2004-2008	Raytheon Scholars Program
2004-2008	Dean's List (GPA 3.5-3.999) and Dean's List with Distinction (GPA 4.0)
2004-2008	UA Provost Scholarship
2004-2008	UA Spirit of Discovery Award

PUBLICATIONS AND PRESENTATIONS

D.Lam, C. K. Lonappan, B. Buckley, A. M. Madni, and B. Jalali, "Real-time Optical Performance Monitoring using Time-Stretch Technology," CIAN lecture series, Sept 2014.

D.Lam, B. W. Buckley, C. K. Lonappan, A. M. Madni, and B. Jalali, "Ultra-wideband Instantaneous Frequency Estimation," (To be published).

C. K. Lonappan, B. Buckley, J. Adam, **D. Lam**, A. M. Madni, and B. Jalali, "Time-Stretch Accelerated Processor for Real-time, In-service, Signal Analysis," IEEE Conference on Signal and Information Processing, December 3-5, 2014 (Accepted).

C. K. Lonappan, **D. Lam**, B. Buckley, P.T.S. DeVore, D. Borlaug, A. M. Madni, B. Jalali, M. Chitgarha, A. Almaiman, A. E. Willner, M. Wang, A. Ahsan, B. Birand, G. Zussman, K. Bergman, W. Mo, M. Yang, A. Gautham, S. Albanna, J. Wissinger, D. Kilper, "Optical Performance Monitoring for Agile Optical Networks," Poster presentation at Center for Integrated Access Networks (CIAN) Site Visit, May 2014.

C. K. Lonappan, **D. Lam**, P.T.S. DeVore, D. Borlaug, B. W. Buckley, A. M. Madni, and B. Jalali, "Photonic Time-Stretch for Real-time In-service Performance Monitoring of Next Generation Optical Networks," Poster presentation for CIAN Industrial Affiliates Board meeting, 2014.

P. DeVore, **D. Lam**, C. Kim, and B. Jalali, "Boosting Electrooptic Modulators for Optical Communications," in Frontiers in Optics 2013, I. Kang, D. Reitze, N. Alic, and D. Hagan, eds., OSA Technical Digest (online) (Optical Society of America, 2013), paper FW48.

D. Lam, A. Fard, B. Buckley, and B. Jalali, "Digital broadband linearization of optical links," Optics Letters, 38, 446-448 (2013).

D. Lam, A. Fard, and B. Jalali, "Digital broadband linearization of analog optical links," IEEE Photonics Conference, 23-27 Sept. 2012.

J. Hendrickson, B. C. Richards, J. Sweet, S. Mosor, C. Christenson, **D. Lam**, G. Khitrova, H. M. Gibbs, T. Yoshie, A. Scherer, O. B. Shchekin, and D. G. Deppe, "Quantum dot photonic-crystal-slab nanocavities: quality factors and lasing", Phys. Rev. B 72, 193303 (2005).

Chapter 1

Introduction

1.1   Optical Fiber Links

Optical fiber networks have been used for many decades to transport large amounts of data across long distances. These networks help connect the world and bring wireless access to remote locations cheaply. Radio frequency over fiber is an enabling technology used for an array of applications such as providing wireless access to remote and rural areas, phased array radars, and cable television to name a few. Using optical links provides significant advantages over current coaxial cables [1]-[3]. Optical links have much lower attenuation than other media. Using optical fibers allows transmission of signals further, thereby reducing the number of repeaters along the way. The optical fiber link has lower complexity, typically a link just consists of an optical to electrical converter, amplifiers, and an antenna. This means that we could create a central location and connect all the antennas to this station which simplifies the overall architecture. Additionally, having a simpler architecture reduces cost since there will be reduced power consumption and lower cost to the infrastructure. Moreover, fiber optics can support speeds that are greater than those available today, and they can handle faster speeds offered by

future generations. This means that they do not need to be upgraded as frequently which also saves on cost [1]-[4].

With increased demand for wireless access points, many locations need to be connected to these fiber links. There is a need for transporting data to farther remote areas or areas inaccessible via wireless. As signals are transmitted over longer distances, the optical links begin to suffer from nonlinearities and distortion that degrade the performance of the link [1]. These distortions, known as intermodulation distortion products, can produce crosstalk in the link which causes interference for signals in other bands. These eventually degrade the entire optical link performance and limit the data rate and distance of signal propagation. Chapter 3 presents a digital post-processing algorithm that is capable of reducing nonlinearities and increasing the spurious free dynamic range of an optical link. This is an improvement over current techniques because it is a post-processing technique which does not require additional hardware and can be implemented onto a real-time system. Previous techniques, by contrast, require additional hardware and can only reduce the nonlinearities in a limited bandwidth. Additionally, this algorithm regenerates the nonlinearities which obviates the need for excessive bandwidth.

1.2   High Speed Analog-to-Digital Converters

Internet traffic continues to grow at an exponential rate, and next generation networks need to be able to handle the increasing bandwidth every year. According to Cisco [5], the annual global IP traffic will surpass the zettabyte threshold in 2016. Over the past five years, global IP traffic has grown fivefold and is expected to grow threefold in the next five years. Most of the growth has been fueled by the explosion of social media, online gaming, video streaming, and cloud storage. Furthermore, metro traffic is expected to surpass long-haul traffic by 2015 and will account for

more than 62 percent of total IP traffic by 2018 [5]. This large growth in metro traffic is due in part to content delivery services which bypass the long-haul links and deliver their content directly to regional and metro networks. These content delivery services are expected to carry over half of the Internet traffic by 2018 [5].

As the number of users and demand for content increases, the data rate continues to increase in order to meet demand. However, due to high speed signals, it becomes increasing difficult and challenging for engineers to develop electronic hardware capable of supporting these speeds. There has been a lot of development over the past two decades on developing technology to send more data through optical fibers. For example, the data rate is increased through different optical techniques like optical time division multiplexing or using denser wavelengths. Research is ongoing on making the optical components, such as the electro-optic modulators faster. Next generation modulators have demonstrated the ability to achieve speeds of over 100 GHz [6].

On the receiving end, there is a need for high speed analog-to-digital converters (ADC) to convert this information into digital format. Walden has taken a survey of different high speed digitizers and shown that as the bandwidth increases, the resolution decreases [7],[8]. This is because as the bandwidth of the digitizer increases, the amount of noise increases as well thereby lowering the signal to noise ratio. Several architectures have been developed to increase the speed of the digitizers, such as interleaving multiple ADCs. However, the main issue with this architecture is the timing and ability to interleave the data. A small timing error during the interleaving process can create timing errors in the final data resulting in jitter [9]. Additionally, these high speed ADCs comprised of several interleaved ADCs are large rack mount units that consume a considerable amount of energy.

3

Using time-stretch technology, we can perform high speed measurements and reduce the size and energy consumption of the system. The time-stretch concept was first demonstrated in 1998 [10] and has since been used for an array of applications. One application is the time-stretch analog-to-digital converter (TS-ADC) [11],[12]. The unique advantage of this technology is that it can slow down ultrafast signals in time and allow a slower, higher resolution ADC to sample the signal. By using a slower ADC for sampling, we can maintain a higher resolution as opposed to using a faster ADC with lower effective number of bits (ENOB) [11],[12]. For example, a 40 GHz signal would appear as a 2 GHz signal with a stretch factor of 20. By using this technique, the TS-ADC is able to break past the Walden curve shown in Figure 1.1 and set a record 7.2 ENOB over 10 GHz of bandwidth [13].

Time-stretch has been used to capture ultrafast signals. In one demonstration, a 95 GHz tone was sampled at an effective sampling rate of 10 Terasamples/second [14]. By expanding this technology into two-dimensions, ultrafast images can be captured. A new type of bright-field camera known as time-stretch microscopy [15] has demonstrated imaging of cells with record shutter speed and throughput leading to detection of rare breast cancer cells in blood with one-in-a-million sensitivity [16]. Used for single-shot real-time spectroscopy, the time stretch technology led to the discovery of optical rogue waves, bright and random flashes of white light that result from complex nonlinear interactions in optical fibers [17]. Time-stretch also led to the development of a fluorescence imager with record imaging speeds [18].
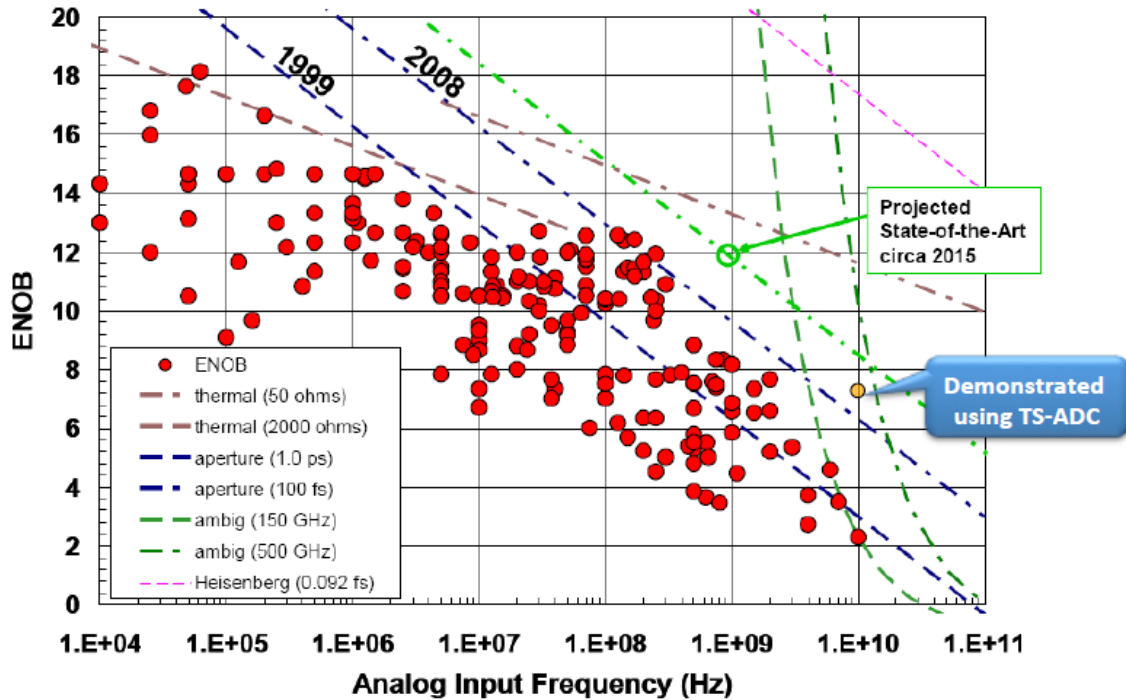
Figure 1.1. Resolution of state-of-the-art electronic ADCs versus input bandwidth [8]. The TS-ADC is able to demonstrate 7.2 ENOB over 10 GHz of bandwidth [13] which shows photonics can help in overcoming current bandwidth limitations.

1.3 Wideband High Speed Applications

As stated in the previous section, time-stretch can be applied to perform high speed, wide bandwidth measurements. Two of those applications are addressed in this thesis: ultra-wideband instantaneous frequency estimation and using time-stretch for signal integrity measurements in optical communication networks. In defense applications, it is important to monitor the frequency spectrum over a very wide bandwidth. Sweeping across bandwidths of several gigahertz would take several seconds and quick transient signals would not be measured. A new architecture known as time-stretch instantaneous frequency measurement (TS-IFM) receiver is

introduced that can overcome some of the limitations of current IFMs. The TS-IFM can estimate multiple frequencies with improved accuracy in a wide bandwidth with fast sweep times. The improved frequency estimation is performed by windowing the time domain data and performing quadratic interpolation in the frequency domain [19]. Wideband single tone frequency estimation across 40 GHz of bandwidth has been demonstrated and this can be extended to multiple frequency estimation as well. The TS-IFM is discussed in detail in Chapter 5.

Time-stretch technology can also be used for high speed signal integrity measurements for optical networks. Using the time-stretch enhanced recorder (TiSER) and a field programmable gate array (FPGA) for real-time processing, fast signals can be captured with high fidelity due to TiSER's high temporal resolution. Chapter 6 describes how we can use time-stretch to capture rising and falling edges which provides more data points than a conventional Tektronix 50 GSa/s real-time oscilloscope. Due to TiSER's high sampling throughput and by overlapping the recorded signals, eye diagrams can be generated. A major development, which will not be discussed in detail in this thesis, is TiSER's ability to generate eye diagrams in real-time which allows for rapid analysis of the eye for bit error rate, rise time, fall time, and jitter measurements. This information can immediately be used to provide feedback to a software defined network (SDN). Chapter 6 describes how the eye diagram is analyzed to extract the bit error rate, rise and fall times, and jitter. Chapter 7 discusses how TiSER was integrated into the Center for Integrated Access Networks Test-bed for Optical Aggregate Networks. In this test-bed, TiSER acts as an optical performance monitor for a SDN which is able to perform measurements and analyze the eye diagram in order to determine the health of the optical network. Depending on the information provided by TiSER, real-time adjustments can be made by the SDN control plane to optimize network performance.

6

Chapter 2

Background

Many of the topics discussed in this thesis involve performing high speed measurements using optical fiber links. This chapter presents some of the fundamental concepts so that the reader is able to gain a better appreciation of the work presented later in this thesis and to gain an appreciation of the challenges faced and the approach used in solving those problems.

2.1 Historical Perspective

Fiber optic systems are ubiquitous in modern society and the demand for high speed internet continues to grow. Fiber optic networks have stimulated the development of cities, promoted economic growth, and connected people around the world. Communication systems transmit information from one place to another, whether separated by a few kilometers or by great transoceanic distances. Optical communication systems use light to transmit information by modulating information onto a high carrier frequency.

The precursor to the fiber optic link, called the photophone, was developed in 1880 by Alexander Graham Bell and his assistant Charles Sumner Tainter [20]-[22]. The device allowed for the transmission of sound on a beam of light. Using the photophone, the first wireless voice transmission was made some 213 meters apart, and this was different than the telephone because it required the modulation of light instead of modulated voltage carried over a conductive wire circuit. Bell deemed it his greatest invention, but the photophone would not be very practical until advances in lasers and optical fiber technology permitted the secure transport of light. Until 1950, the main issue with realizing optical waves as a carrier was there was neither a coherent optical source nor a suitable transmission medium for transporting light.

Optical communications was realized when the laser was invented which solved the coherent optical source issue. However, there was no low attenuation medium as the glass fibers during this time had losses around 1000 dB/km [22]-[24]. The concept for developing low loss fibers was possible from the proposal of Charles K. Kao and George Hockman in 1966 when they showed that losses in existing glass was due to contaminants and that these could potentially be removed [25]. It was not until the 1970's that the optical fiber was successfully invented by Corning Glass Works researchers Robert Maurer, Donald Keck, and Peter Schultz (patent no. 3,711,262) [26] with low enough attenuation and the development of the GaAs semiconductor laser that optical fiber technology became practical. Afterwards, development on lasers and fiber-optic communications started and continued to develop at a rapid pace.

The first fiber-optic communication systems operated around 0.8 μm with a bit rate of 45 Mbps with repeater spacing of up to 10 km. It was found in the 1970's that the repeater distances can be increased by shifting the wavelength to 1.3 μm. In the 1980's, the second generation of fiber-optic communication was developed and operated in the 1.3 μm window and used

InGaAsP semiconductor lasers. The bit rate of early systems was limited to below 100 Mbps because of dispersion in multimode fibers, but this limitation was overcome with the development of the single mode fiber. One of the issues during this time period was having practical connectors capable of working with the newly developed single mode fiber. Towards the end of the decade, commercial systems were able to operate at bit rates up to 1.7 Gbps and repeater spacing of 50 km [23],[24].

The third generation fiber systems operated at 1.55 μm and fibers at this time had losses of about 0.2 dB/km. Many of these improvements are due to the discovery of Indium gallium arsenide (InGaAs) and the InGaAs photodiode. It was during this time that the dispersion problems experienced in optical systems could be reduced by using dispersion shifted fibers that had minimum dispersion near 1.55 μm. The third generation systems were able to operate at speeds of 2.5 Gbps with repeater spacings in excess of 100 km [22]. The fourth generation systems used optical amplification to increase the distance between repeaters and began using wavelength division multiplexing (WDM) to increase data capacity. The development of the erbium doped fiber amplifier (EDFA) was a major breakthrough as these optical amplifiers could compensate for losses in the fiber system and reduce the number of repeaters required. This resulted in a revolution that resulted in the doubling of system capacity every six months. By 2006, a bit-rate of 14 Tbps was achieved over a 160 km line [23],[24].

The fifth generation of fiber optic communications is concerned with extending the wavelength range of the WDM in order to increase the wavelength range the system can operate. This has led to the wavelength windows known as C, L, and S bands. C is for the conventional band in the range from 1.53-1.57 μm, and the window was extended for long and short wavelengths on either side resulting in L and S bands, respectively. Also a new kind of fiber

known as dry fiber had been developed with very little loss that led to optical systems able to support thousands of WDM channels. Also the fifth generation systems tried to increase the bit rate within these WDM channels by using optical solitons as pulses. Optical solitons are pulses that preserve their pulse shape during propagation by counteracting the effect of dispersion through the fiber nonlinearity [22].

Today, much of the development is focused on creating a "smart" mesh grid network. With increased content delivery services, fiber optics are no longer just used for long haul networks and are being used for metropolitan networks. These networks need to be able to quickly adapt to any impairment and adapt to large volumes of traffic. The invention of the colorless, distortionless, contentionless reconfigurable optical add drop multiplexer (CDC-ROADM) will be revolutionary in making networks more agile and robust [27],[28]. In the past, sending data required a direct link from transmitter to receiver. With the CDC-ROADM, it can act as an optical switch and can send the data in any direction and on a new wavelength [27],[28]. The ability to instantly switch wavelengths and directions provides much greater flexibility for a network and allows it to send information quickly. There is also focus on making next generation networks more robust by using a control plane that can monitor and rapidly adapt to impairments. Repairs on modern optical communication systems are very time consuming and can bring an entire network down for hours or days. By being able to monitor a network continuously, a "smart" network can allocate resources to where traffic is heaviest and identify where problems may occur before it happens [29]. If a disaster occurs, then the network can immediately use these optical switches and redirect traffic to minimize network connectivity loss.

2.2 Analog Optical Links

Analog optical links, also referred to as Radio over Fiber (RoF), is a technology where light is modulated by a radio frequency signal and transmitted over an optical fiber link [1]. RoF is used for multiple purposes such as cable television, phased arrays, networks, and military radar applications. The most common usage is to facilitate wireless access because of its ability to transport signals over long distances and reach areas where wireless cannot penetrate.

Analog optical links are comprised of three main parts: a transmitter, transmission medium, and a receiver [30],[31]. The basic transmitter consists of a laser and a modulator where the laser acts as a carrier and the signal we want to send is modulated via a modulator onto the carrier signal. The optical fiber acts as the transmission medium. The signal from the transmitter is transported along the optical fiber. At the receiver, the transmitted signal is detected using detectors. This will allow us to demodulate and recover the signal. A schematic of an optical link is shown in Figure 2.1 [32].
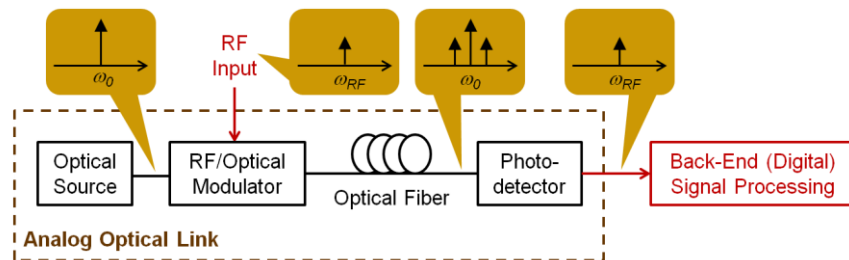
Figure 2.1. Schematic of a typical intensity-modulation direct-detection analog optical link [32].

There are several advantages of using an optical link to send radio signals [1]. An optical link has low loss and is able to send signals across a longer distance with less power compared to a copper coaxial cable. The cost to manufacture and maintain optical fibers is cheaper than

copper. In addition, photonic devices are capable of very high speeds and inherently have a large bandwidth. This makes them suitable for future generations and device upgrades for years to come as we have not yet reached those speeds. Also optical fiber is bit rate and protocol independent, hence it can be used in current and future technologies. The optical fiber is immune to electromagnetic interference, so other electrical signals and lightning strikes will not affect its performance. Furthermore, fibers can be deployed to "dead zones," secluded areas where wireless signals cannot access easily such as in large buildings, tunnels, and rural areas. By deploying RoF, we can reach these areas and set up wireless access points [3],[4].

2.3 Intermodulation Distortion

One of the problems when sending signals in an optical fiber for long distances is the generation of intermodulation distortions (IMD). IMD is the amplitude modulation of signals containing two or more different frequencies in a system with nonlinearities. It is an important metric of linearity for a wide range of RF devices and components. Good IMD performance is essential in many applications because interference from other signals can pollute the spectrum and create crosstalk [33].

IMD measurement begins with a two tone test where a two-tone signal is injected into a device under test [33]. For instance, a signal with two tones at frequencies ω_1 and ω_2 and with amplitudes V_1 and V_2 respectively described by equation 2.1 is input to a device under test.

$$V_{input} = V_1 \cos(\omega_1 t) + V_2 \cos(\omega_2 t) \tag{2.1}$$

Most RF components have a degree of nonlinearity and for weakly nonlinear systems, the output can be given by the Taylor series power expansion:

$$V_{out} = G_1 V_i + G_2 V_i^2 + G_3 V_i^3 + \cdots \qquad (2.2)$$

For systems with strong nonlinearities, the nonlinearities can be described by the Volterra Series. In a perfectly linear device, the output signal will only be represented by just the first term in equation 2.2 and produce two tones at the exact same frequencies as the input signal. A single tone signal will produce harmonic distortions which are additional frequency components that appear at integer multiples of the input frequency. A two tone signal will produce both harmonic distortion and intermodulation distortions [33],[34]. For this scenario frequency components appear not just at harmonic frequencies of the two original input frequencies, but also at the sum and difference of those frequencies and at integer multiples of those sum and difference frequencies. Figure 2.2 below illustrates these generated intermodulation products and their frequency locations [35].

$$
\begin{aligned}
P_{out} = \ & a_1 f_1 + a_2 f_2 + && \leftarrow \text{Fundamentals} \\
& a_3(f_1 \pm f_2) + && \leftarrow 2^{nd} \text{ Order Products} \\
& a_4(f_1 \pm 2f_2) + a_5(2f_1 \pm f_2) + && \leftarrow 3^{rd} \text{ Order Products} \\
& a_6(2f_1 \pm 2f_2) + && \leftarrow 4^{th} \text{ Order Products} \\
& \ldots + a_\infty(\infty f_1 \pm \infty f_2) && \leftarrow \text{ etc.}
\end{aligned}
$$
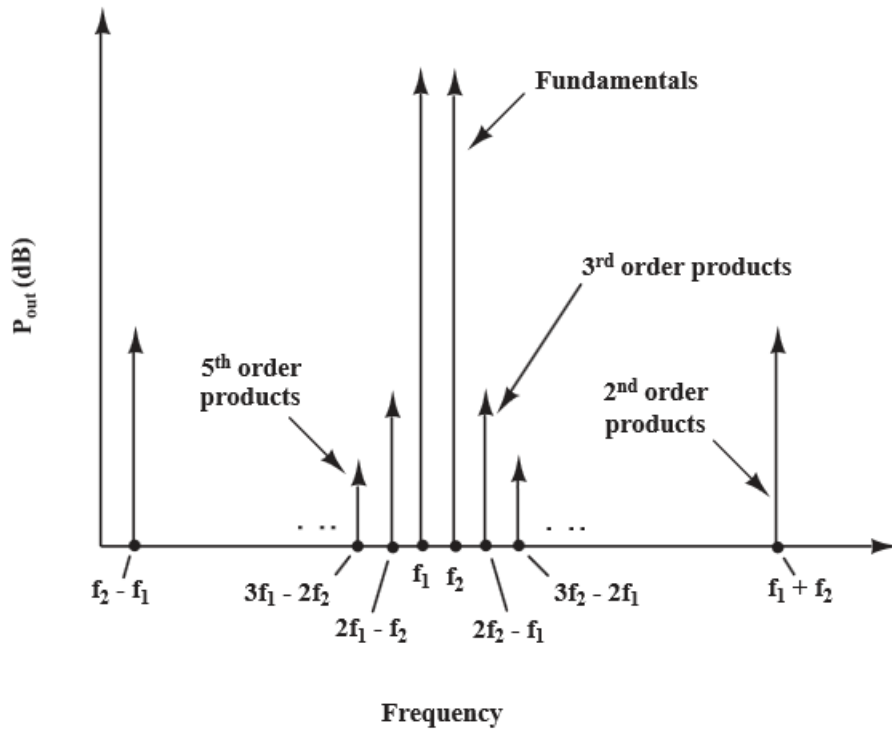
Figure 2.2. Spectrum of the intermodulation products generated by nonlinearities in a system [35].

Typically, the third order intermodulation products are of interest because they are closest to the fundamentals. Intermodulation products can be removed by filtering or are out of band and cause no problems. The intermodulation products that fall in-band add nonlinearity and distortion to the output. It is important to note that IMD is problematic in RF and microwave systems for a couple reasons. For modulated signals, third order distortion creates additional frequency content often called "spectral regrowth" in bands adjacent to the modulated signal. In a transmitter, spectral regrowth can interfere with other wireless channels [33]. In a receiver, it can cause out-of-band signals to obscure the signal of interest. In an optical link, the nonlinearity contribution is mostly due to the Mach-Zehnder modulator which has a nonlinear transfer function.

2.4　Spurious Free Dynamic Range

The spurious free dynamic range (SFDR) measures the strength ratio of the fundamental signal to the strongest spurious signal in the bandwidth at the output. It is the range of input powers allowed to be inputted into the system without generating any harmonics or intermodulation distortions. As mentioned in the previous section, the third order is usually the largest spur in the band. In an optical link with the modulator biased at quadrature, even order harmonics cancel out leaving only the odd ordered intermodulation distortions. To measure the spurious free dynamic range, a two tone test is performed [33]. During a two tone test, the fundamental signal powers and the third intermodulation products (or the largest spur) are plotted. As the signal power is increased, the intermodulation products increase at a rate n faster than the fundamental where n is the intermodulation order [34]. We can see this from equation 2.2 if we expand the series. The point where the fundamental power and third order product line intercept is called the third order intercept point. This is the theoretical point where the third order intermodulation products overtake the fundamentals, but this never happens in real systems due to output power saturation [35]. We can measure or extrapolate the fundamental signal power and third order product to the noise floor of the system as shown in Figure 2.3. The range of power from where the third order product crosses the noise floor to the fundamental signal power is called the spurious free dynamic range which is the maximum dynamic range achievable. Given the noise floor and third order intercept point, we can calculate the SFDR by using the equation

$$SFDR = \left(\frac{IP3_{in}}{kTB\ NF}\right)^{\frac{n-1}{n}}$$

(2.3)
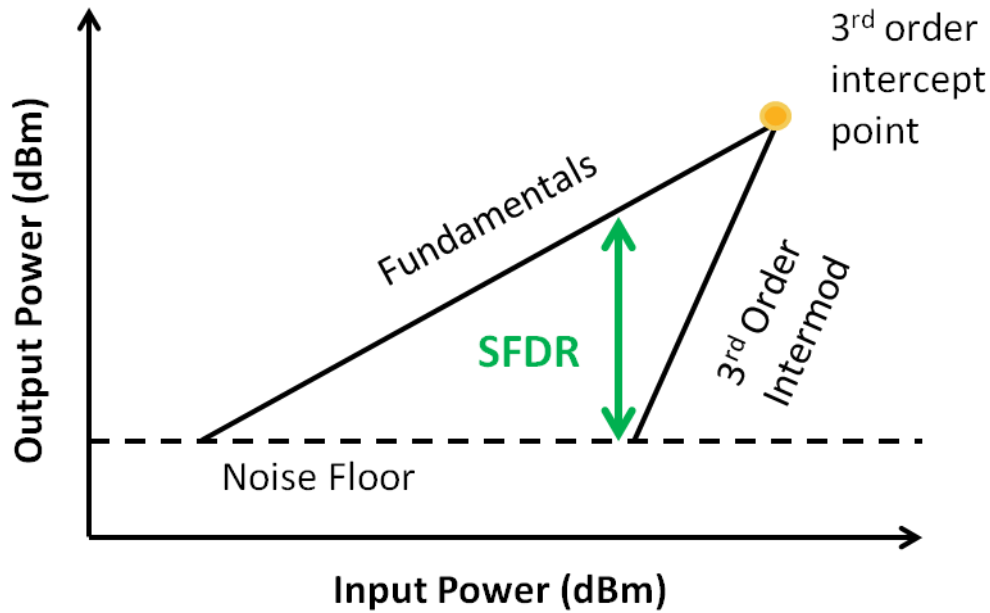
Figure 2.3. Measuring the spurious free dynamic range from a two tone test.

2.5 Fundamentals of Photonic Time-Stretch

In the second part of this thesis, time-stretch enhanced recorder (TiSER) is used for ultra-wideband frequency estimation and for high speed measurement applications. In this section, the fundamentals of photonic time-stretch are discussed. First, I will give a brief overview of the photonic time-stretch preprocessor from a systems perspective, discuss briefly how the time-stretch analog-to-digital converter can be implemented into continuous time, and then go through the mathematical framework of time-stretch. Lastly, I will discuss about the time-bandwidth product and how dispersion penalty can limit the bandwidth of the time-stretch system. However, dispersion penalty is not a fundamental limitation and can be mitigated using several techniques.

2.5.1 Photonic Time-Stretch Preprocessor

Time-stretch is able to provide the equivalent of an extended bandwidth of the electronic analog-to-digital conversion process. It does so by employing group velocity dispersion to slow down the analog signal in time (compressing its bandwidth) before digitization by an electronic ADC. Time-stretch preprocessor uses a dispersive analog optical link except a chirped pulse source is used instead of a continuous wave source [12]. The basic operating principle is shown in Figure 2.4.
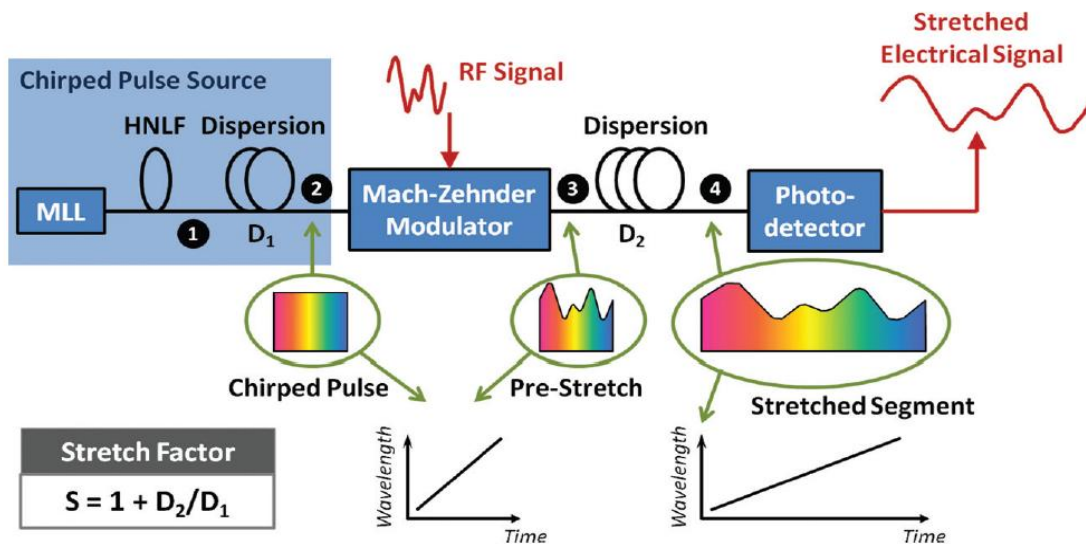
Figure 2.4. Basic operating principle of time-stretch [12].

A train of short optical supercontinuum pulses is generated by dispersing broadband pulses from a mode locked laser. To generate a supercontinuum pulse, a mode locked laser generates high peak power narrow linewidth pulses that go through a highly nonlinear fiber which broadens the pulse spectrum through nonlinear interactions such as self phase modulation, modulation instability, and Raman frequency conversion. The first dispersive fiber (with dispersion

17

parameter D_1 and length L_1) chirps the pulse using group velocity dispersion (GVD) which is the phenomenon that the velocity of light is dependent on the wavelength or frequency in a transparent medium. In an optical fiber, frequencies travel at different velocities which will spread the pulse. This creates a chirped optical pulse and results in a way to perform wavelength to time mapping. At the Mach-Zehnder electro-optic modulator, the analog input signal is intensity modulated onto these chirped pulses. This maps a particular wavelength to the modulated RF signal. The pre-stretched segment is then propagated through a second dispersive fiber (with dispersion parameter D_2 and length L_2) which stretches out the segment even more. Finally the segment is converted to the electrical domain using a photodetector. The stretch factor for the system describes the factor the signal has been stretched or how much the signal bandwidth has been compressed. The time stretch factor is given by,

$$S = \frac{Temporal\ pulse\ width\ (after\ time - stretching)}{Temporal\ pulse\ width\ (after\ pre - chirping)}$$

$$S = \frac{D_1 + D_2}{D_1} = 1 + \frac{D_2}{D_1} \tag{2.4}$$

If the dispersion parameters are the same, we can represent the stretch factor as a function of their lengths,

$$S = 1 + \frac{L_2}{L_1} \tag{2.5}$$

2.5.2 Continuous Time-Stretch Analog-to-Digital Converter

This system can be extended for continuous operation by using a train of supercontinuum pulses to stretch the signal and dividing the signal into multiple segments [11],[12]. The continuous time-stretch system with stretch factor of four is depicted in Figure 2.5 [12]. The input RF signal

18

is split into multiple segments and divided by a wavelength division multiplexer and each segment is stretched in time and digitized. The resulting four segments can then be digitally recombined by stitching the segments back together. The capture time would be the length of all the segments added together. However for longer stretch factors, we would need the same number of ADCs as the stretch factor. A continuous time-stretch version of this was demonstrated by Aerospace Corporation and discussed in [36], [37]. Unlike a traditional time-interleaved ADC array, the analog signal that each ADC sees is below its Nyquist bandwidth. Since the signal at the input of each digitizer is slowed to below Nyquist bandwidth, each digitizer is able to capture the full input signal. This is different than a conventional sample-interleaved ADC in which the signal at the digitizer is above its Nyquist rate [12].
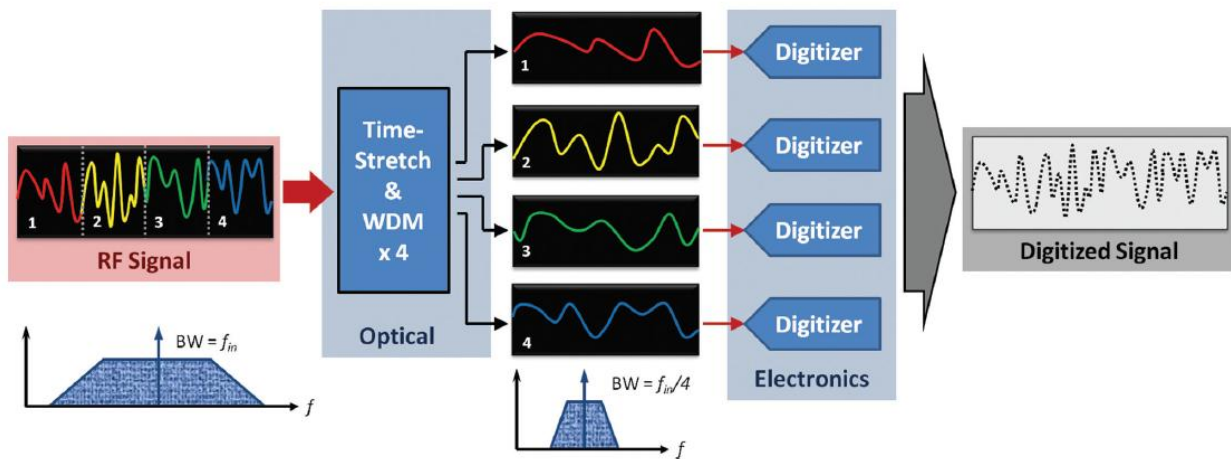
Figure 2.5. Continuous time-stretch ADC diagram for stretch factor of four [12].

2.5.3 Mathematical Framework for Time-Stretch

In this section, mathematical framework for time-stretch is provided [11], [12]. Since time-stretch uses a modified optical link, understanding the nature of the carrier wave and modulation

19

sidebands and what happens to them as they propagate through the system is required. The symbols used are defined in Table 2-1.

Table 2-1. Symbols used in time-stretch ADC mathematical framework [12].

Parameter	Definition	Dimensions
$E, \tilde{E}$	Electric fields in time and frequency domains, respectively	V/m
m	Modulation index ($\pi V_{amp}/V_\pi$)	-
ω_{RF}	Angular frequency of the original electrical signal	rad/s
β_2, β_3	Second and third order dispersion parameters, respectively	s^2/m, s^3/m
η	Photo-detector responsivity	A/W
α	Attenuation coefficient	1/m
γ	Nonlinear coefficient	W-1/km-1
n	Refractive index of the fiber	-
ε_0	Relative permittivity of free space	F/m
A_{eff}	Effective optical field mode area in fiber	m2
P_{in}	Average optical power at photo-detector input	W
V_{amp}	Signal amplitude	V
V_π	Half wave voltage of the Mach Zehnder modulator	V

In this framework, the time domain electric fields at different positions in the time-stretch system are denoted by E and the Fourier transforms of these fields are denoted by $\tilde{E}$ to represent them in the frequency domain.

We assume the optical supercontinuum pulse is transform-limited and has a Gaussian envelope. In the frequency domain, its electric field can be represented as

$$\tilde{E}_1(\omega) = \int_{-\infty}^{+\infty} E_1(t)e^{-j\omega t} dt \tag{2.6}$$

$$\tilde{E}_1(\omega) = E_0(2\pi T_0^2)^{\frac{1}{2}} \exp\left(-\frac{\omega^2 T_0^2}{2}\right) \tag{2.7}$$

where T_0 is the pulse half-width and E_0 is the pulse amplitude. $\tilde{E}_1$ represents the electric field at the output of the source. After propagating through the first dispersive fiber, the electric field can be represented as $\tilde{E}_2$.

20

$$\tilde{E}_2(\omega) = \tilde{E}_1(\omega)exp\left(\frac{j\beta_2\omega^2 L_1}{2} + \frac{j\beta_3\omega^3 L_1}{6}\right) \tag{2.8}$$

Here both the linear group velocity dispersion term β_2 and its dispersion slope β_3 are included. To simplify the mathematics in this section, the β_3 term is ignored. Non-quadratic phase shifts caused by β_3 of GVD elements and elsewhere in the signal path cause time warping in the stretched signal. $\tilde{E}_2$ represents the signal before the modulator. Assuming a push-pull Mach-Zehnder modulator biased at quadrature point and after modulation by a sinusoidal RF signal of angular frequency ω_{RF}, the field can be represented as

$$E_3(t) = E_2(t)cos\left(\frac{\pi}{4} + \frac{m}{2}\,cos\omega_{RF}t\right) \tag{2.9a}$$

where m is the modulation index. Equivalently, the field after the MZM can be represented as $E_3(t)$.

$$E_3(t) = \frac{E_2(t)}{2}\left[e^{j\left(\frac{m}{2}\right)cos(\omega_{RF}t)} + e^{-j\left(\frac{m}{2}\right)cos(\omega_{RF}t)+j\pi/2}\right] \tag{2.9b}$$

Next we can do a Taylor series expansion of the term $(m/2)\,cos(\omega_{RF}t)$ where the second and higher order terms are ignored if we assume a linear approximation. This linear approximation leads to a double sideband-modulated chirped carrier,

$$\begin{aligned}
E_3(t) &\approx \frac{E_2(t)}{\sqrt{2}}e^{\frac{j\pi}{4}}\left[1 + \frac{m}{2}cos(\omega_{RF}t)\right] \\
&= \frac{E_2(t)}{\sqrt{2}}e^{j\pi/4}\left[1 + \frac{m}{4}\left(e^{j\omega_{RF}t} + e^{-j\omega_{RF}t}\right)\right]
\end{aligned} \tag{2.10}$$

with frequency-domain representation of this field given by

$$\tilde{E}_3(\omega) = \frac{e^{j\pi/4}}{\sqrt{2}}\left[\tilde{E}_2(\omega) + \frac{m}{4}\left(\tilde{E}_2(\omega - \omega_{RF}) + \tilde{E}_2(\omega + \omega_{RF})\right)\right]. \tag{2.11}$$

This field then propagates through the second GVD element and the resulting electric field is,

$$\tilde{E}_4(\omega) = \tilde{E}_3(\omega)exp\left(\frac{j}{2}\beta_2\omega^2 L_2 + \frac{j}{6}\beta_3\omega^3 L_2\right). \tag{2.12}$$

21

Once again, we ignore the β_3 term for simplicity which gives the field at the photo-detector.

$$\tilde{E}_4(\omega) = \tilde{E}_3(\omega)e^{-\frac{j\omega^2\beta_2 L_2}{2}} \tag{2.13a}$$

$$\begin{aligned}
\tilde{E}_4(\omega) = \frac{e^{j\pi/4}}{\sqrt{2}} e^{-j\omega^2\beta_2 L_2/2} \\
\times \left(\tilde{E}_1(\omega)e^{-j\omega^2\beta_2 L_1/2} + \frac{m}{4}\tilde{E}_1(\omega - \omega_{RF})e^{-\frac{j(\omega-\omega_{RF})^2\beta_2 L_1}{2}} \right. \\
\left. + \frac{m}{4}\tilde{E}_1(\omega + \omega_{RF})e^{-\frac{j(\omega+\omega_{RF})^2\beta_2 L_1}{2}} \right).
\end{aligned} \tag{2.13b}$$

For wideband supercontinuum pulses (ie. $\Delta\omega_{optical} \gg \Delta\omega_{RF}$) that have slow frequency dependent variations, we can approximate $\tilde{E}_1(\omega \pm \omega_{RF}) \approx \tilde{E}_1(\omega) \approx \tilde{E}_1\left(\omega \pm \frac{\omega_{RF}}{S}\right)$. We also define the dispersion-induced phase as $\phi_{DIP} = \omega_{RF}^2\beta_2 L_2/2S$ where $S = 1 + D_2/D_1$ and the envelope function is defined as

$$\tilde{E}_{env}(\omega) = \frac{e^{j\pi/4}}{\sqrt{2}}\tilde{E}_1(\omega)e^{j\omega^2\beta_2(L_1+L_2)/2}. \tag{2.14}$$

We can then rewrite 2.14 as

$$\tilde{E}_4(\omega) = \tilde{E}_{env}(\omega) + \frac{m}{4}e^{-j\phi_{DIP}} \times \left[\tilde{E}_{env}\left(\omega - \frac{\omega_{RF}}{S}\right) + \tilde{E}_{env}\left(\omega + \frac{\omega_{RF}}{S}\right)\right] \tag{2.15}$$

which gives time-domain representation as

$$E_4(t) = E_{env}(t)\left[1 + \frac{m}{4}e^{-j\phi_{DIP}} \times \left(e^{\frac{j\omega_{RF}t}{S}} + e^{-\frac{j\omega_{RF}t}{S}}\right)\right]. \tag{2.16}$$

The photocurrent at the photo-detector without a modulated signal is given by,

$$I_{env}(t) = \frac{c\epsilon_0 n}{2}\eta A_{eff}E_{env}(t)E_{env}^*(t). \tag{2.17}$$

Therefore, the output current with RF modulation is

$$I_{out}(t) = \frac{c\epsilon_0 n}{2}\eta A_{eff}E_4(t)E_4^*(t)$$

$$I_{out}(t) = I_{env}(t) \times \left[1 + mcos\left(\frac{\omega_{RF}t}{S}\right)cos(\phi_{DIP}) + \frac{m^2}{4}cos^2\left(\frac{\omega_{RF}t}{S}\right)\right]. \qquad (2.18)$$

For small values of m (i.e. m << 1), the m^2 component can be ignored, and envelop modulation can be removed to give the current with just the signal.

$$I_{signal}(t) = \frac{I_{out}(t) - I_{env}(t)}{I_{env}(t)} = m \cos\left(\frac{\omega_{RF}t}{S}\right)cos(\phi_{DIP}) \qquad (2.19)$$

From the output current, this output signal has a frequency of ω_{RF}/S for the input signal frequency ω_{RF}, which implies that the frequency (and the bandwidth) are compressed or that the signal is stretched in time by a factor of S.

2.5.4 Time-Bandwidth Product

The photonic time-stretch system could be described by the following three parameters: the stretch factor, time aperture, and RF bandwidth [11]. The stretch factor as mentioned previously is the factor in which the RF signal is stretched in time or the factor its bandwidth is compressed. The time aperture is defined as the pulse width after the first dispersive fiber, equivalent to the amount of time that each pulse captures data: $T_A = \Delta\lambda D_1 L_1 = \beta_2 L_1 \Delta\omega_{opt}$ where $\Delta\omega_{opt}$ is the optical bandwidth. Ideally, it is desirable to maximize the time aperture, however there are tradeoffs. To increase the time aperture while maintaining a constant stretch factor, one would simply increase L$_1$. However a larger L$_1$ would increase the dispersion penalty and reduce the overall RF bandwidth. Thus one cannot only use the time aperture or just the bandwidth to assess the performance. The time-bandwidth product is identified as a metric to evaluate the overall performance and is defined as $TBP = 2T_A \Delta\omega_{RF}$. For a dual sideband modulated system, the TBP is given as

23

$$TBP_{DSB} = 2T_A\Delta f_{RF} = \frac{\Delta f_{opt}}{2\Delta f_{RF}}. \tag{2.20}$$

2.5.5 Dispersion Penalty

The frequency dependent phase term $\cos(\phi_{DIP})$ results in nulls in the frequency response. The modulator produces upper and lower sidebands of the RF signal in the optical spectrum at frequencies of $\omega_{optical} \pm \omega_{RF}$. In the absence of dispersion, these sidebands beat with the optical carrier at the photo-detector to reproduce a copy of the signal. Since dispersion is present, the upper and lower sidebands slip in phase with each other and interfere at the photo-receiver, creating nulls at certain frequencies when the two sidebands are 180 degrees out of phase. This produces a periodic fading characteristic versus frequency shown by Figure 2.6 [12]. For a double sideband modulated signal with dispersion parameter β_2, second dispersive fiber length L_2, and angular frequency ω_{RF}, the transfer function is given by

$$H(\omega_{RF}) = \cos\left(\frac{\beta_2 L_2 \omega_{RF}^2}{2S}\right). \tag{2.21}$$

This equation is similar to an optical link if it were dispersed by fiber of length L_2/S. The fiber is not shorter, but the frequency of the signal has been decreased due to the stretching. This causes the total dispersion induced phase to be reduced. However, dispersion penalty can limit the total bandwidth of the time-stretched signal and acts as a low pass filter. The 3 dB RF bandwidth in equal to $\Delta f_{RF} = \sqrt{\frac{1}{8\pi|\beta_2|L_1}}$ which is valid for M $\gg$ 1.
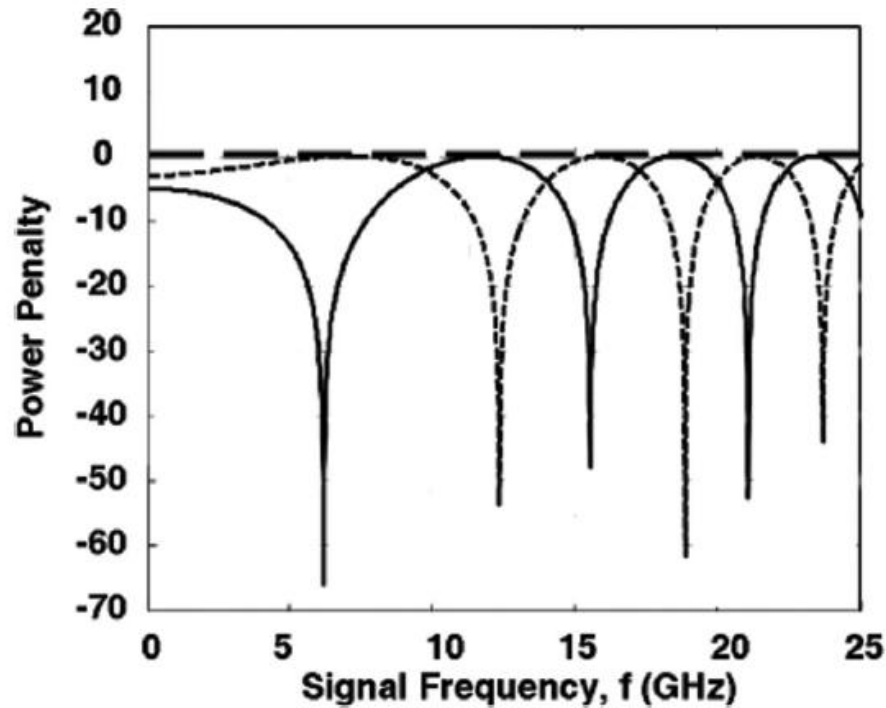
Figure 2.6. Dispersion penalty curves in a conventional optical link and for a photonic time-stretch ADC (solid line). By mitigating the dispersion penalty, we get a flat response (wide dotted lines) [12].

The solid line represents the dispersion penalty behavior in a conventional optical link and in the photonic time-stretch ADC. In practice, the dispersion penalty can be eliminated by employing either single sideband modulation [38] or by taking advantage of the natural phase diversity in the outputs of a dual-output Mach Zehnder modulator [39]. Since dispersive fading phenomenon occurs due to the interference from the two sidebands, single sideband modulation can avoid this effect. For this technique, a dual-drive MZM that has two phase modulating arms that can be independently driven by RF sources is used. When the modulator is biased at quadrature point, one of the RF sidebands in the optical field from the two arms will add destructively at the output

25

coupler, whereas the other sideband will add constructively. This suppresses one of the sidebands and eliminates the frequency dependent fading. The bandwidth of the hybrid coupler sets the limit on the maximum system bandwidth that can be achieved using the system.

The second technique is known as phase diversity. This technique uses maximum ratio combining of two outputs from a MZM, which have inherently complementary transfer functions. As seen in Figure 2.6, one output would be the solid line and the other is the dotted line which shows complementary fading characteristics. When one is at a maximum, the other is at a null. By combining the maximums, this ensures that both channels will never have a common frequency null and thus removes the bandwidth limitation to the system. This technique is used to demonstrate an ultra-wideband TS-ADC with an ideal impulse response.

2.6 Discrete Fourier Transform

In mathematics, the Fourier Series is used to represent complicated periodic signals as a summation of sines and cosines. The Fourier transform is an extension of the series where the period of the signal is lengthened and allowed to approach infinity. The Fourier transform and its inverse is given by the following two equations respectively [40].

$$\tilde{F}(\omega) = \int_{-\infty}^{+\infty} f(x)e^{-i\omega t}dx \tag{2.22}$$

$$f(x) = \frac{1}{2\pi} \int_{-\infty}^{+\infty} \tilde{F}(\omega)e^{i\omega t}d\omega \tag{2.23}$$

Since we have a finite number of samples that we use to compute the Fourier Transform, the discrete Fourier transform (DFT) is used. The DFT transforms N samples of a discrete-time signal to the same number of discrete frequency samples and is defined as [41]

26

$$X(k) = \sum_{n=0}^{N-1} x(n)e^{-\frac{i2\pi nk}{N}} \tag{2.24}$$

The DFT is invertible by the inverse discrete Fourier transform given by

$$x(n) = \frac{1}{N} \sum_{k=0}^{N-1} X(k)e^{\frac{i2\pi nk}{N}} \tag{2.25}$$

The theoretical frequency resolution limit, the smallest resolvable frequency resolution, is given by

$$\delta f = \frac{1}{T} = \frac{f_s}{N} \tag{2.26}$$

where f_s is the sampling frequency, T is collection time, and N is number of samples [41]. With a longer collection time, the frequency resolution limit becomes finer. To increase the frequency resolution, we could either decrease the sampling frequency, f_s, or increase the number of samples N. Decreasing f_s is usually not practical because that would decrease the range of frequencies that can be measured. Typically the number of samples N is increased by taking a longer measurement. Many times, zero-padding is used to extend the number of points or to make the number of points a power of 2 making it easier for the computer to compute the DFT. However, despite zero-padding increases the frequency resolution by extending the number of points for the DFT, it does not add any additional information. It only interpolates the frequency spectrum [41]. The smallest resolvable frequency resolution is still determined by the inverse of the collection time. When resolving two frequencies placed close together, these frequencies need to be spaced apart greater than the minimum frequency resolution. For the time-stretch system, this collection time is the length of the chirped pulse after the first dispersive element which we defined as the time aperture.

For amplitude measurements, the accuracy of the amplitudes is limited by the resolution of the frequency bins. The energy of the frequency components when computed by the DFT will fit into frequency bins. For one frequency the energy might fit into a bin while for another frequency the energy could be detected by multiple bins and could spread into adjacent bins. This frequency spreading is known as spectral leakage. Spectral leakage occurs mainly due to arbitrary sampling of signals. Instead of having pre-determined starting and ending times to capture an integer number of cycles, arbitrary starting and ending times capture a non-integer number of cycles with abrupt starting and ending edges. This causes the peak in the frequency-domain to broaden and spread into adjacent frequency bins. This might give the false error after performing a DFT for two signals that appear to not be equal in amplitude despite they are due to the spreading of the energy. This peak magnitude error due to insufficient frequency sampling is known as scalloping loss [41].

Windowing the signal can help to reduce spectral leakage and also affect the ability to resolve two signals close together. By windowing [42], a weighting function can be applied across the captured signal so that the edges are close to zero and the center of the signal where the cycles are complete and amplitude is maximized is close to "1." Depending on the window used, the peak could broaden due to the frequency response. For resolving two tones close together, a rectangular window is best since the peak is sharpest, however it has the most scalloping. When using other windows, the spreading of the peak energy could cover two tones close together. In general, the type of window used should be application specific.

Chapter 3

Digital Broadband Linearization of Optical Links

This chapter is an expanded version of two published manuscripts [32],[42] where we present a digital post-processing linearization technique to efficiently suppress dynamic distortions added to a wideband signal in an analog optical link. This technique achieves up to 35-dB suppression of intermodulation distortions over multi-octaves of signal bandwidth. In contrast to conventional linearization methods, it does not require excessive analog bandwidth for performing digital correction. This is made possible by re-generating undesired distortions from the captured output, and subtracting it from the distorted digitized signal. Moreover, we experimentally demonstrate record spurious-free dynamic range of 120 dB.Hz$^{2/3}$ over 6-GHz electrical signal bandwidth. While our digital broadband linearization technique advances state-of-the-art optical links, it can also be applied to other nonlinear dynamic systems.

3.1 Introduction

Analog optical links have become extremely useful platforms over the past decades for transmitting and/or routing analog radio frequency (RF) signals over long distances. Due to wide-bandwidth and low-loss characteristics of optical fibers, analog optical links [44] have attracted a broad range of applications, from RF antenna remoting and beam forming for phased-array radars [45], [46] to cable television (CATV) [45]-[48]. In such applications, the optical link must meet stringent performance requirements in terms of dynamic range, gain, bandwidth, and noise figure [49]-[52]. In general, intensity-modulation direct-detection (IMDD) analog optical link consists of an optical source followed by RF or optical modulation scheme as illustrated in Figure 3.1.
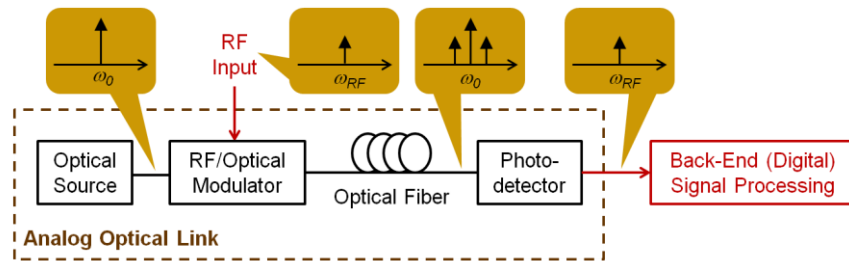
Figure 3.1. Schematic of a typical intensity-modulation direct-detection analog optical link [43].

They are hence categorized as either direct modulation or external modulation scheme. In either case, a trade-off between linearity and gain places upper limits on the dynamic range [46],[48]. For instance, if a Mach-Zehnder modulator (MZM) is used to externally-modulate the optical carrier, it inherently exhibits nonlinear behavior, leading to harmonic and intermodulation distortions of the analog RF signal. In addition, at the photo-detector, another trade-off between bandwidth and linearity defines the maximum system bandwidth. Over the past several years, significant efforts have been made for increasing the system bandwidth by improving the optical

components, while maintaining linearity and dynamic range. A sub-octave analog optical link has been developed through pioneer work by Betts, *et al* [52]. This technique that is capable of achieving a spurious-free dynamic range (SFDR) of 132 dB over 1-Hz bandwidth relies on a linearized modulator, consisting of two standard Mach-Zehnder modulators in series. Later, a broadband linearized modulator for frequencies up to 2.5 GHz was demonstrated by Ackerman [53], achieving a dynamic range of 122 dB.Hz$^{4/5}$ over 1-Hz bandwidth. Another technique that achieves a highly linear link was recently demonstrated by Chou, *et al* [54]. Their approach is based on coherent detection with feedback and is capable of achieving an SFDR of up to 124.3 dB.Hz$^{2/3}$ over 160 kHz of bandwidth. Finally, several techniques based on adaptive pre-distortion and post-distortion linearizers have been previously developed in our early work [55]-[57]. In case of pre-distortion linearizer [55], [56], adaptive complementary-metal-oxide-semiconductor (CMOS) circuits are designed to predict the distortions added by the optical link and to generate distortions that are equal but opposite in phase from the undesired components. Another approach is to perform post-distortion correction optically [57], which uses a spatial light modulator (SLM) and a feedback loop to optically generate the out-of-phase distortions, and hence it suppresses the optical nonlinearities. Unfortunately, while these approaches are effective for distortion suppression up to 20 dB, their operation bandwidth is limited to the bandwidth of the linearizer circuits. Another effort made by Karim and Devenport [58] was able to reduce the noise figure, and hence it was able to achieve an SFDR of 121 dB over 1 Hz, yet it requires 500 mW optical power at the photo-receiver. In work done by Juodawlkis, *et al*. [59], they were able to reduce distortions by reversing the MZM transfer function and improving the linearity of the modulator, yet they were unable to compensate for long fiber lengths and memory effects.

31

Clearly, all aforementioned methods are not able to obtain high dynamic range (>120 dB) and large (multi-octave) operation bandwidth at a moderate photocurrent simultaneously.

Here we propose and demonstrate an efficient digital post-processing linearization technique that is performed after photo-detection to suppress the intermodulation distortions by more than 31 dB over multi-octave bandwidth of analog signal. Our technique essentially estimates the input signal to the well-known nonlinear system (e.g., analog optical link) from the observed output. It can be also implemented on digital signal processing (DSP) units and/or field programmable gate arrays (FPGA) to perform real-time correction of the analog RF signal transmitted through an analog optical link. Moreover, it is compatible with the state-of-the-art sub-octave optical link and can be exploited at the back end to further improve their performance. We also report a record SFDR of more than 120 dB.Hz$^{2/3}$ across 6-GHz bandwidth (with only 1 mA of photocurrent) that has been achieved using the proposed digital linearization technique. A simplified implementation of digital broadband linearization was previously demonstrated by us [60]. It was shown that this technique is able to suppress the distortions by more than 15 dB in a photonic time-stretch analog-to-digital converter.

3.2   Digital Broadband Linearization Technique

All analog systems exhibit some nonlinear behavior which limits their dynamic range. The magnitude of the output does not follow the input which results in distortion of the signal. This nonlinear behavior can be memory-less or dynamic. Memory-less nonlinearity is frequency-independent, resulting in a direct mapping between instantaneous magnitudes of the input signal to their outputs. For dynamic or memory behavior, nonlinearities depend on the input signal over a period of time instead of a single time instance. In an optical link, the spurious free dynamic

range is limited by the intermodulation distortion products due to the nonlinear transfer function of the system.

The digital broadband linearization technique was first proposed and demonstrated for the time-stretch analog to digital converter (TSADC) [60]. The technique estimates the input to a well-known nonlinear system from the observed output. Moreover, it works in the presence of memory effects—something that many other linearization models cannot do. In [60], the linearization of TSADC was performed and the technique was compared to the arcsine method which is typically used to correct for memory-less systems. Using the post-compensation technique, it was shown the dynamic range of the TSADC improved by more than 15 dB compared to the arcsine operation [60].

The digital broadband linearization technique is an effective, yet simple way of suppressing distortions. The technique shown in Figure 3.2 is the single stage post-processing that can be applied to multi-octave and sub-octave analog optical link to significantly improve the performance. In this technique, the distorted RF signal is converted to the digital domain via a digitizer for post-compensation. The digitized signal is linearly equalized and scaled using a linear equalization filter so that the obtained signal [denoted by point (0)] represents the original signal X with the same amplitude plus the distortion component X'. Then, the signal $X+X'$ is sent through a digital signal processing block (1st stage) that emulates the transfer function of the analog optical link. Again, linear equalization and scaling is performed on the obtained signal from the nonlinear system emulator. As a result, the obtained signal is equal to $X+2X'+X''$ as shown in Figure 3.2 [denoted by point (1)]. Since the relative distortion added by a nonlinear system depends on the amplitude of the original signal, the linear equalization and scaling in the

first step is necessary to provide the same signal amplitude (albeit with a small additive distortion).

From
Photo-Detector

Distortion-
Free Signal

0 $X + X'$

1 $X + 2X' + X''$
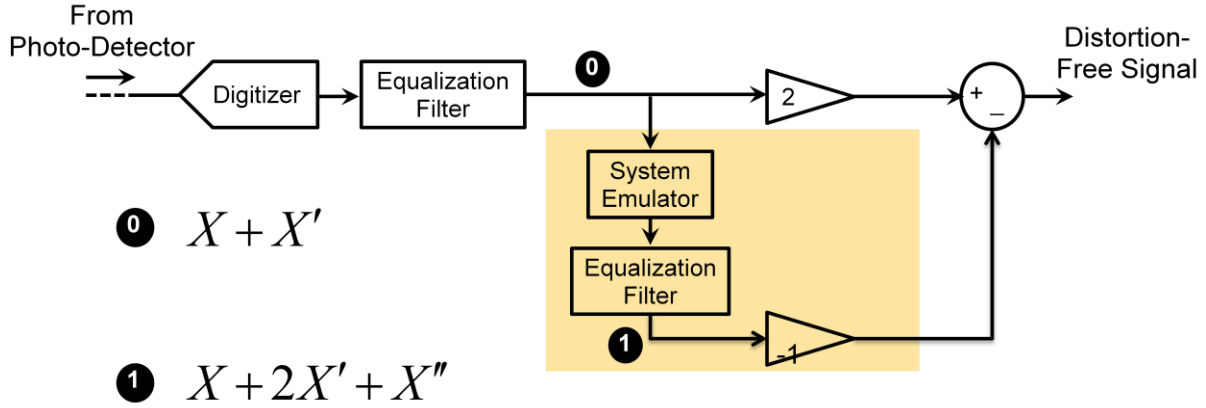
Figure 3.2. Digital broadband linearization technique is a single stage post-processing algorithm used to linear optical links [60].

3.2.1 Optical Link Emulator

For the digital broadband linearization technique to be effective, the transfer function of the system must be well modeled and understood. A typical optical link is comprised of a continuous wave (CW) source, a modulator, fiber, and a photodetector (PD). For our model used in the algorithm, we used an ideal laser with center wavelength of 1550 nm, push-pull Mach-Zehnder intensity modulator, standard single mode fiber (SMF), and an ideal PD. The carrier signal is generated by the CW source with electric field E_1. The RF signal is given by $x(t)$ and is intensity modulated using the MZM onto the carrier. The transfer function of the MZM is known and is given by

$$E_2(t) = \frac{1}{\sqrt{2}} E_1(t) \left[e^{jmx(t) + \frac{j\pi}{4}} + e^{jmx(t) - \frac{j\pi}{4}} \right] \tag{3.1}$$

34

and the optical fiber transfer function is given by

$$E(\omega) = E_2(\omega)e^{j\beta_2 L\omega^2}. \tag{3.2}$$

The output signal is detected by an ideal photodiode at the end giving output $y(t)$. Below in

Figure 3.3 is the optical link emulator used in the algorithm with the parameters used.
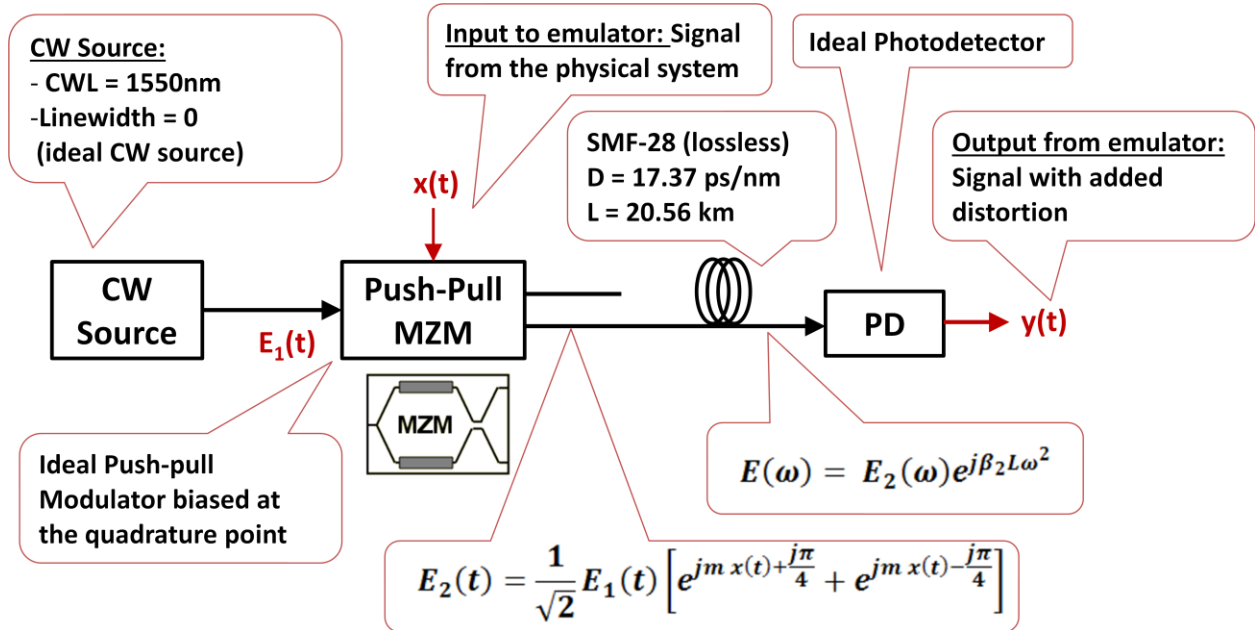
Figure 3.3. Optical link transfer function emulator used in the digital broadband linearization

algorithm.

3.3 Digital Broadband Linearization Algorithm

Following the success demonstrated by Fard, *et al.* [60] on applying the digital broadband

linearization technique to TSADC, we decided to apply this technique to a generic optical link.

The digital broadband linearization technique works well if the nonlinearity is weak. However, if

the nonlinearity is stronger, we cannot achieve perfect cancellation. To improve upon the result,

35

an iterative process was developed which we call the digital broadband linearization algorithm shown in Figure 3.4.

0 $X + X'$

1 $X + 2X' + X''$

2 $X + 3X' + 3X'' + X'''$

3 $X + 4X' + 6X'' + 4X''' + X^{(4)}$

i ...

n $X + (n+1)X' + ... + (n+1)X^{(n)} + X^{(n+1)}$
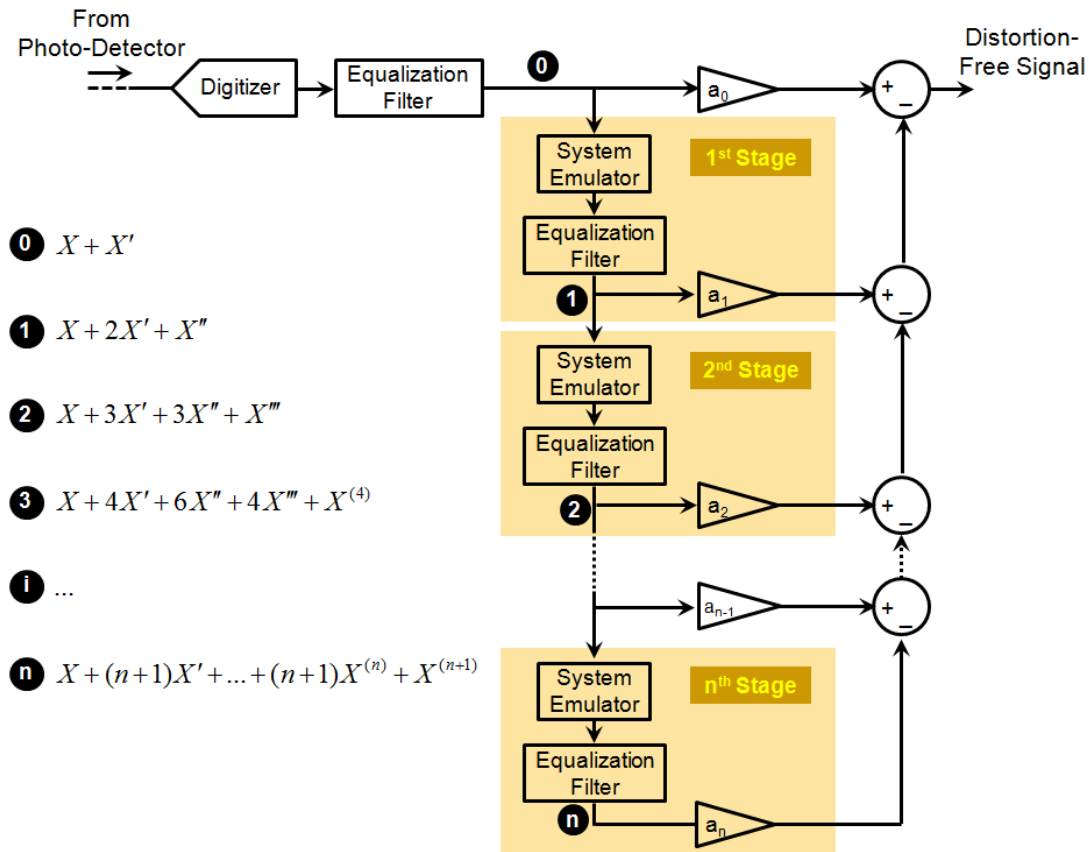
Figure 3.4. The digital broadband linearization algorithm is able to suppress nonlinearities in several stages [32].

This multi-stage digital broadband linearization algorithm follows the same process as outlined in the section above. The difference now is that the resultant signal is sent to subsequent stages similar to this first stage. A copy of the resultant signal of each stage is sent to the next stage, while another copy is multiplied by a gain factor and directed to the output. The gain factor follows the constants created in Pascal's triangle and provides the right gain to suppress higher order distortion terms. This procedure continues to the n-th stage. Note that we assume the

36

nonlinear distortion caused by the distortion from the last stage is negligible. The number of stages required here depends on the strength of nonlinear distortion, and hence it should be optimized to achieve maximum dynamic range and/or SFDR.
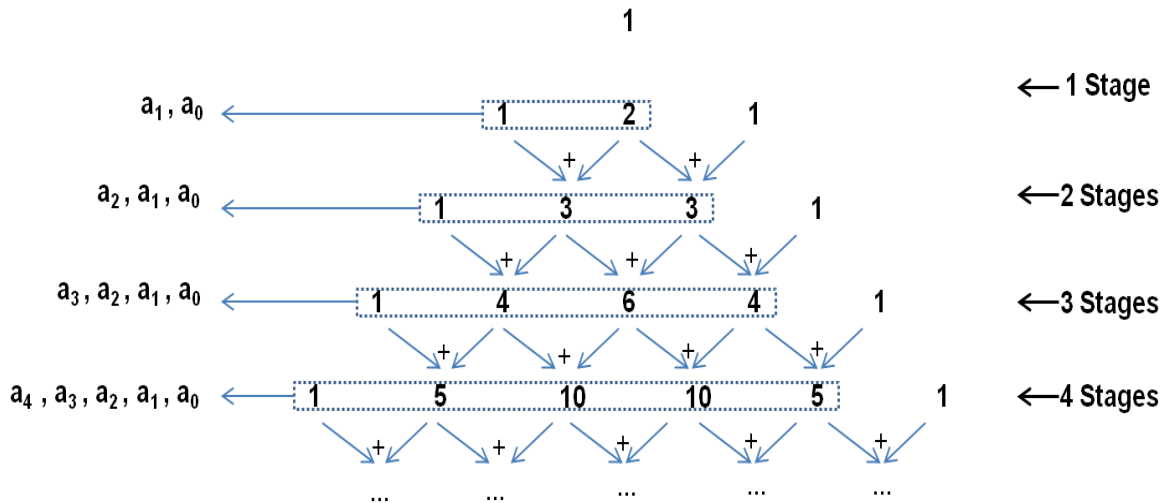
Figure 3.5. The gain coefficients used in the digital broadband linearization algorithm follows the coefficients from Pascal's triangle.

We also note that if the nonlinear distortions are strong, a mixing term (product of fundamental tone and distortion components) may become problematic. However, this can be mitigated by first applying a single-stage (n = 1) algorithm to reduce the intermodulation distortions to some extent, and then perform the multi-stage (n > 1) algorithm to fully suppress distortions. Note that if the system emulator does not match with the physical system, residue from imperfectly cancelled distortions would remain. These imperfections may become significant when utilizing a multi-stage block.

3.4 Experimental Results

To evaluate the performance of our algorithm, we built a link consisting of a continuous-wave laser, a standard $LiNbO_3$ Mach-Zehnder modulator (MZM), and ~20-km single-mode fiber. The long SMF-28 emulates a practical application, where the radio frequency signal is captured in a remote site. This is particularly important because in presence of dispersion, the nonlinear distortions become dynamic (i.e., with memory effect), which results in significant frequency-dependent nonlinear distortions. Finally, the modulated optical signal is detected by a PIN photodiode with a responsivity of 0.85 A/W. The photo-current was found to be 1 mA. Hence, our system exhibits ~ -22 dB of gain from input to output (without pre- and/or post-amplification). The resultant signal is digitized using a commercial digitizer with sampling rate of 50 GSamples/s and analog bandwidth of 16 GHz. The optical power was set so that the photocurrent is at 1mA. We then performed a two-tone test by coupling two input RF tones, f_1 and f_2, into the RF input port of the MZM. To minimize the 2nd-order distortion, the modulator is biased at quadrature. In order to measure the SDFR, we performed the two-tone measurement with different analog signal power levels for different frequencies up to 6 GHz. By cascading two single-stage blocks before the 4-stage block, we are able to suppress the third-order intermodulation distortions to some extent, and to avoid any additional distortions while propagating through the 4-stage block. Additionally, we checked the dispersion power penalty to ensure the 3rd-order distortion was not in a null when making the measurements.

Figure 3.7a and Figure 3.7b show output power versus input power for the fundamental input frequencies at 1 and 1.1 GHz and also at 6 and 6.1 GHz, respectively. As evident from these two plots, our digital broadband linearization technique achieves an SFDR of 120 dB.Hz$^{2/3}$ over 6-GHz bandwidth at 1mA of photocurrent. In addition, the fiber length of 20 km used in the

experiment showcases our ability to suppress the dynamic (i.e., frequency-dependent) distortions even in presence of large dispersion. Conventional optical links with longer fiber lengths are unable to obtain high SFDR values over such a large bandwidth [61]-[63].
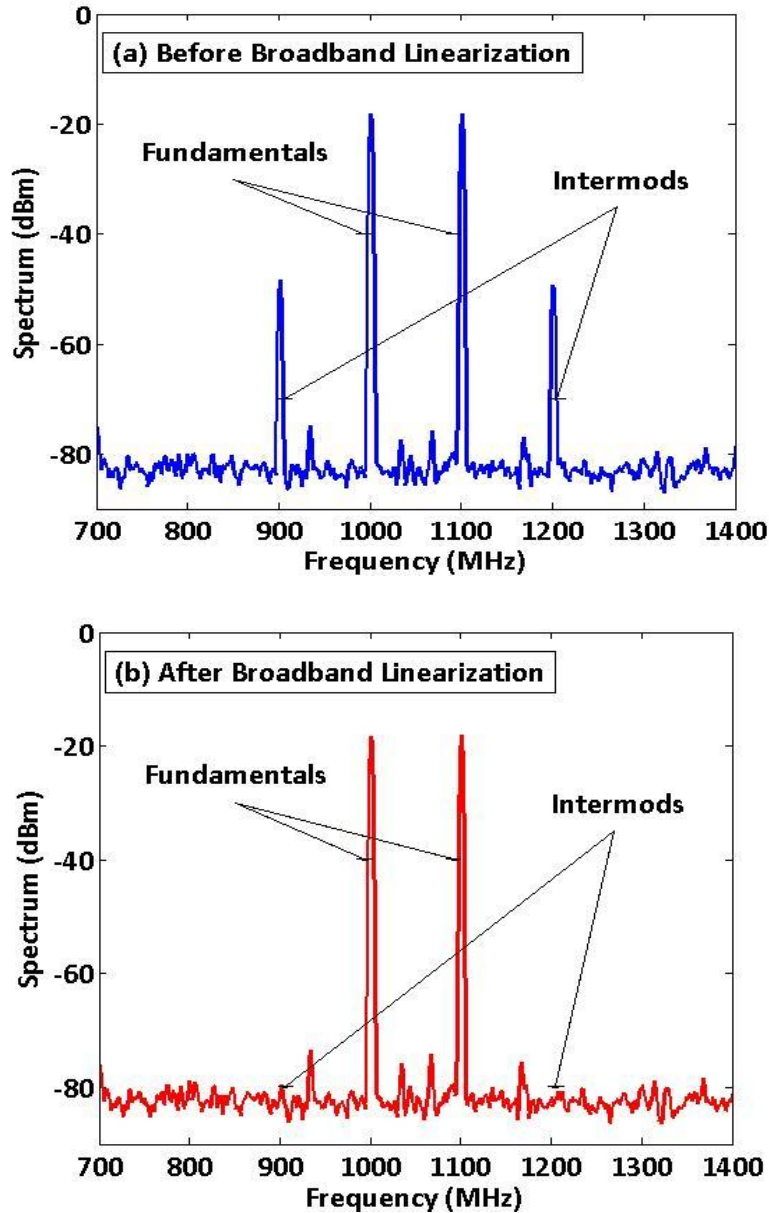
Figure 3.6. Third-order intermodulation product suppression is observed. (a) Prior to digital broadband linearization we have two third order tones. (b) After digital broadband linearization we observe 35 dB of third-order suppression.
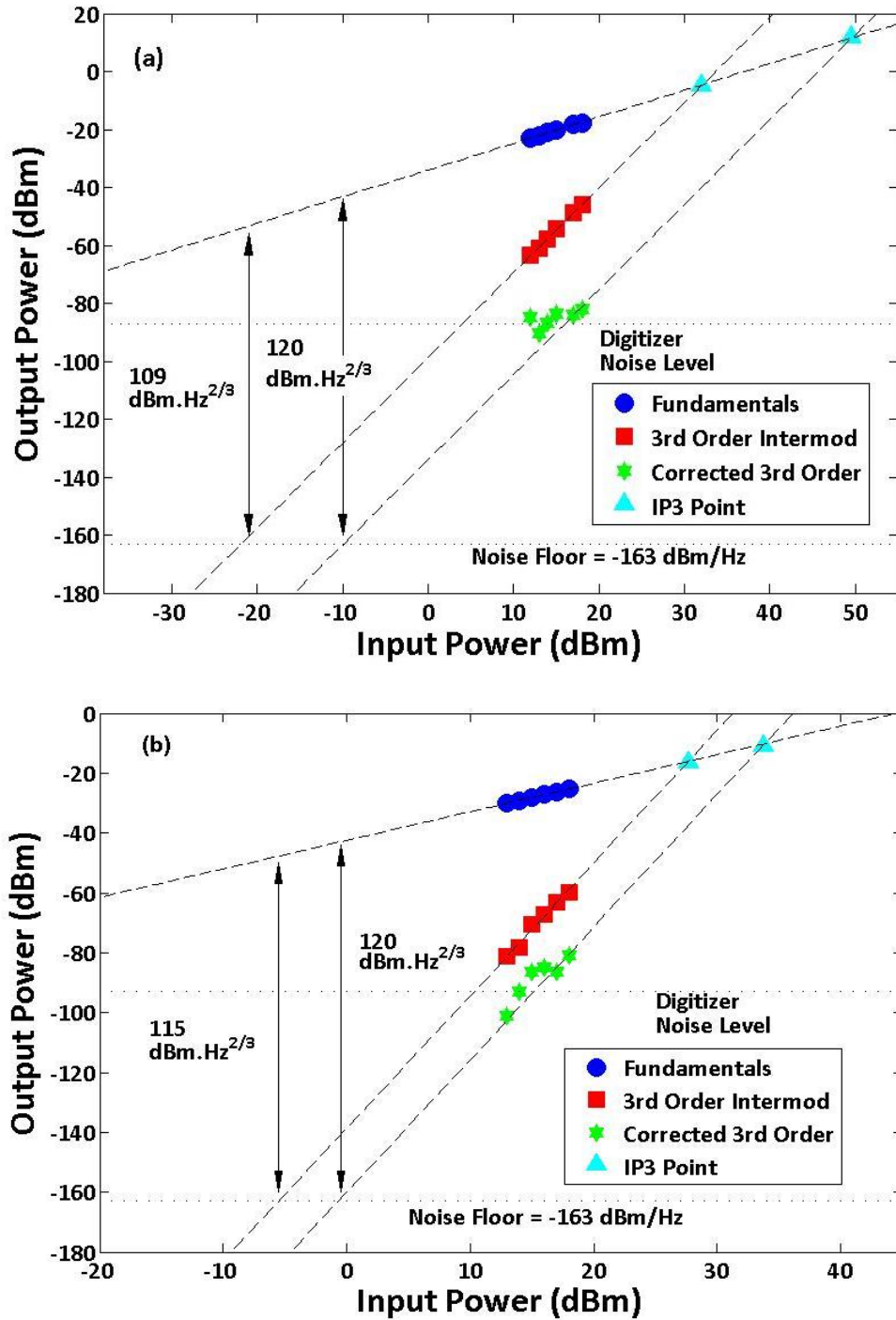
Figure 3.7. Output power versus input power for two different frequency sets. (a) Fundamental

tones at 1 and 1.1 GHz, resulting in third-order intermodulation distortions at 900 MHz and 1.2

GHz. (b) Fundamental tones at 6 and 6.1 GHz, resulting in third-order intermodulation

distortions at 5.9 and 6.2 GHz [32].

Since our technique is performed in digital domain, it is imperative to evaluate the impact of digitizer noise (i.e., quantization noise) on the performance of the broadband linearization technique. In order to do so, we calculated the signal to noise ratio (SNR) at the input before and after the algorithm. The input signal is already digitized by the system so it includes quantization noise prior to using the algorithm. We observed that across the 6 GHz bandwidth, we had an average SNR degradation of 0.5 dB. This is due to the algorithm being designed to mitigate nonlinear distortions and not uncorrelated white noise. Generally, the amount of noise not taken into account by the emulator may increase as we propagate through several stages of the algorithm.

3.5 Benefits and Comparison with Notable Benchmarks

Furthermore, our broadband linearization method is a digital technique, which means no additional hardware is required. It also works with time-domain representations of the RF signal, making it hardware friendly for real-time implementations. It hence can be implemented using field programmable gate arrays (FPGAs), which are capable of handling high data rates and performing complex algorithms on the data. Moreover, as opposed to conventional digital correction techniques, our presented technique performs distortion correction by re-generating the distortion components in digital domain, and subtracts them from the captured signal. Hence, it only requires digitization of fundamental frequency components, which obviates need for capturing excessive analog bandwidth at the electronic back-end. In other methods, the other frequency components over a wide bandwidth need to be captured. In the table below we show a table which compares some notable benchmarks of optical links with the largest SFDR. As we can see, we are able to achieve 120 dB.Hz$^{2/3}$ over 6 GHz of analog bandwidth while also using an average photocurrent of 1 mA which is typical of standard links.

Experiment	Bandwidth	SFDR	NF	Avg. Photocurrent
Betts	1 MHz (centered at 500 MHz)	132 dB.Hz$^{4/5}$	27.7 dB	0.94 mA
Chou, et al.	160 kHz	124.3 dB.Hz$^{2/3}$	42 dB	3.13 mA
Li, et al.	Up to 100 MHz	134 dB.Hz$^{2/3}$	14 dB	100 mA (total of both PDs)
Ackerman	Up to 2.5 GHz	122 dB.Hz$^{4/5}$ (75 dB was in 1 MHz inst. BW)	39.5 dB	8 mA (total of both PDs)
Lam, et al.	DC - 6 GHz	120 dB.Hz$^{2/3}$	23 dB	1 mA

Table 3-1. Benchmark comparisons of the digital technique with other broadband linearization techniques [32], [52]-[54], [64].

3.6 Conclusion

In conclusion, we proposed and demonstrated a broadband linearization technique that is an effective way of suppressing nonlinear distortions for a known nonlinear system. Using this technique, we experimentally demonstrated record spurious-free dynamic range of 120 dB.Hz$^{2/3}$ over 6-GHz of analog bandwidth. This technique can be expanded to real-time systems since this algorithm can be utilized in the time domain making it hardware friendly.

Chapter 4

Real-Time Simulation of Digital Broadband Linearization Technique

In the previous chapter, a digital post-processing linearization technique was demonstrated to efficiently suppress dynamic distortions added to a wideband signal in an analog optical link. To make this algorithm useful in a real-world application, the technique needs to be implemented onto a field-programmable gate array (FPGA) which allows for fast computation and real-time correction of these distortions. This chapter will discuss the aspects of implementing a real-time system and discuss the architecture required to implement the digital broadband linearization algorithm onto a FPGA. A Matlab simulation of the real-time implementation of this technique was developed, and the FPGA implementation was done using Verilog, a hardware description language. The performance of this algorithm was simulated in iSim and compared to a Matlab simulation of the real-time implementation. The two simulations show similar performance in suppressing third order intermodulation distortions by about 17 dB.

4.1   Introduction to Field Programmable Gate Arrays

The FPGA has been an important and ubiquitous device since its invention in 1985. It has been slowly incorporated into essentially every facet of technology that requires real-time application or fast computation. Many applications today take advantage of the power of the FPGA such as aerospace and defense systems, audio and broadcasting equipment, medical imaging devices, wireless communications, and video and image processing hardware, and medical to name a few [65]. The FPGA is a programmable semiconductor device that is based around a matrix of configurable logic blocks connected through programmable interconnects [65]. These are different from application specific integrated circuits (ASICs) where the device is custom built for a particular design, FPGAs can be programmed to a desired application or functionality.

The true power behind this device is in its computation power and its ability to process large amounts of data in parallel. Its millions of logic gates allow it to implement complex computations, and it can be reprogrammed if required for another application. FPGAs allow designers to change their designs very late in the design cycle–even after the end product has been manufactured and deployed in the field. In addition, Xilinx FPGAs allow for field upgrades to be completed remotely, eliminating the costs associated with re-designing or manually updating electronic systems [65]. As FPGAs evolve and are developed, many now have embedded processors transforming these devices into systems on a chip [66].

As the FPGA continues to increase in popularity, one of the many challenges application engineers face is programming in Register Transfer Level (RTL) despite many are experienced in higher level languages [67]. Many companies have attempted to ease this transition by writing hybrid programs in which a higher level language can be translated into RTL. However, the hardware description language (HDL) produced usually is inefficient compared to writing it

strictly in RTL. Companies such as Xilinx and Mathworks have started addressing this issue by developing user-friendly methods, such as interactive graphical user interfaces, for designing logic blocks and linking them together in order to make it easier for beginners to learn FPGA development and make it more efficient for advanced developers. By utilizing Matlab Simulink and Xilinx's System Generator, one can design a circuit in Simulink and export the logic block using Mathwork's HDL Coder [68]. This will generate the RTL that can be exported to FPGA.

4.2   Matlab Simulation of Real-time Digital Broadband Linearization

Before implementing onto a FPGA, a model for the single stage broadband linearization algorithm was designed and implemented in Matlab. As shown in Figure 4.1 in the blue box, a model of the optical link was generated and the green box highlights the part coded onto the FPGA. In this model, two sine wave generators set at approximately 1 GHz and 1.1 GHz were used and combined to form a modulated signal. These two frequencies were chosen to be consistent with the offline Matlab demonstration of the digital broadband linearization code. The combined signal was sent through the system emulator to simulate sending the original signal through the optical link and to add the nonlinearities generated as the signal propagates. The resultant signal is then sent through a simulation of the FPGA programmed with the digital broadband linearization algorithm shown in the green box. Inside the FPGA, the signal is sent through a copy of the system emulator, and then coefficients are multiplied against the digitized signal and the resultant signal from the emulator. The corrected signal is obtained by summing the two signals, and its performance can be evaluated by viewing the spectrum.
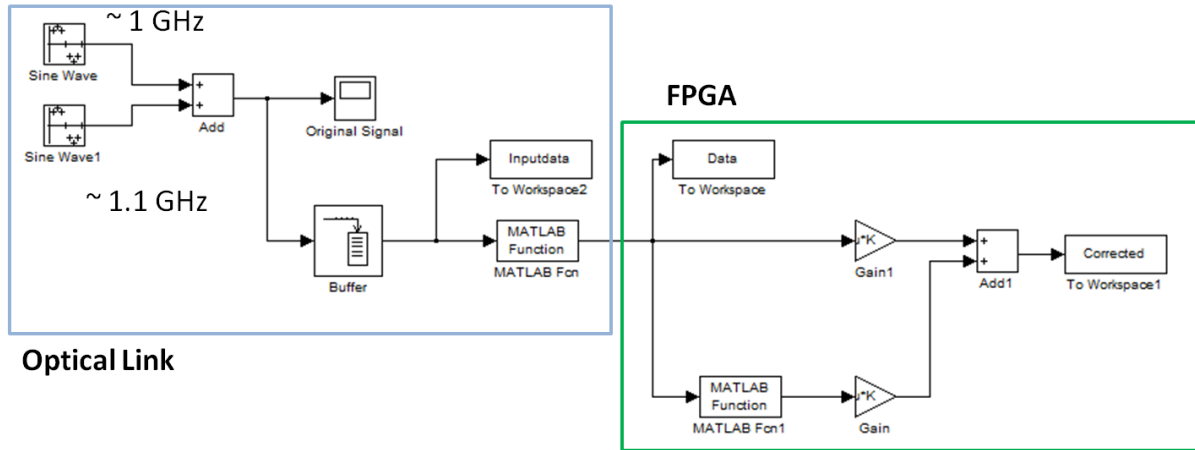
Figure 4.1. Simulink Model of the broadband linearization algorithm.

During the design of the simulation, adjustments had to be able to model the FPGA. This meant that functions typically used in higher level languages could not be used, and values needed to be changed to single precision instead of floating point. The optical link emulator had to be adjusted so that it could perform with the same functions readily available for the FPGA. Furthermore, values had to be truncated to model the limited bit representation. Values that have long significant digits such as π had to be truncated to nearest bit representation. To verify the Simulink model is working, the results are plotted as shown in Figure 4.2. After a single stage, 18 dB of suppression of the third order intermodulation products is observed verifying the Matlab simulation of the real-time implementation is able to suppress distortions.
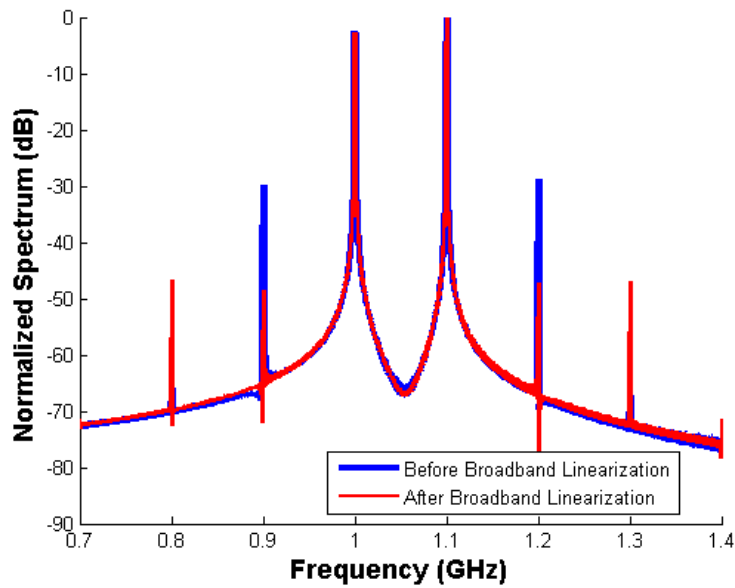
Figure 4.2. Simulink simulation results showing about 18 dB of improvement from a single

stage.

4.3 Digital Broadband Linearization FPGA Architecture

The next step is to design the architecture in order to implement the digital broadband linearization technique on a FPGA for real-time correction. The architecture for a real-time FPGA implementation of the algorithm is shown in Figure 4.3 and follows the block diagram of the digital broadband linearization technique [60]. An analog input signal is digitized by an onboard ADC. The digitized samples are normalized in amplitude by a normalization block. From here the data is divided into two paths. In the top path, the normalized data is buffered and in the second path the data is applied to the optical link emulator. The buffer is used to hold the data so that when the two paths are recombined at the multiply and accumulate block, the data are in time. The output of the link emulator block undergoes normalization and is combined with the original normalized data at the multiply and accumulate block. The multiply and accumulate

47

block multiplies the inputs from both paths with a gain and adds them to produce an improved

signal with less distortion. This implementation can be extended to multiple stages for improved

distortion correction for strong nonlinearities and higher order distortions. A detailed description

of each block can be found in Appendix A.
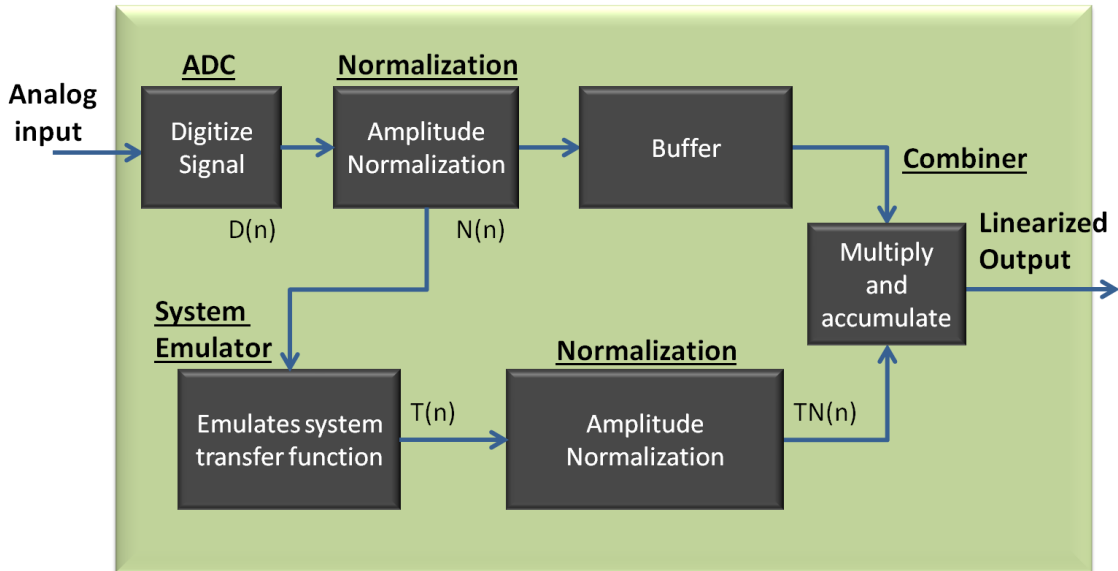
Figure 4.3. Block diagram of a single stage of the broadband linearization algorithm. It can be expanded to multiple stages.

One of the many challenges in implementing this algorithm into real-time was to transfer the

algorithm written in Matlab to Verilog. Initially this was done by developing the algorithm in

Mathwork's Simulink by linking premade Xilinx blocks and using HDL coder to generate the

Verilog code. Some of the blocks developed worked in simulation, but if the block did not work,

the computer generated code was difficult to debug. In other cases, the block worked in

simulation, but it did not work on the FPGA which may be due to timing issues and how the

blocks are connected. Again, code automatically generated by Simulink was difficult to fix and

debug. In the end, the entire architecture was written in Verilog for simplicity and making it easier to debug and more efficient with less extraneous code from the HDL coder.

4.4   Simulation Comparisons of Experimental Data

In order to demonstrate a highly linear optical link using our digital broadband linearization technique, an externally-modulated direct-detection optical link was built with a FPGA at the output to digitize the signal. The link uses a continuous-wave laser (Orbits Lightwave Inc.), which provides 7-mW of low-noise optical power at 1.55 μm. The optical signal is directed to a Lithium-Niobate Mach-Zehnder modulator (EO Space EO modulator), where the optical signal is intensity modulated by the radio frequency analog signal. To minimize even-ordered distortions, the electro-optic modulator is biased at the quadrature point. The resultant optical signal is then transmitted through 20.56-km of standard single-mode fiber (SMF-28). The long SMF-28 emulates a practical application, where the radio frequency signal is transmitted and received in a remote site. This is particularly important because in presence of dispersion, the nonlinear distortions become dynamic (i.e., with memory effect), which results in significant frequency-dependent nonlinear distortions. Finally, the modulated optical signal is detected by a PIN photodiode (Optilab, LR-12-AM) with a responsivity of 0.85 A/W. The photo-current was found to be 1mA. Hence, our system exhibits ~22 dB of gain from input to output (without pre- and/or post-amplification). The resultant signal is digitized and will undergo signal processing using a commercial FPGA (SP Devices ADQ108).

In this evaluation, the FPGA digitized the signal and the output collected will serve as the input to both the Matlab and Verilog simulations to test how well the algorithm works with real

data. A two-tone signal with fundamental frequencies at 1 and 1.1 GHz was inputted to the link. This gives the third order intermodulation distortion products at 0.9 and 1.2 GHz. The output file from the FPGA was inserted into the Matlab and Verilog simulations to (1) verify that the Matlab and Verilog codes were similar and (2) demonstrate third-order intermodulation distortion product suppression. After plotting the spectrum, it is evident that the performance of the two is very similar. Both spectrums shown in Figure 4.4 look similar, and they both show about 17 dB of third order intermodulation distortion product suppression.

MATLAB Simulation of Real Time Linearization
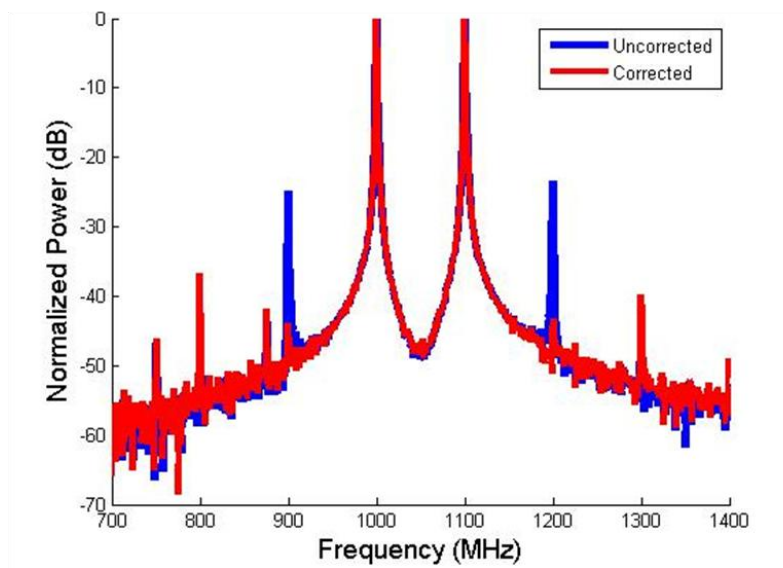
Verilog Simulation of FPGA
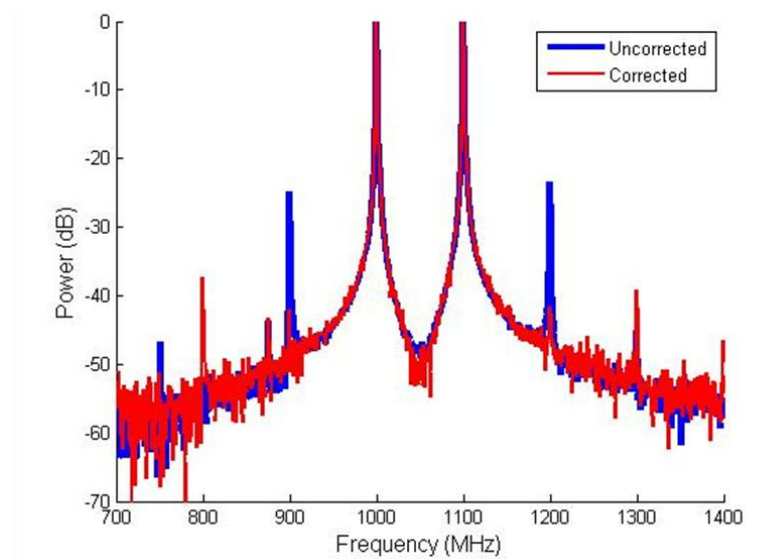
Figure 4.4. Matlab (top) and Verilog (bottom) simulation of real data show IMD3 suppression of

about 17 dB. The blue curve shows the spectrum before digital broadband linearization

(uncorrected) and the red curve shows the spectrum after digital broadband linearization

(corrected).

4.5 Future Work

The digital broadband linearization technique is shown to work on a FPGA simulator and matches with the Matlab simulation results. Despite the simulation was written in Verilog and able to compute the corrected output, actual implementation on FPGA hardware proved very difficult and hard to debug. There were internal timing issues that are beyond the expertise of the author and several blocks were unable to function, notably the normalization block. There is interest in pursuing a joint venture with an outside vendor for implementing the digital broadband linearization algorithm on a FPGA for real-time demonstration through the Office for Naval Contracts small business innovation research program. Additionally the multi-stage version of this algorithm can be implemented. By being able to use the algorithm in real-time, this makes the technique much more useful for real-time correction to improve the dynamic range of the optical link.

Chapter 5

Ultra-wideband Instantaneous Frequency Estimation

Determining the instantaneous frequency of a signal is required for many applications ranging from radio astronomy to military equipment. Unfortunately, the scan rate over a wideband spectrum is often too long compared to the time scale of the frequencies of interest. A time-stretched instantaneous frequency measurement receiver is presented which is capable of simultaneous measurement of multiple frequencies and amplitudes across an ultra-wide instantaneous bandwidth. The high effective sampling throughput of the system provides high temporal resolution of the signal, and frequency and amplitude estimation capability is improved through signal processing. This system has the flexibility to be modified to adjust its instantaneous bandwidth and frequency resolution. It also has an ultra-fast sweep time and reduced hardware complexity compared to other instantaneous frequency measurement systems.

5.1   Introduction to Instantaneous Frequency Measurements

Instantaneous frequency measurement (IFM) receiver has been an increasingly important tool for measuring radio-frequency (RF) signals over a wide bandwidth. It is used to measure RF frequency, amplitude, pulse width, and time of arrival for a plethora of applications such as radar threat detection, electronic warfare, and signal intelligence [69]-[70]. A wideband IFM receiver offers the high probability of intercept over wide instantaneous RF bandwidths, high dynamic ranges, good sensitivity and high frequency measurement accuracy. Currently IFM receivers are limited in performance mainly by their ability to only measure single frequencies at a time, and have limited bandwidths with very slow sweep times across enormous bandwidths. Additional channels would be required to expand the bandwidth which would increase hardware complexity. The time-stretch instantaneous frequency measurement receiver (TS-IFM) is able to overcome these challenges and provide a solution capable of ultra-fast sweeping across enormous bandwidths to perform measurements on transient signals. Today's spectrally cluttered environments demand a system that can perform measurements across wider bandwidths and also detect frequencies of interest quickly and efficiently.

Traditional IFMs use microwave interferometers and make use of hybrid couplers, power dividers, and delay lines to perform measurements [71]. The basic measurement technology consists of a microwave correlator to measure an unknown signal [70]. A traditional IFM, shown in Figure 5.1, will split the incoming signal into two paths and delay one path by a time τ with respect to the other along with a 90 degree phase shift. Subsequently the ratio of the two paths is taken and then an arc-tangent operation is performed to determine the input frequency of the received signal.
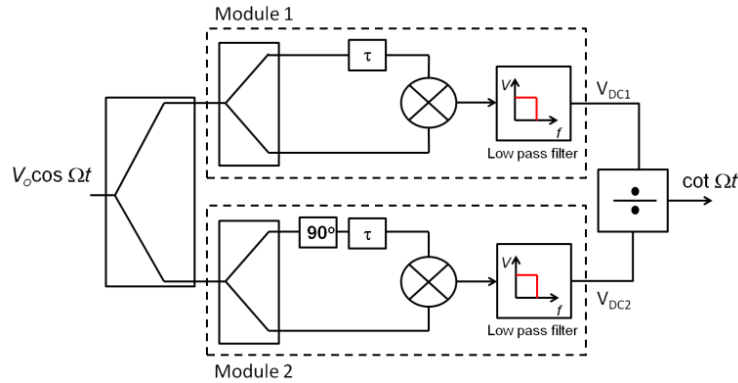
Figure 5.1. Block diagram of a traditional instantaneous frequency measurement system [72].

A limitation of using this method is that it can only measure a single frequency at a time and measuring amplitude requires another set of discriminators. While there may be other signals in the band, the IFM receiver only measures the largest RF signal in the band [69]. Moreover, the largest signal must also be several dB greater than the others and two signals cannot be too close in both frequency and amplitude otherwise estimation errors would occur [70]. IFM systems have reduced bandwidths to measure multiple frequencies and also require a series of filters and post-processing to measure each frequency component accurately. Also, it is difficult to realize broadband performance because of the bandwidth limitations of the RF components. Most IFMs have an instantaneous bandwidth of only 1-4 GHz.

Digital IFMs (DIFM) have recently become popular and provide several major upgrades to analog approaches. DIFMs are capable of having wider instantaneous bandwidth than analog devices, can detect multiple frequencies, measure complicated signals, and do not rely on physical delay lines [73]. Digital frequency measurement uses a digital filter bank and several channels to perform the measurement. It also requires a local oscillator to down convert the signal to an intermediate frequency and a high speed digitizer to sample the signal. An advantage of using DIFMs is that the signal processing backend allows for easier implementation of digital

delays and typically several delays have to be implemented for performing more accurate measurements. DIFMs require several successive stages where each stage determines a frequency using a correlator [74]. Errors can occur when the frequency is close to the time delay hence to avoid this problem, different time delays are utilized [75]. The necessity of this method requiring multiple stages to accurately measure a frequency makes it computationally intensive. DIFM performance is also limited by the sampling rate and resolution of the analog to digital converter (ADC), jitter in the electronics, and quantization errors.

Recently, there has been work on employing photonic devices to perform IFM exploiting the inherent wide bandwidth. Many photonic systems using correlation methods to measure a single frequency have been demonstrated [76]. Various research groups have achieved multiple frequency measurements by mixing nonlinear terms [77], utilizing multiple optical delay channels [78], and using frequency to time mapping [79]. While these techniques can perform frequency measurements, they are incapable of measuring both frequency and amplitude without requiring additional hardware. Furthermore, their frequency resolutions are not narrow enough and are typically on the order of several gigahertz.

5.2 Time-Stretch Instantaneous Frequency Measurement Receiver

We propose the time-stretch IFM receiver that is capable of rapidly measuring multiple signals simultaneously (within hardware and software constraints) over an ultra-wide bandwidth. Time-stretching compresses the signal bandwidth which allows for rapid spectral sweeps across an enormous bandwidth to be digitized using slower analog to digital converters. The TS-IFM captures a segment of real-time data on which we can apply Fast Fourier Transform (FFT) to analyze in the spectral domain. This allows us to perform multiple frequency and amplitude

measurements over an ultra-wide bandwidth. The frequency resolution for the system is limited by the short capture window and the number of points used for the FFT. However, the capture time window can be adjusted which allows for frequency resolution tuning. The accuracy of frequency estimates is further improved by windowing the sampled signal data and performing quadratic interpolation on the signal peaks in the frequency domain [19]. In this section, we demonstrate TS-IFM frequency detection capabilities by performing frequency measurements across a wide bandwidth and simultaneous multiple frequency measurements without requiring additional hardware or cascading filter designs. The time-stretch IFM is the union of time-stretch enhanced recorder (TiSER) and digital signal processing that performs windowing on time domain sampled data and frequency interpolation on the signal peaks. The combination of the two allows for a high resolution, wideband, low power instantaneous frequency measurement receiver.

The front-end of the time-stretch IFM is TiSER, shown in Figure 5.2, which uses time-stretch to capture ultrafast signals [11],[12]. Using this system we are able to take an ultrafast RF input signal and stretch it in time which then allows a slower ADC to digitize the signal with high fidelity in real-time. In the system, a short optical super-continuum (i.e. broadband) pulse is chirped by propagating through dispersive fiber which performs a frequency to time mapping as indicated by the rainbow pulses in Figure 5.2. The RF input signal is intensity modulated onto the chirped optical pulse using an electro-optic modulator. This modulated pulse is sent through a second dispersive fiber which linearly stretches out the signal in time, compressing its analog bandwidth. The amount of stretching is defined as $M = 1 + D_2/D_1$ where M is the stretch factor and D_1 and D_2 are the dispersions of the two dispersive fibers. The stretch factor is the factor by which we compress the signal bandwidth. At the backend of TiSER is an ADC which digitizes

57

the stretched RF output signal from the photo-detector (PD). Compressing the bandwidth using time stretch allows a slower, low power ADC with lower bandwidth and higher resolution to digitize the signal with very high temporal resolution thus giving a large effective sampling throughput. By slowing down signals before digitization, TiSER performs instantaneous spectral sweeps across an enormous bandwidth otherwise the ADC would have captured only a small slice of the full spectrum. Furthermore, the time-stretch system exhibits very low aperture jitter due to the stretching of the signal and the low laser jitter.
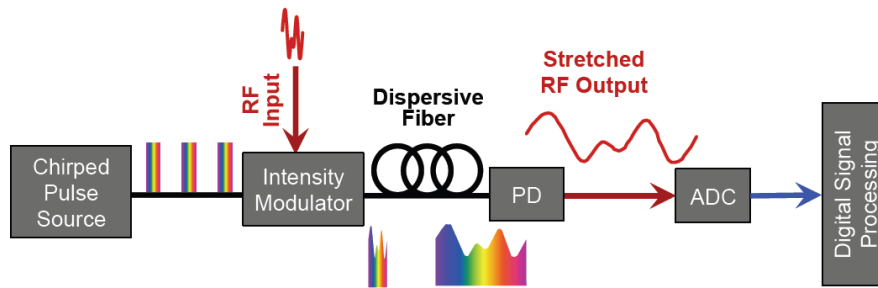
Figure 5.2. Time-Stretch IFM Receiver block diagram [80].

Each chirped laser pulse captures a short real-time segment of the RF signal and each these pulses are time-stretched and digitized by an ADC. This kind of sampling gives rise to TiSER's unique real-time burst sampling modality where a signal is sampled in high temporal resolution bursts. By adjusting the first dispersive element, we can increase or decrease the time aperture for our signal capture window. This allows for narrower or wider frequency resolution that can be resolved by the system. The time aperture, T_A, is given by $T_A = \Delta\lambda D_1$ where $\Delta\lambda$ is the laser bandwidth and D_1 is the dispersion parameter of the first dispersive fiber.

The photonic front-end of the TS-IFM receiver is fundamentally a modified optical link and power sensitivity is limited either by the intensity modulator or by dispersion penalty [11],[12]. In dispersion penalty, a signal is modulated onto a chirped pulse and transmitted

58

through the optical fiber. The modulator produces upper and lower sidebands of the RF signal in the optical spectrum at frequencies of $\omega_{optical} \pm \omega_{RF}$. In the absence of dispersion, these sidebands beat with the optical carrier at the photo-detector to reproduce a copy of the signal. Since dispersion is present, the upper and lower sidebands slip in phase with each other and interfere at the photo-receiver, creating nulls at certain frequencies [12]. This produces a periodic fading characteristic versus frequency as shown by Figure 5.3 (although the fading can be eliminated using a variety of techniques [12] whose discussion is beyond the scope of this work). In the TS-IFM with dispersion parameter β_2, second dispersive fiber length L_2, and angular frequency ω_{RF}, the transfer function is given by [11], [12]

$$H(\omega) = \cos\left(\frac{\beta_2 L_2 \omega_{RF}^2}{2M}\right). \tag{5.1}$$

In addition to IFM, the time stretch technique has been used in other applications. A new type of bright-field camera known as time-stretch microscopy [14] has demonstrated imaging of cells with record shutter speed and throughput leading to detection of rare breast cancer cells in blood with one-in-a-million sensitivity [16]. Used for single-shot real-time spectroscopy, the time stretch technology led to the discovery of optical rogue waves, bright and random flashes of white light that results from complex nonlinear interactions in optical fibers [17].
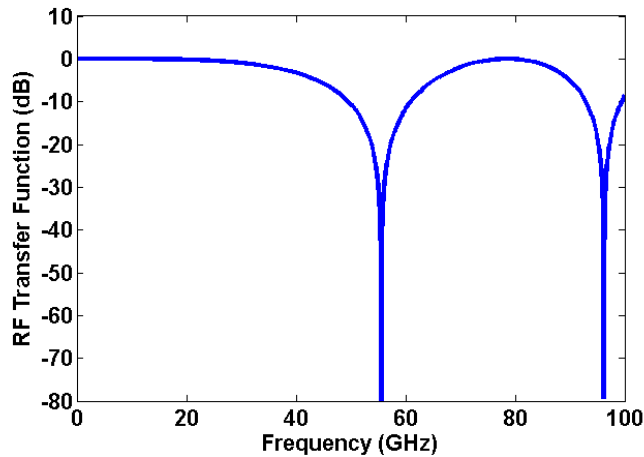
Figure 5.3 Dispersion penalty behavior in the Time-stretch IFM.

Digital signal processing is performed on the time-stretch ADC sampled data for improving accuracy for frequency and amplitude estimation. From each time-stretched pulse, we are able to digitize a short real-time segment of the signal due to TiSER's real-time burst sampling, which allows us to perform analysis in the spectral domain. When performing a Fast Fourier Transform (FFT) of this short time segment, the frequency resolution is limited by the time aperture of TiSER and by the number of digitized sample points prior to computing the FFT which is dependent on the sampling rate of the back-end electronic ADC.

In the early 1980s, Madni demonstrated, in a transmission line analyzer that uses both frequency domain reflectometry and digital signal processing algorithms to determine the true amplitudes and frequencies of multiple mismatches in waveguide and co-axial transmission lines [19],[81]-[84], spectral leakage as well as frequency and amplitude inaccuracies occur due to two primary reasons. The first is due to the sampling of a non-integer number of cycles because sampling starts and stops arbitrarily at some given points on the signal rather than at a pre-determined starting and stopping point. This non-integer cycle sampling creates abrupt edges at the start and stop sampling of the signal which in turn results in spectral leakage. One way to reduce this leakage is to window [42] the sampled signal so that the weighting function at the edges is close to zero while the weighting function gradually approaches "1" in the center when the cycles are complete and the amplitude is maximized. A second reason is due to the finite number of samples digitized in time domain that are taken prior to performing the FFT. To overcome this, a "quadratic interpolation technique" was also developed which looks at each peak in the FFT spectrum and its adjacent neighbors, and performs an interpolation on this triplet in order to better estimate the true amplitude and frequency of the original signal [81]. This

60

powerful technique can be extended to improve the frequency and amplitude estimation from time-stretch measurements as well.

The quadratic interpolation is used to provide a better frequency and amplitude estimation which is closer to the "true" frequency and amplitude [81]. A generic parabolic curve as shown below in Figure 5.4 and it follows the equation $s = af^2 + bf + c$.
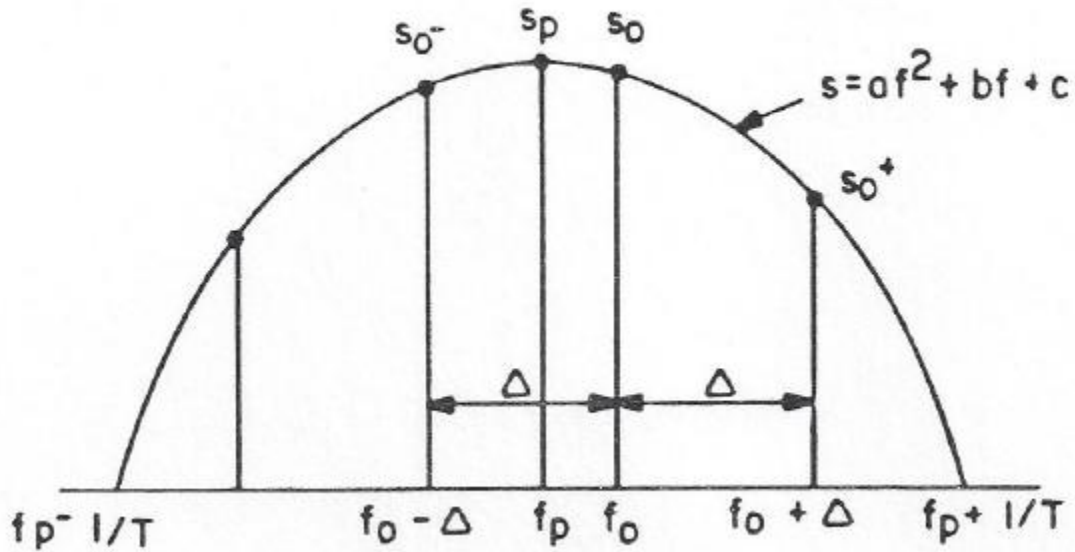
Figure 5.4. By using quadratic interpolation, the true peak frequency and amplitude can be found [81].

Given three points on the curve, s_o^-, s_o, and s_o^+, we can use these three points to calculate the peak and amplitude of the curve. The equation [81] for finding the peak frequency is given by the equation below

$$f_p = f_0 + \frac{(S_0^+ - S_0^-)}{2(2S_0 - S_0^+ - S_0^-)} \tag{5.2}$$

The equation [81] for finding the peak amplitude is given by the following equation

$$S_p = S_0 + \frac{(S_0^+ - S_0^-)^2}{8(2S_0 - S_0^+ - S_0^-)} \tag{5.3}$$

61

5.3   Matlab Simulation

The time-stretch IFM was simulated assuming experimental system parameters used this demonstration [80]. A single frequency tone was swept from 5 to 45 GHz. To show the effectiveness of the windowing and quadratic interpolation technique, the signal frequency was estimated with and without using this technique. The frequency error was calculated using the frequency estimated using a rectangular window and also by using a Hann window with quadratic interpolation. The simulation shows that with windowing and interpolation the frequency estimation error significantly reduced compared to just using a rectangular window. For over 40 GHz of instantaneous bandwidth, we achieved an error of ±125 MHz which a ten-fold improvement in spectral resolution [80].
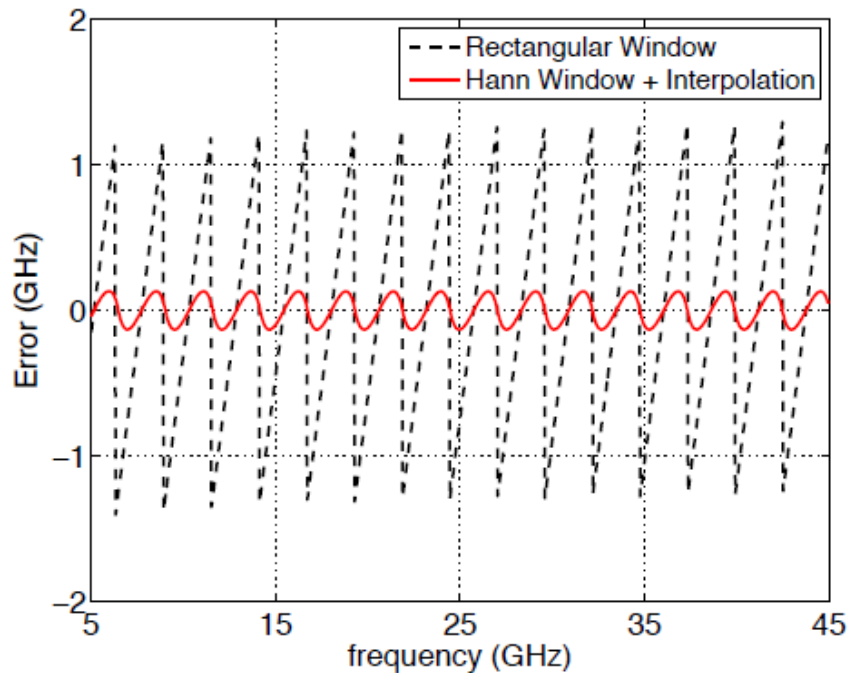
Figure 5.5. TS-IFM frequency estimation simulation which shows using quadratic interpolation significantly reduces the frequency error [80].

5.4   Experimental Results

To evaluate our system performance, we built TiSER using a chirped super-continuum source with $\Delta\lambda$ = 18 nm, a first dispersive fiber with dispersion of -20 ps/nm, a 40 Gbps Lithium Niobate electro-optic intensity modulator, a second dispersive fiber with dispersion of -984 ps/nm, and a 13 GHz bandwidth photodiode. A 3 GSa/s analog to digital converter is used to digitize the signal. The stretch factor and the time aperture depend on the amount of dispersion and the optical bandwidth [11], [12]. Using these dispersion parameters, we get a stretch factor of 50 giving an effective sampling rate of 150 GSa/s. For tuning the frequency resolution by changing the time aperture, the first dispersive fiber was changed to -40 ps/nm and -100 ps/nm for stretch factors of 25 and 10 respectively. The power sensitivity in this demonstration is limited by the Lithium Niobate electro-optic modulator in which 6 dB is lost over 30 GHz. Since each laser pulse captures a short window of the signal in time, we effectively are sweeping over a wideband spectrum. The laser pulse repetition rate of 36.6 MHz gives us a sweep time of 27 ns, and real-time burst sampling modality of TiSER would allow for detection of transient signals that could be missed by conventional IFMs.

To demonstrate improved frequency estimation accuracy and to show the enormous instantaneous bandwidth of the system, we performed a single frequency estimation experiment from 5 to 45 GHz. The signal was then digitized, a windowing function was applied to the digitized samples of the time-stretch signal, and quadratic interpolation was performed on the peaks in the frequency domain. As can be seen in Figure 5.6, we are able to closely estimate the input frequency using the TS-IFM and Figure 5.7 shows the frequency estimation error. Across 40 GHz, we achieve a root-mean-square (rms) error of 97 MHz.
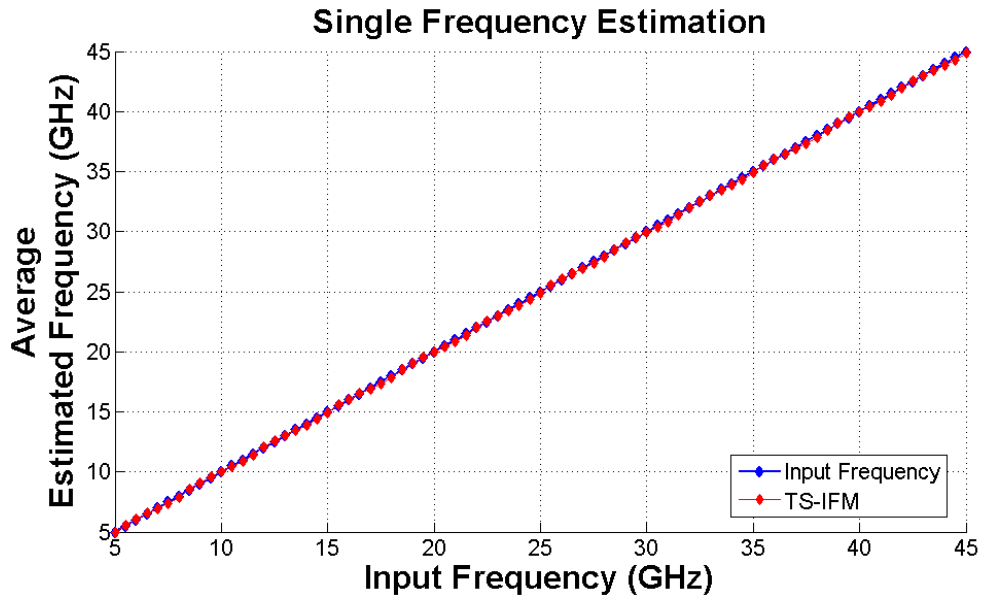
Figure 5.6. A single frequency tone was swept from 5 GHz to 45 GHz.
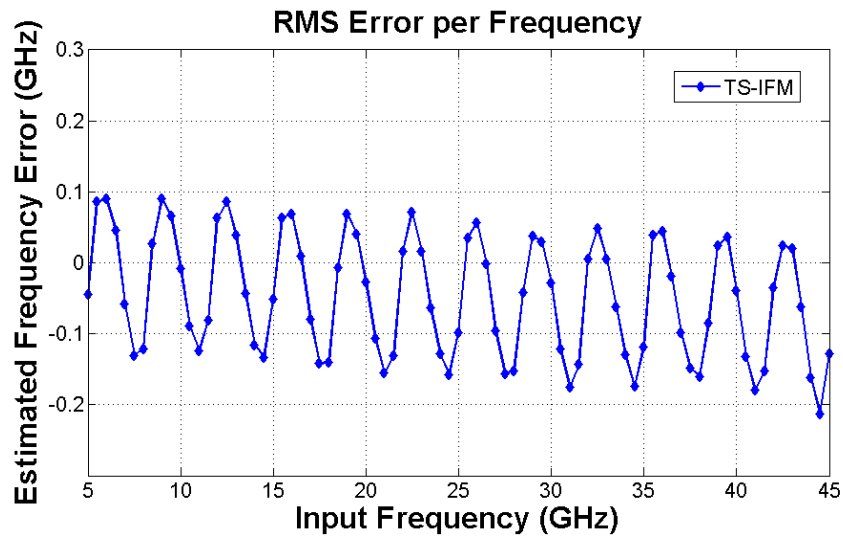
Figure 5.7. Estimated frequency error of 97 MHz rms is achieved using the TS-IFM receiver.

For multiple frequency estimation, we demonstrate the capability of the TS-IFM to measure multiple tones simultaneously given the frequency spacing of the two tones are greater than the FFT frequency resolution. We performed a two tone test using the TS-IFM for 10 GHz

and 30 GHz. Figure 5.8 shows how quadratic interpolation is applied to the peak for improved frequency estimation. The TS-IFM receiver estimated the tones at 9.96 GHz and 30.01 GHz as shown in the same figure. We also demonstrate the flexibility of the system in tuning the system bandwidth and frequency resolution by modifying the dispersion for the first dispersive fiber to provide a narrower frequency resolution. In Figure 5.9 and Table 5-1 we show scenarios of how changing the first dispersive fiber changes the time aperture and thus the frequency resolution. By changing the frequency resolution, the TS-IFM receiver can better resolve two tones closer together. The first dispersive fiber was modified to obtain a stretch factor of 10 giving a longer time aperture, and tones at 8 GHz and 9 GHz were input to TS-IFM. We were able to resolve these two tones even when their amplitudes were over 10 dB apart and provide better frequency estimation as shown in Figure 5.10 and Figure 5.11. The frequencies were estimated to be 8.09 GHz and 9.15 GHz.
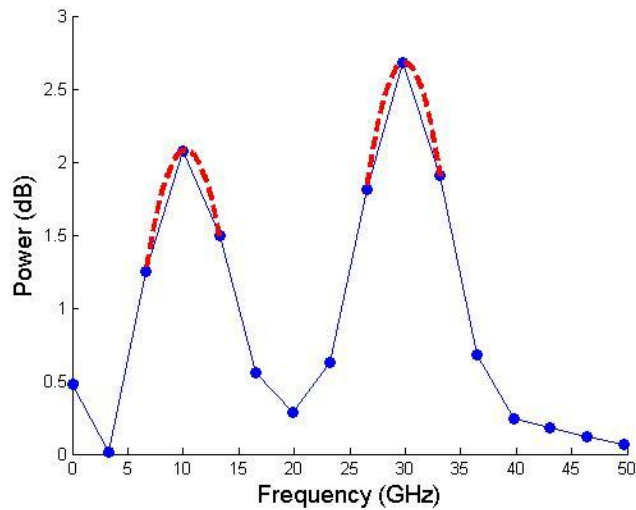
Figure 5.8. Dual tones input at 10 GHz and 30 GHz. TS-IFM estimated the frequency of the tones to be at 9.96 GHz and 30.01 GHz.

(a)

(b)

66
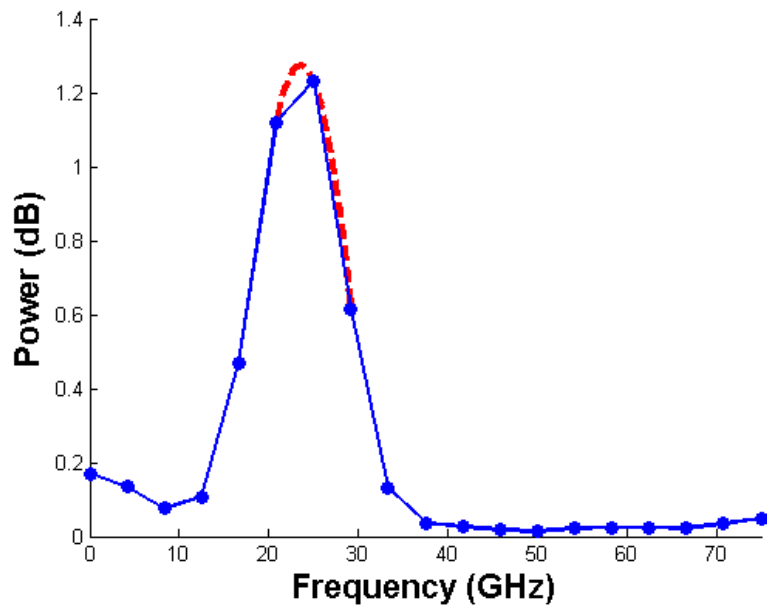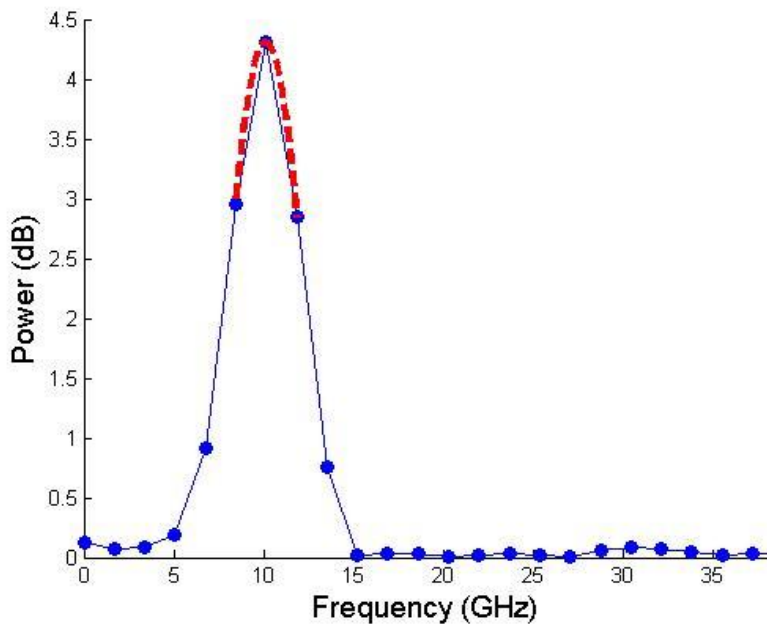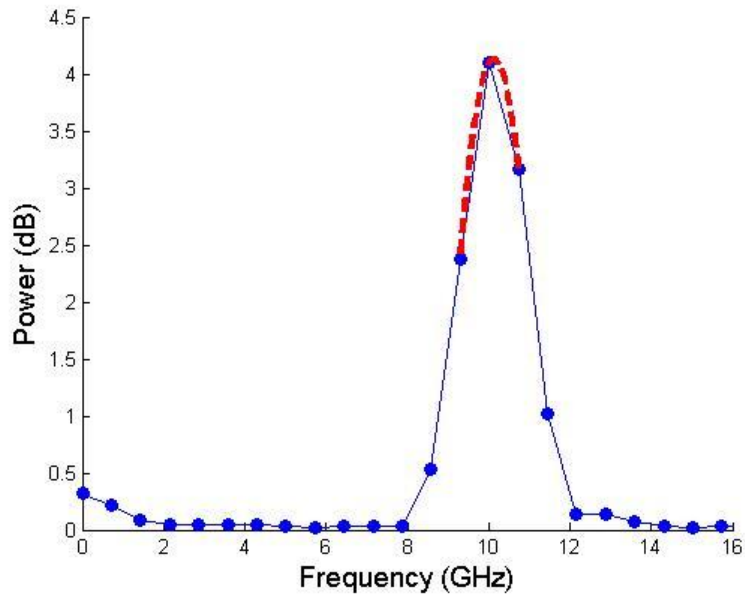
(c)

Figure 5.9. Plots 5.9(a)-(c) depicts how changing the first dispersive fiber allows for tuning of

frequency resolution.

Table 5-1. Tuning TS-IFM for bandwidth and resolution

Plot	Δf (GHz)	DCF 1 (ps/nm)	Time Aperture (ns)	Stretch Factor	Nyquist Frequency (GHz)
5.9a	3.31	-20	0.3	50	75
5.9b	1.69	-40	0.6	25	37.5
5.9c	0.72	-100	1.5	10	15

Table depicting how changing the first dispersive fiber allows for tuning of frequency resolution.
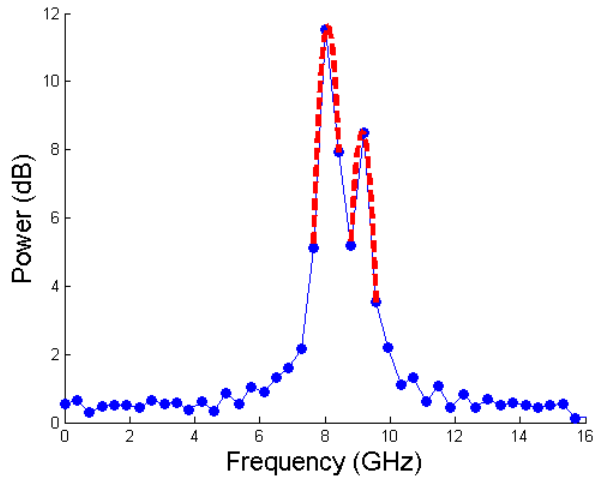
Figure 5.10. TS-IFM can resolve two tones close together and with similar amplitudes

simultaneously which is a challenge for current IFM receivers.
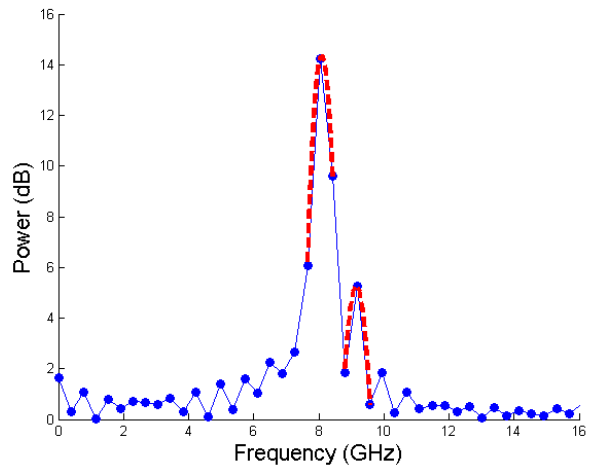
Figure 5.11. Dual tones input at 8 GHz and 9 GHz with high and low amplitudes. The system

was able to resolve these two signals and correct for signal frequency.

5.5 Benefits and Advantages of Time-Stretch Instantaneous Frequency Measurement Receiver

Time-stretch IFM receiver has several key advantages compared to commercial systems [86]-[88]. TS-IFM has the ability to perform frequency measurements across an ultra-wide instantaneous bandwidth with increased accuracy through windowing and quadratic interpolation. The fast sweep time allows for rapid spectral measurements across enormous bandwidths. Additionally, multiple frequencies can be estimated simultaneously without any additional filtering or cascading stages whereas current commercial systems do not have this capability. This makes the TS-IFM receiver very effective in spectrally cluttered environments and for quickly detecting transient signals. Moreover, the effective sampling throughput of TS-IFM receiver is significantly higher allowing it to capture signals with high temporal resolution due to its real-time burst sampling and uses less power than high speed ADCs with similar throughput thus reducing the electronic hardware complexity and cost. The TS-IFM can be implemented in real-time using field programmable gate arrays and could be used as a wideband cueing receiver for finer resolution systems. Further work can be done by calibrating the system for amplitude measurements and by implementing continuous time-stretch architecture to take longer collection times for better frequency resolution.

Chapter 6

Signal Integrity Measurements using TiSER

As electronic circuits and data speeds in communications continue to increase, the demand for high bandwidth digitizers have become paramount. It becomes more difficult to measure the integrity of the signal. By using time-stretch to slow down the signals, we are able to measure these high speed signals with higher fidelity. In this chapter, our approach to perform signal integrity measurements using time-stretch is presented. A discussion on the advantages of TiSER's unique real-time burst sampling modality and low system jitter will be given. Afterwards, we present how the signal integrity parameters are measured using TiSER and how these results match with commercial instruments. By matching with calibrated equipment results, we demonstrate TiSER can be used as a high speed measurement device.

6.1 Time-Stretch Enhanced Recorder

The time-stretch enhanced recorder (TiSER) uses the concept of time-stretch to stretch a quickly varying signal using group velocity dispersion by compressing its bandwidth or slowing down the signal spatially in time and digitizing the signal with high fidelity by using a slower, lower bandwidth ADC. A block diagram of the system is shown below in Figure 6.1.
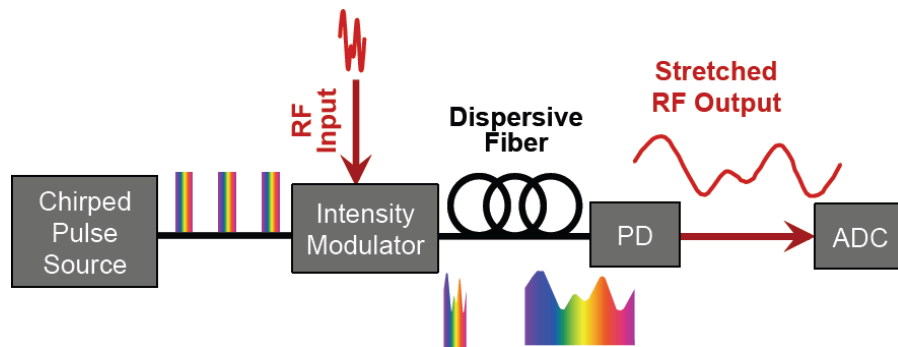
Figure 6.1. Block diagram of time-stretch enhanced recorder [80].

In the system, a short optical super-continuum (i.e. broadband) pulse is chirped by propagating through dispersive fiber which performs a frequency to time mapping as indicated by the rainbow pulses in Figure 6.1. The RF input signal is intensity modulated onto the chirped optical pulse using an electro-optic modulator. This modulated pulse is sent through a second dispersive fiber which linearly stretches out the signal in time, compressing its analog bandwidth. At the backend of TiSER is an ADC which digitizes the stretched RF output signal from the photo-detector (PD). A more detailed discussion of how TiSER works can be found in section 2.5 of this dissertation.

6.1.1 Real-time Burst Sampling Modality

When digitizing high speed signals, equivalent-time (sampling oscilloscopes) and real-time digitizers are employed. For sampling oscilloscopes, the signal is sampled on the order of megahertz frequencies and then reconstructed digitally requiring a long time to obtain the original signal in high fidelity. The bandwidths of sampling oscilloscopes can reach up to 100 GHz, but they are unable to capture non-repetitive signals. Even with repetitive signals, the obtained waveform is not in real-time. Real-time oscilloscopes have the ability to sample much faster on the order of gigahertz. However, these have input bandwidths limited on the order of a few gigahertz. By using TiSER, each chirped laser pulse is able to capture a small segment of the signal which then is digitized by an ADC. This gives rise to a unique real-time burst sampling modality since the signal is sampled in bursts like a high speed camera capturing frames.

In Figure 6.2, the different sampling modalities (equivalent-time, real-time, and real-time burst sampling) are compared. When using a sampling oscilloscope, the input bandwidth is very wide, but the signal is measured slowly on the order of megahertz giving no real-time capability. To reproduce the signal, the signal needs to be repetitive and it would take a long collection time. When using a real-time digitizer, the signal is sampled much quicker on the order of gigahertz, yet the problem with this method is the bandwidth is limited. TiSER is able to bridge these two technologies by combining both high speed sampling and wide bandwidth. By capturing segments of the signal rather than single points, TiSER has the ability to capture non-repetitive signals and rare events in single shots with very high temporal resolution. Having such a system would allow more insight to a signal quickly and allow us to see events such as transients that would otherwise be missed by sampling and real-time oscilloscopes. The effective sampling rate

of TiSER is much higher than any other commercial electronic ADC available commercially [89].
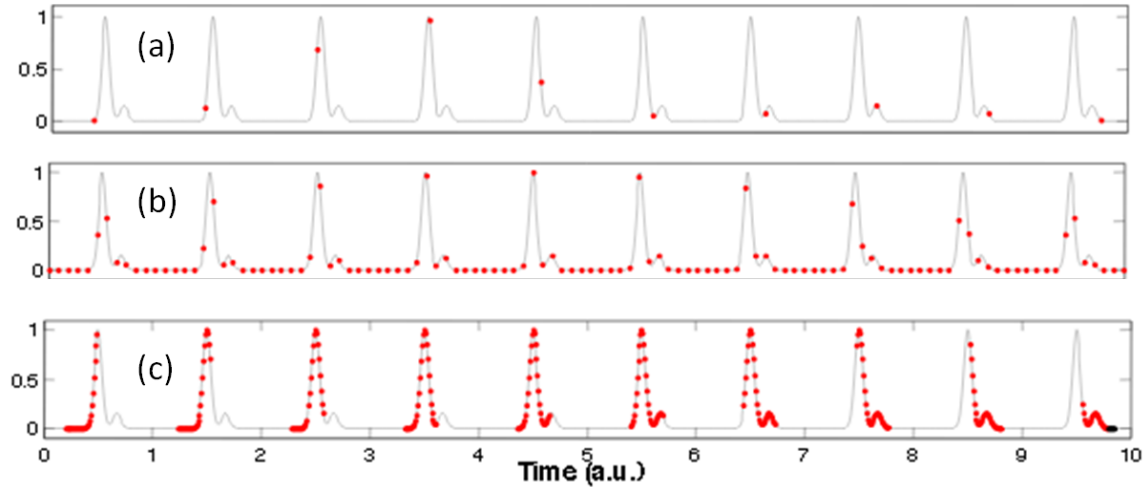
Figure 6.2. Different sampling techniques are shown. (a) An equivalent-time oscilloscope samples signals at very slow rates and can reproduce signals only of repetitive nature. (b) A real-time digitizer samples signals continuously but has limited bandwidth. (c) TiSER can capture very high bandwidth signal segments in real-time and quickly reproduce them on equivalent time scales [89].

6.1.2 Jitter Noise in TiSER

The amount of jitter noise during digitization is reduced due to time-stretching the signal making the measurement more accurate. With high speed signals, jitter from electronic ADCs becomes a major factor that could affect the measurement. A small amount of jitter from the ADC could result in a large voltage error depending on how rapidly the signal is changing. As shown in

Figure 6.3, an ADC with sampling jitter of $\tau_{j,clock}$ could give a large range of voltages depending on where the signal is sampled which could result in a large voltage error.
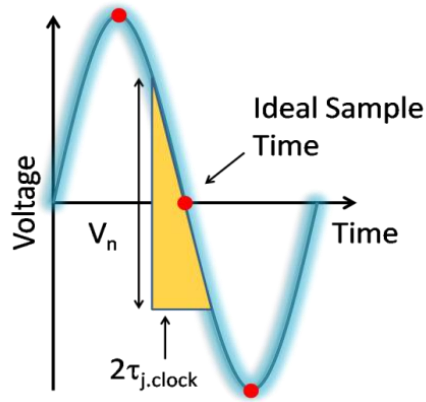
Figure 6.3. Small amount of jitter in a fast signal can result in large voltage errors [12].

If the signal were stretched in time and sampled with the same ADC, the rate at which the signal changes is reduced as shown in Figure 6.4. By reducing the slope at which the voltage changes, the overall voltage error due to jitter will be less. At this stage, we've only reduced the amplitude jitter, but the amount of sampling jitter from the ADC is still the same.
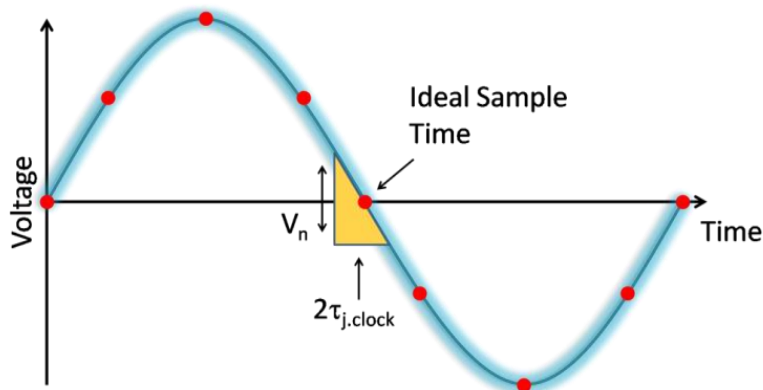
Figure 6.4. Sampling stretched fast signal reduces amplitude jitter [12].

When we recompress the stretched signal to the original time scale, the amount of sampling jitter from the ADC is reduced by the stretch factor. Also because previously we showed how the

74

amplitude error was reduced after stretching, then this final waveform has reduced both amplitude and sampling jitter errors.
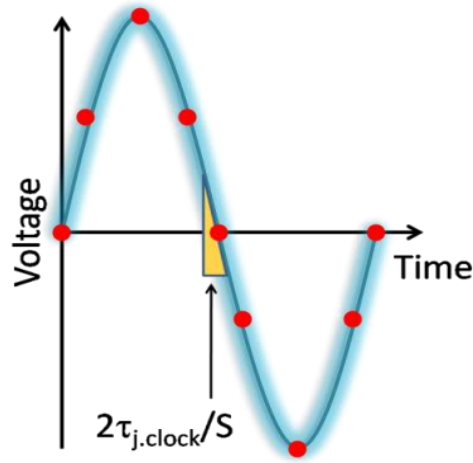
Figure 6.5. By recompressing the signal to the original timescale, the sampling jitter is reduced [12].

The total jitter in TiSER is based on the record time and can be defined by either short or long durations. For short, single-shot measurements using one pulse which is defined as intra-pulse jitter, then the jitter contribution is from the electronic ADC. The total jitter for intra-pulse jitter is given by

$$\tau_{j,TiSER} = \frac{\tau_{j,ADC}}{S} \qquad (6.1)$$

For long measurements involving multiple pulses, this is defined as inter-pulse jitter. The main jitter contribution is from the jitter of the mode-locked laser. When we take this into account, then the total jitter for inter-pulse jitter is expressed as

$$\tau_{j,TiSER} = \sqrt{\tau_{j,laser}^2 + \left(\frac{\tau_{j,ADC}}{S}\right)^2}. \qquad (6.2)$$

Using TiSER's mode locked laser and FPGA ADC jitter values, the mode locked laser has a jitter of 150 fs rms and FPGA ADC has 0.4 ps rms jitter. For short measurements using one pulse, the intra-pulse jitter is 8 fs rms. For long measurements, the overall estimated inter-pulse jitter from

75

TiSER is about 150 fs rms. Therefore, TiSER has very low jitter which is important when measuring signal integrity parameters such as jitter. These values are very short compared to the jitter we are trying to measure which may be on the order of picoseconds. This allows us to use TiSER to measure the jitter of other signals since our jitter is lower than conventional standards and other hardware. Time-stretch is able to reduce the amount of jitter noise contributed by electronic ADCs in the measurement.

6.2   Introduction to Signal Integrity

In high speed measurements, signal integrity is a significant issue and is posing increasing challenges to design engineers. Signal integrity is a set of measurements that determines the timing and quality of an electrical signal [90]. More importantly, does the signal reach its destination when it is supposed to and is it in good condition? In the past, digital transmission speeds were on the order of megahertz and there were fewer issues at such low speeds. With accelerating data rates, higher frequencies are used which push the limits of electronics and increase design complexity. Faster switches and detectors are required to detect the signal received. As the frequency increases and thus the required bandwidth, a variety of variables such as transmission-line effects, impedance mismatches, ringing, and crosstalk can hamper the performance and thus the signal integrity of a high speed link. As technology continues to evolve, it makes it more difficult for system developers to design completed, unimpaired signals in digital systems. Ultimately, systems are judged on their ability to pass bits faithfully and without error [91]. In this section, we concentrate on measuring signal characteristics that could affect signal integrity namely jitter, rise time, fall time, and bit error rate since those are of interest to high speed communications.

76

6.3 Signal Integrity Measurements from Eye Diagram

The eye diagram is a very successful way of quickly and intuitively assessing the quality of signals in high speed transmissions. The eye diagram is generated by superimposing every possible combination of 1's and 0's from segments of long data streams [92]. The edges of the bit sequences are timed according to a master clock and after a period of time, the resulting image would appear like an eye. Ideally, the eye diagram would appear like a rectangular box. In reality, communication systems are imperfect and thus the pattern appears eye shaped. The eye diagram shows parametric information about the signal such as any impairment in the communication system that would distort the signal and cause the recovery circuit to read the wrong bit value. Common measurements using of characterizing an eye diagram is to measure the rise times, fall times, jitter, overshoots present, bit error rate, and any other numerical descriptions of eye behavior [91].

By taking advantage of TiSER's real-time burst sampling, we can capture long segments of data that would otherwise not be able to be captured by sampling oscilloscopes or real-time oscilloscopes. This gives us more information about the signal at that instance than over several repetitions which would not give us a real-time advantage. Moreover, these longer segments can help us gain important insight into a signal and capture transients and overshoots that may occur. Below in Figure 6.6, we can see how the real-time burst sampling can be used to generate eye diagrams by superimposing the captured data streams on top of each other. We can also see that by capturing long segments, transient effects can be observed that would otherwise be missed by the other oscilloscopes. TiSER also allows us to generate eye diagrams in a fraction of the time that it would take a regular sampling oscilloscope.
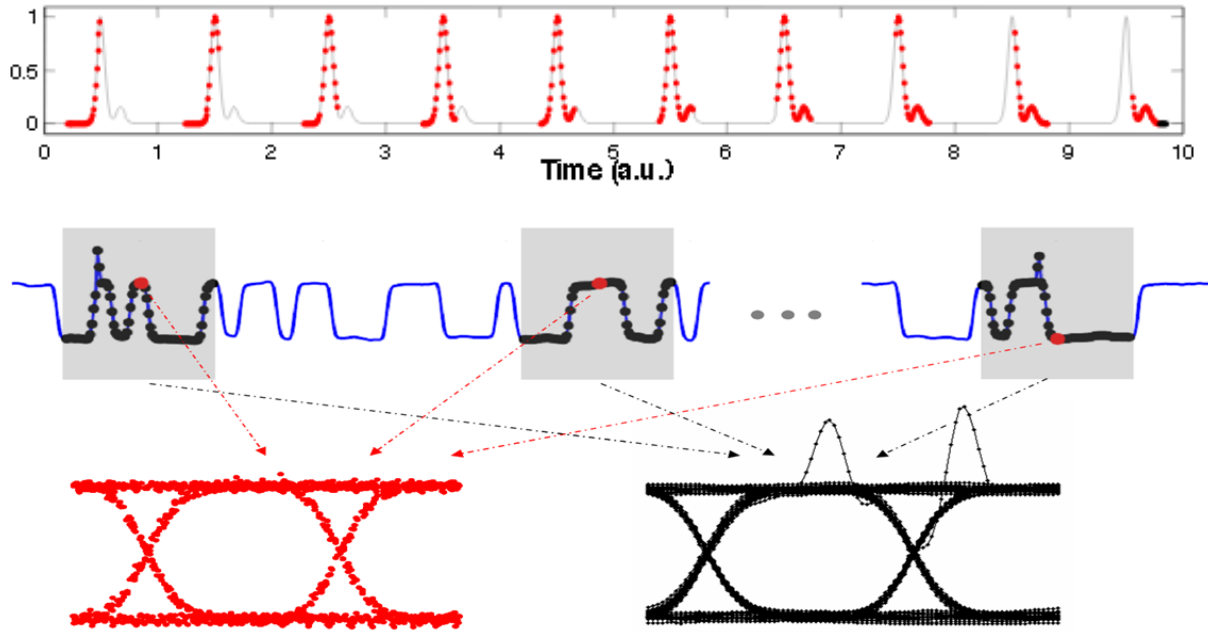
Figure 6.6. Real-time burst sampling modality using TiSER allows for rapid generation of eye

diagrams for signal integrity analysis [89].

Using the eye diagram generated by TiSER, the performance parameters that we are interested in measuring are bit error rate, rise times, fall times, and jitter. All these values can be estimated by performing statistical analysis on various parts of the eye diagram as shown in Figure 6.7. The colored markers indicate the location of where a statistical measurement will be taken. Each measurement is described in detail in the following sections.
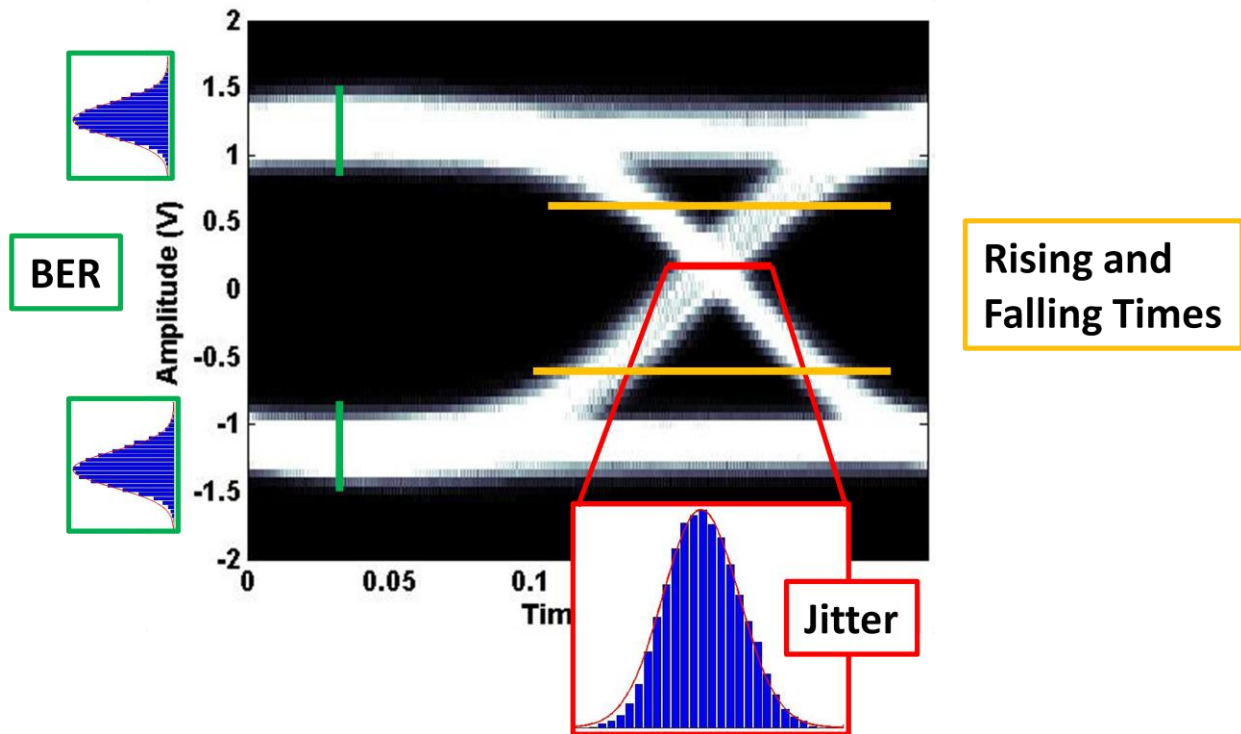
Figure 6.7. Eye diagram with areas of statistical measurements for bit error rate, jitter, and rise and fall times.

6.4 Bit Error Rate Measurement

The bit error rate (BER) is the single most important quantifier of the quality of transmission. This value estimates the probability of how many erroneous bits will be generated over a total number of bits transmitted. In modern high speed communication links, the typical number of errors allowed is one in a billion bits. There are two methods used to measure the bit error rate. The first is to directly measure the BER using a bit error rate tester (BERT) which is the most accurate form of measurement since it will compare bits transmitted and received and count the errors incurred from the system. The BERT sends a known sequence of bits through a channel, detects the output, and checks the output signal to the input signal for errors. The BERT can take

on the order of minutes to many hours to measure the BER depending on the data rate and what BER value is desired. However when there are multiple channels needing to be measured, this method becomes impractical due to the amount of time required to do a measurement. For example, when requiring a BER of 1×10^{-15} a minimum measurement time of 27 hours is required at 10 Gb/s data rate for just a single channel to get to a 95% confidence level. When using this method, the BER is given by the following equation [23], [93]:

$$\text{Bit Error Rate, BER} = \frac{\text{Number of Erroneous Bits}}{\text{Total Number of Bits Transmitted}} \qquad (6.3)$$

The second method is using the quality factor, or "Q factor", to estimate the BER [93]. The Q factor involves generating an eye diagram and estimating the BER from the eye opening by Gaussian fit approximations which is much faster than using a BERT for measuring low BER values of 10^{-12} to 10^{-15}. This method is uses the signal-to-noise ratio (SNR) in a digital signal and assumes normal noise distribution to estimate the BER. In a digital receiver, a decision circuit decides whether an incoming binary signal is at a logical 0 or 1 level by sampling the received signal and comparing the sample value to a threshold value. In a noise free system, the received signal would have only two states. However due to additive noise and nonlinear distortions caused by the transmission medium or equipment, the received signal levels can vary. This means the sampled receive signal must be regarded as a random variable with probability distributions $p_x(x|0)$ and $p_x(x|1)$ for the probability of detecting a 0 or 1 respectively. It is in the overlapping regions where the BER is determined [93].
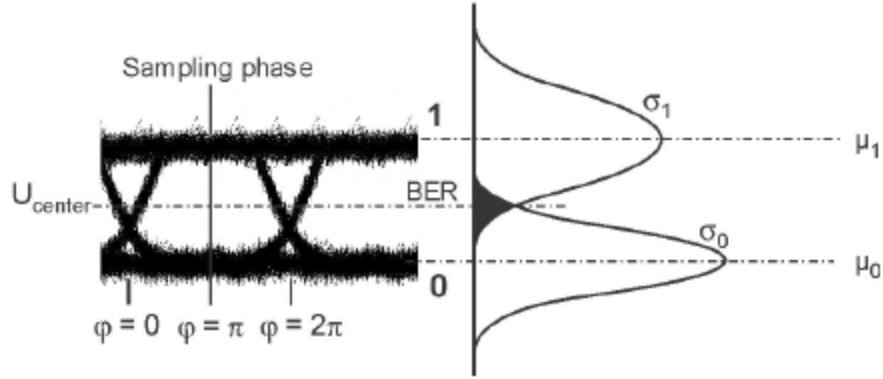
Figure 6.8. The probability distribution functions used to estimate BER from an eye diagram.

The overlap region determines the BER [94].

Assuming normal noise distribution and our decision threshold is set at optimum location for minimum BER, each of these two distributions have a mean value μ and variance σ. Even with optimal threshold settings, there is a probability $P(1|0)$ for detecting a 1, although a 0 was transmitted and the same for the probability $P(0|1)$ for detecting 0 although a 1 was transmitted. The total BER can be expressed as [93]:

$$BER = P(0|1) \cdot P(0) + P(1|0) \cdot P(1) \tag{6.4}$$

where

$$P(0|1) = \int_{-\infty}^{V_{th}} p_x(x|1) \, dx \tag{6.5}$$

and

$$P(1|0) = \int_{V_{th}}^{\infty} p_x(x|0) \, dx . \tag{6.6}$$

From these probabilities, we can determine the mean levels for '1' and '0' given by μ_1 and μ_0 respectively and their variances σ_1 and σ_0 respectively by looking at the distribution at the

sampling point. If we take the mean value and variances, we can determine the Q value defined by [23]

$$Q = \frac{\mu_1 - \mu_0}{\sigma_1 + \sigma_0}$$

(6.7)

and the BER can be estimated using the following equation [23]

$$BER = \frac{1}{2} erfc\left(\frac{Q}{\sqrt{2}}\right)$$

(6.8)

From equation 6.8 we observe that as the SNR degrades, resulting in a lower Q value, then the BER will be a higher value and is thus worse in performance. As the SNR increases giving a higher Q, then the BER will be lower resulting in better performance. As the data rate increases and assuming constant optical power in the system, the BER will worsen since the signal to noise ratio decreases with faster data rate [94]. With faster data rates, we require increased bandwidth to measure the signal and this adds more noise. To get the same BER value, we would need to increase the transmitter power to improve SNR. Visually in the eye diagram, we would expect the eye opening to shrink and thus the BER will get worse with decreasing SNR. As the SNR is decreasing, then the noise grows which will make the eye narrow. This will increase the likelihood of getting erroneous bits which results in more bit errors. If we were to draw an eye mask over the opening of the eye, the edge of the mask is where we can move our decision circuit sampling point to obtain a particular BER. The size of the mask would correspond to a particular BER. As we move the sample point closer to the edge of the eye, the probability of errors would increase thus resulting in a worse BER.

Time is not a factor when performing a Q factor measurement because the timing circuits used for eye diagram generation have very little jitter. The jitter in these circuits must follow conventional standards and thus the jitter will be very low as the signal is usually resampled by a

clock and data recovery circuit (CDR). The clock used to sample the wave form is generated from the CDR, which will have little jitter. Because of this, we are always sampling in the middle of the eye. The sides of the eye will not shrink into the eye as much due to the little jitter in the clock, however the amplitude can vary since it is affected by SNR. The SNR is affected by the data rate and distance transmitted. As noise increases, then the amplitude of the eye will shrink thus the eye diagram will shrink from the top and bottom. The SNR is a better indicator of the bit error rate which is why we perform amplitude measurement rather than jitter to estimate BER. Jitter can be a factor in BER estimation only if there is a lot of jitter in the system.

6.5   Jitter Measurement

Jitter is a major parameter when measuring signal integrity and is defined as the deviation of the significant instances of a signal from their ideal location in time [95]-[97]. Essentially it describes how early or late a signal transitions with reference to when it should transition. As data transfer rates continually increase, it becomes more difficult to accurately decipher the 1's and 0's, and with an ever shrinking time window to determine the level, a small amount of jitter could result in a signal being on the "wrong" side of a transition threshold [95]-[97]. The more important jitter we are concerned with measuring is timing jitter since this affects the time when a transition occurs. Having a significant amount of jitter can severely limit the transmitted data rate, reduce the signal to noise ratio, and can reduce the effective resolution of ADCs and their effective number of bits. By measuring and characterizing the jitter encountered in a system, actions to correct or compensate for it can result in a more accurate bit stream leading to lower BER and faster transmission speeds.

To estimate the jitter in the system, a histogram of the eye diagram is generated. In this code, the jitter is assumed to be due to random noise and thus follows a Gaussian distribution. From the eye diagram histogram, a one pixel wide sample of the crossing point of the eye diagram at the sampling threshold is plotted. Afterwards, a Gaussian curve fit is performed on the histogram data, and the resultant jitter will be approximately twice the variance. This measurement can also be done to determine the jitter in a rising edge or falling edge as well as shown in Figure 6.9.
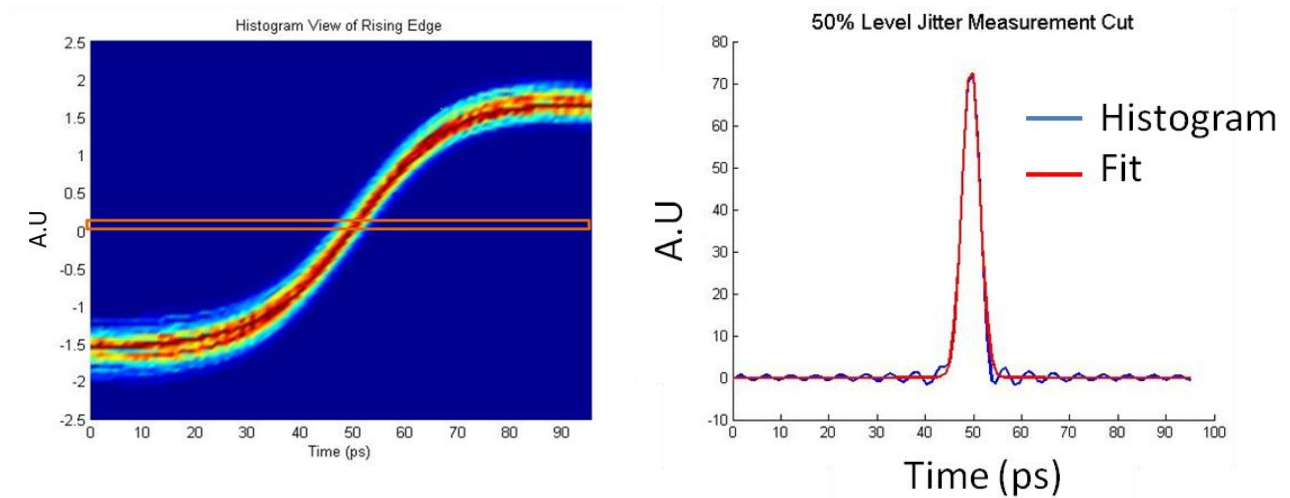
Figure 6.9. Histogram of a rising edge and the sample taken from the center to determine the jitter.

6.6 Rise and Fall Time Measurement

The rise and fall times describe the transition time of a signal from a low value to high value or high value to low value respectively. In high speed optical electronics, the rise and fall times measure the ability of a circuit to respond to fast input signals. The rise and fall times are defined as the time for the response to rise from x% to y% of its final value [98]. In analog signals, typically it is the time the signal takes to rise from 10% to 90%.

Using TiSER's burst sampling, a rising and falling edge can be captured with higher temporal resolution in a single burst. Figure 6.10 shows the performance difference between a real-time oscilloscope and TiSER in a single burst. By capturing a segment, we can get better resolution on the transition edges. Using a 50 GSamples/s Tektronix oscilloscope, we can get at best 2-4 points along the edge of a 12.5 Gbps signal. In comparison using TiSER, we can get approximately 20 points on the edge. If we were to take several of these rising edge measurements, we can get a more accurate measurement of the rising and falling edges. We can also measure any transient effects as the signal rises and falls.
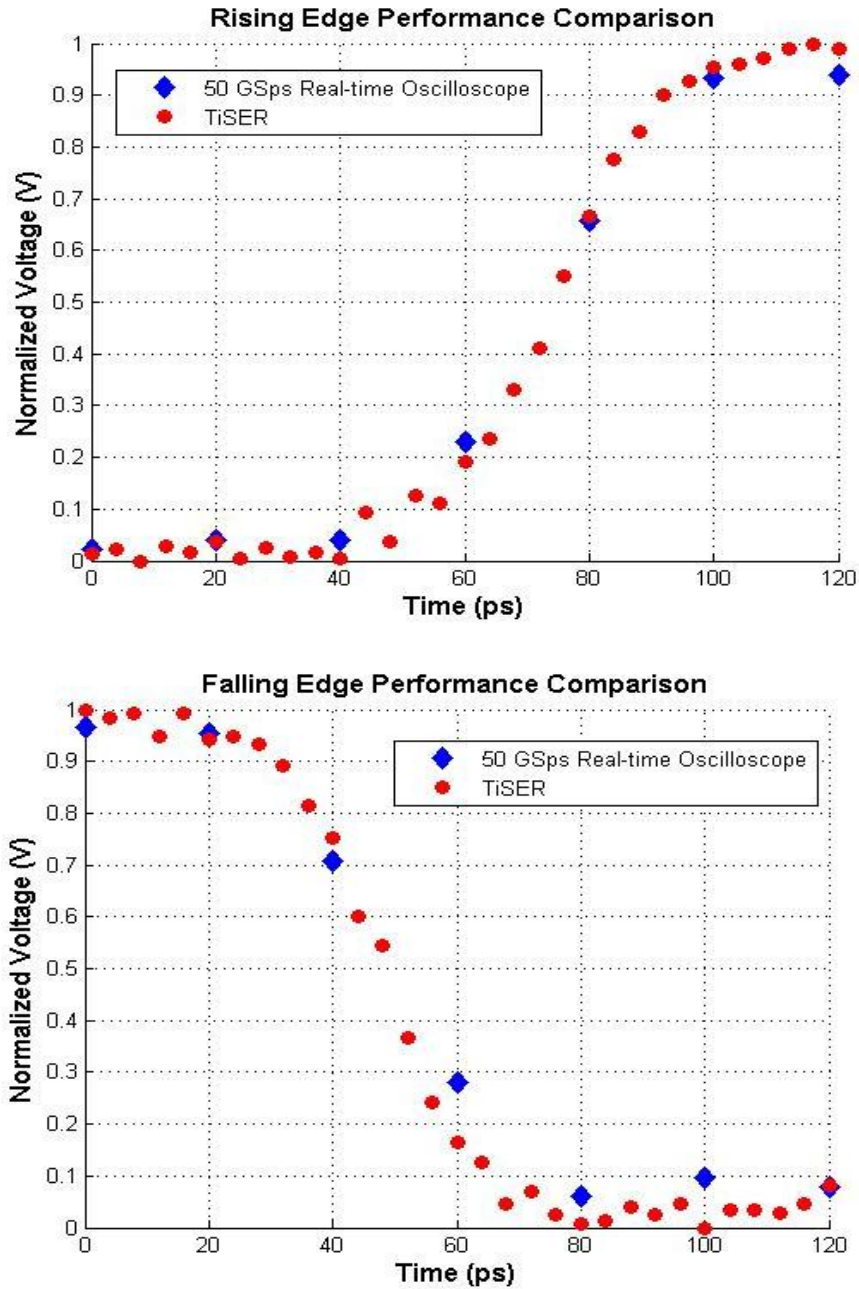
Figure 6.10. Comparison of the temporal resolution for TiSER with stretch factor 50 and 50

GSample/s real-time digitizer capture of the rising (top) and falling (bottom) edges of a 12.5

Gbps data stream in a single burst. TiSER can capture about 20 data points whereas a real-time

digitizer can only get 2-4 along the edge.

The rise and fall times can be calculated from the eye diagram. This is determined by taking a histogram of the low and high values in a rising edge or falling edge. An example of how the rise time is calculated is shown in Figures 6.11, 6.12, and 6.13. Starting from an eye diagram as shown in Figure 6.11, the points for the rising edge and the falling edges can be separated. Using just the rising edge points as shown in Figure 6.12, the '0' and '1' levels are determined by plotting a histogram of the low and high sample points (indicated in green) and performing a Gaussian fit on the data. The mean values in the histogram are approximated to be the low and high levels. Once the '0' and '1' levels are determined, then the rise time can be measured by determining the time it takes the signal to rise or fall from 10% to 90%. For just a rising edge or falling edge, a histogram of the end points at both the low and high ends are used to determine the level of the '0' and '1' levels. From there the rise and fall times can be determined at the intersection of the 10% and 90% levels and taking the time difference between the purple lines as shown in Figure 6.13. Similarly, the falling edge can be determined using the same method as shown in Figure 6.14.
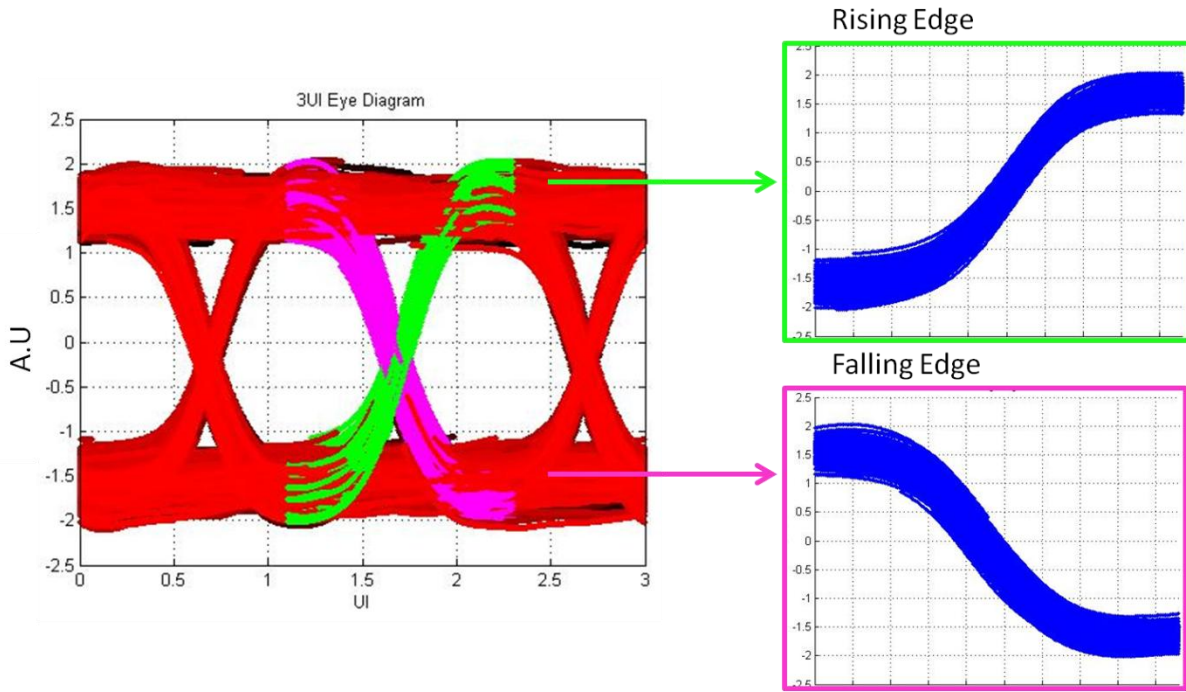
Figure 6.11. Starting from an eye diagram, the rising and falling edges can be separated.
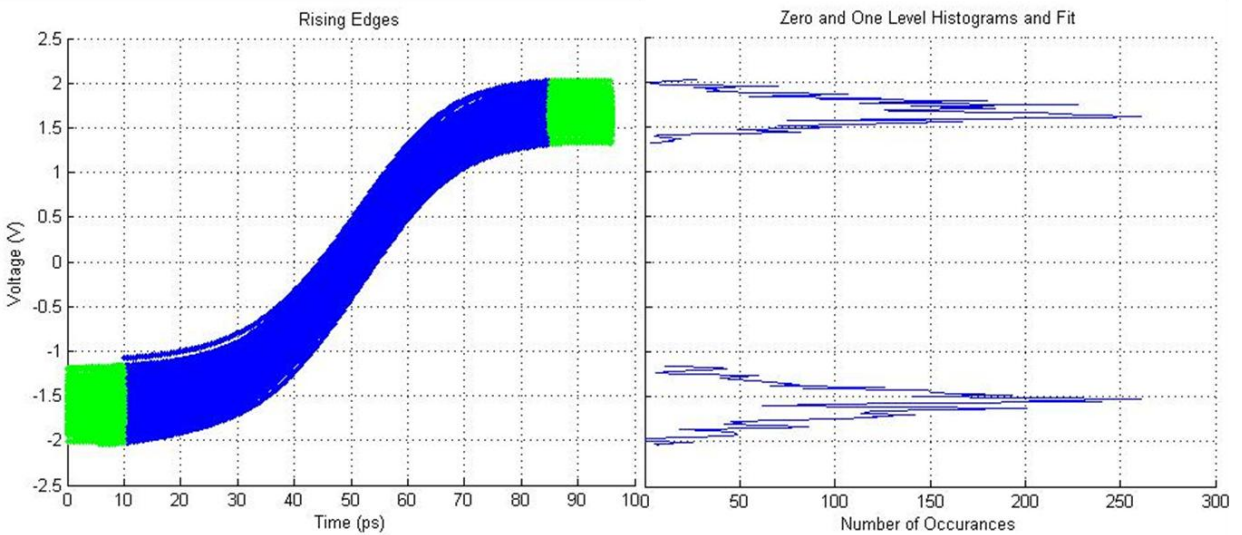
Figure 6.12. The determination of the '0' and '1' levels.
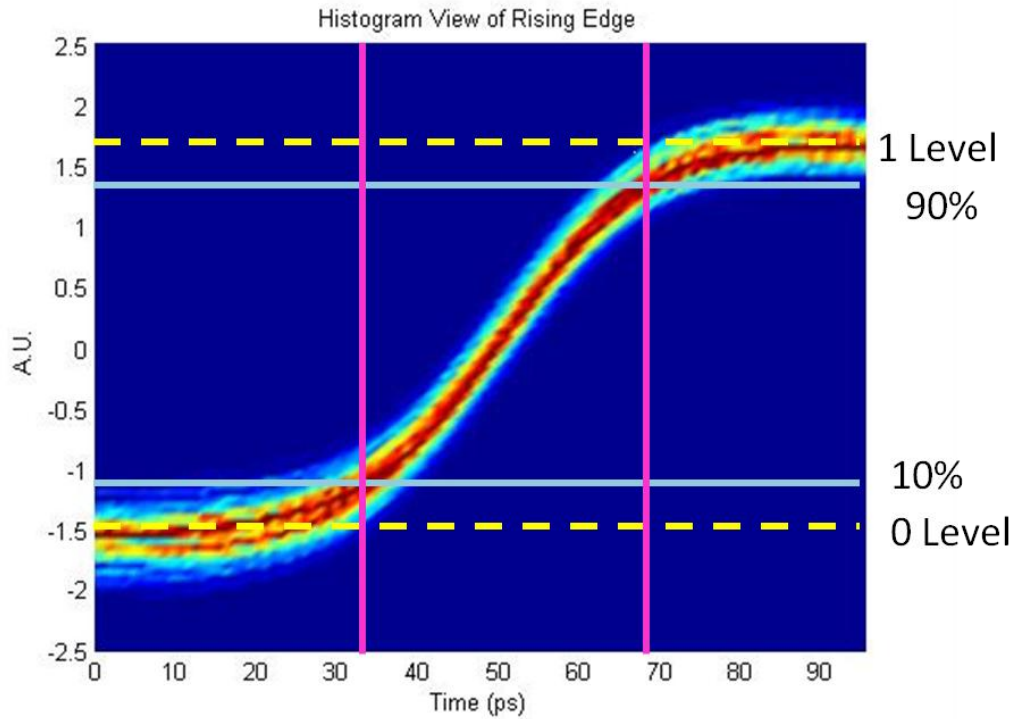
Figure 6.13. The rise time for a rising edge is the time between the purple lines.
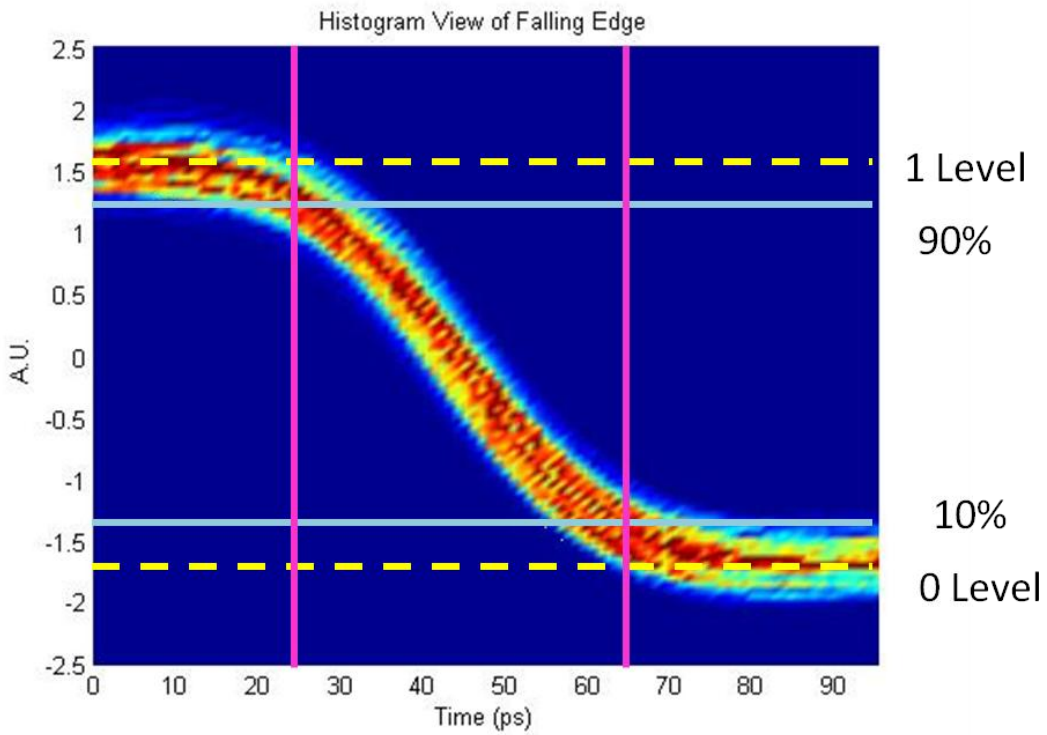
Figure 6.14. The fall time for a falling edge is the time between the purple lines.

6.7   Verification of TiSER Measurements

TiSER is able to generate eye diagrams, and the methods explained in the earlier sections are used to perform signal integrity measurements. However, verification of these values needs to be performed to ensure that it matches with values from standard industry equipment. To verify the performance of TiSER, results were compared to a BERT for bit error rate and a Tektronix oscilloscope for rising and falling times and jitter measurements. A method is provided to calibrate TiSER to make sure it is working properly before performing a measurement.

6.7.1 Jitter, Rise and Fall Time Verification

To verify the results for jitter, rise and fall times, the eye diagrams generated by TiSER is compared to a Tektronix DPO71604C oscillscope. For this experiment, an Anritsu MP1763C pulse pattern generator was used to generate a 10 GSample/s signal. This signal was then inputted to TiSER and the real-time oscilloscope where the eyes are generated as shown in Figures 6.16 to 6.19. The same Matlab code is used to analyze the data, and the results are listed in Table 6-1 and both appear to be in agreement.

Table 6-1. TiSER and Tektronix oscilloscope measurement comparisons.

Parameter	Anritsu	TiSER	Tektronix
Jitter (ps)	< 4	3.6	3.5
Rise Time (ps)	< 40	39.3	42
Fall Time (ps)	< 40	39.5	42.4
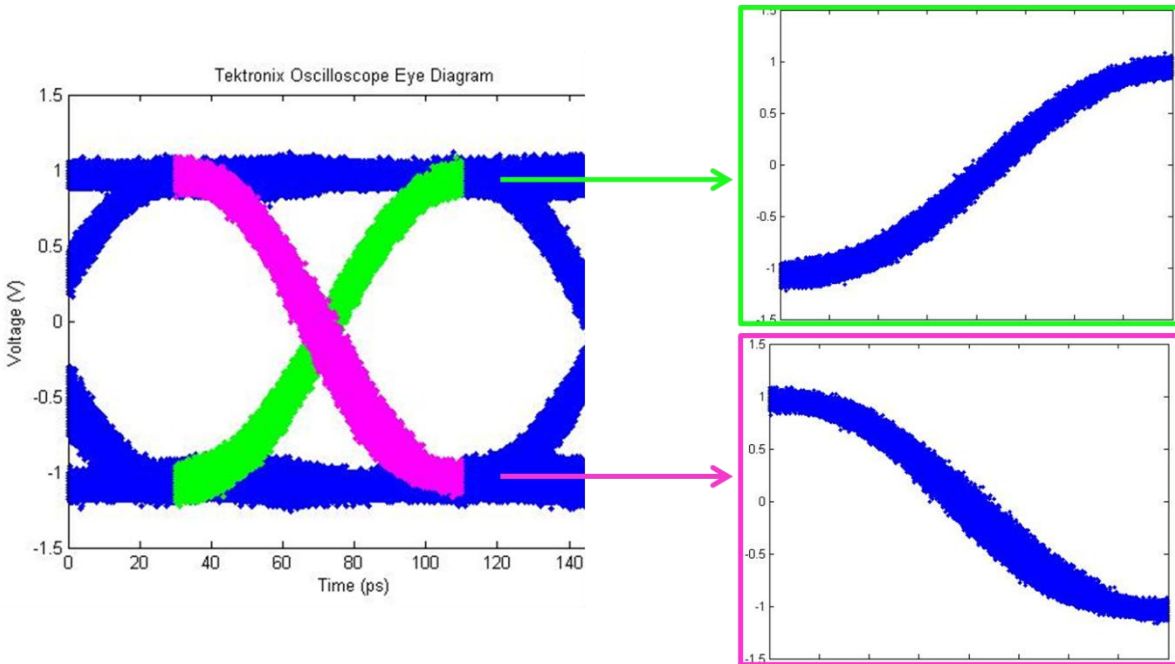
Figure 6.15. Eye diagram generated by using data from Tektronix real-time oscilloscope and

how the rising and falling edges are separated.
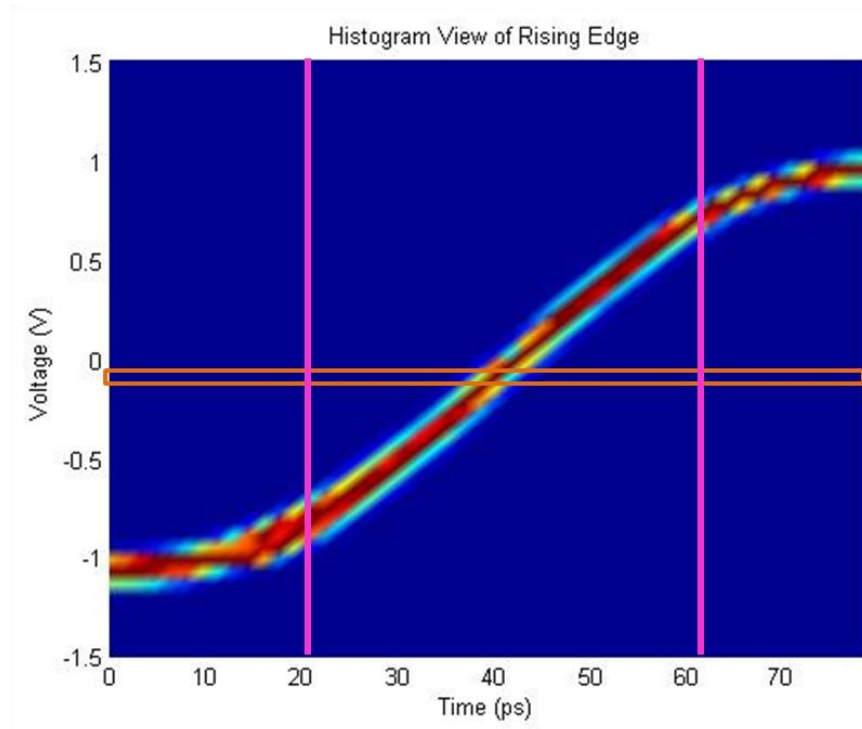
Figure 6.16. Histogram of the rising edge of a PRBS signal using a Tektronix oscilloscope.
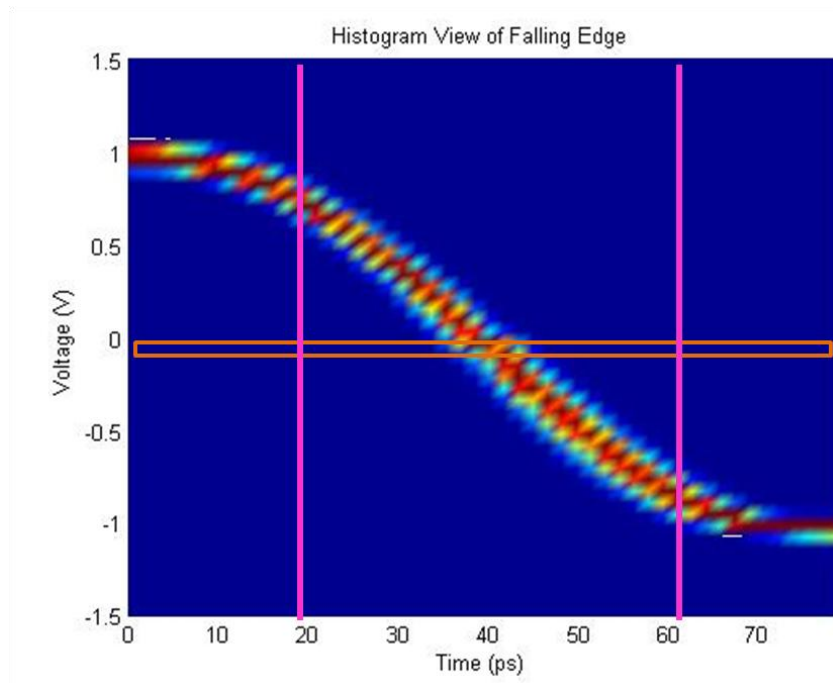
Figure 6.17. Histogram of the falling edge of a PRBS signal using a Tektronix oscilloscope.
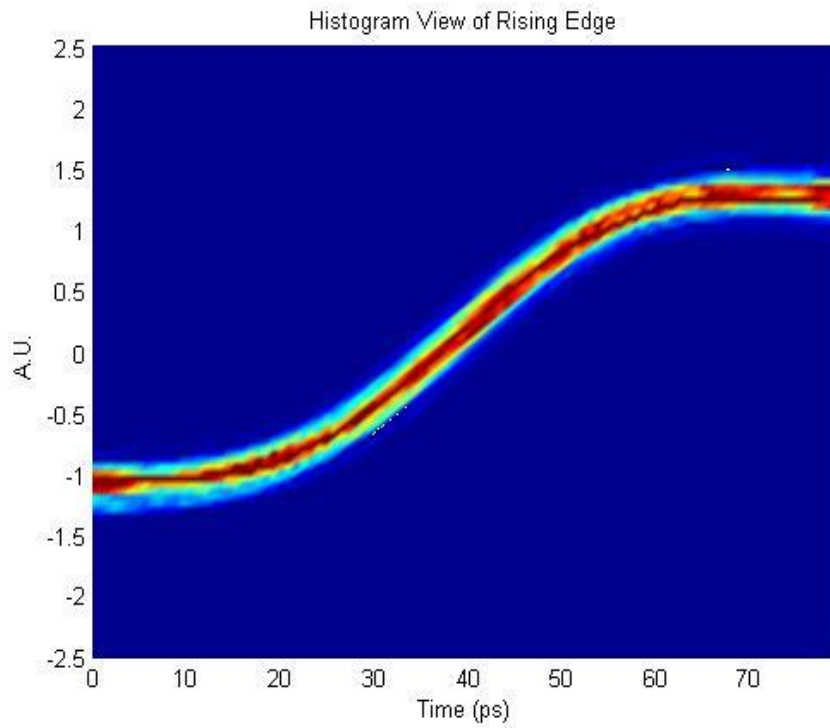
Figure 6.18. Histogram of the rising edge of a PRBS signal using TiSER.
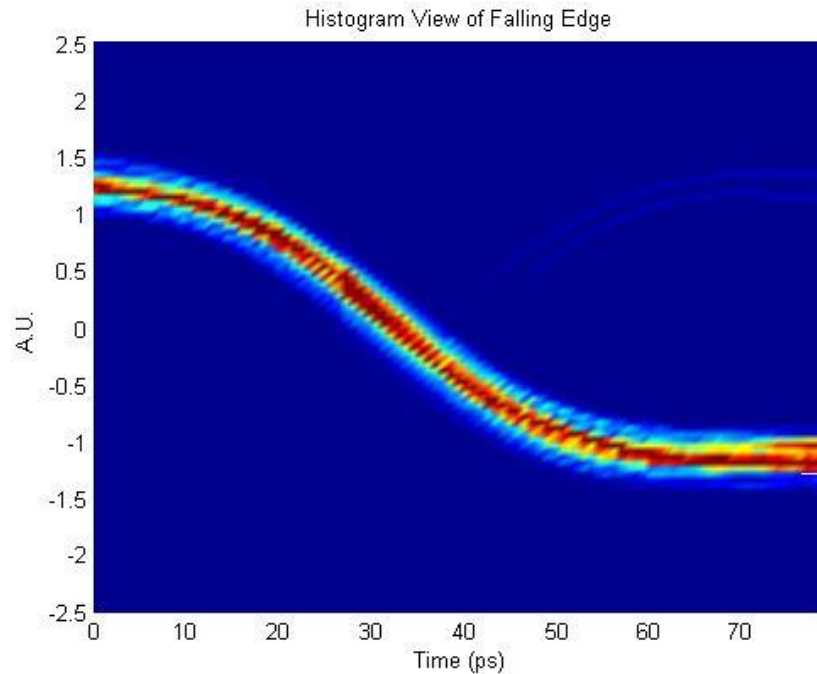
Figure 6.19. Histogram of the falling edge of a PRBS signal using TiSER.

6.7.2 Comparing BERT to TiSER

A Centellax TG1B1-A Bit Error Rate Tester was used for testing for BER. The BERT's internal 10 GSample/s pseudo-random binary sequence (PRBS) generator and a receiver unit were used for this test. A block diagram of the experimental set up is shown in Figure 6.20 for using the BERT. Noise was added to the PRBS signal and the combined signal was sent to the receiver unit where the bits were compared to the transmitted signal. The bit error rate is then determined by the BERT. As the amount of noise is added to the signal, the number of errors was observed to increase thus making the BER value worse. The amount of noise to obtain BER values within the range of 10^{-3} to 10^{-12} was determined. For BER values smaller than 10^{-12}, this was difficult to estimate for both TiSER and the BERT due to the short measurement times. For small BER values using TiSER, the difference between 10^{-15} and 10^{-20} were about the same, and TiSER has

difficulty measuring small BER consistently. For larger BER values where an error would occur

sooner or the SNR has been degraded sufficiently, the output values from TiSER matched within

an order of magnitude of the BERT.

Figure 6.20. The experimental set up used for measuring BER with a BERT and the addition of a

noise generator in the signal path.
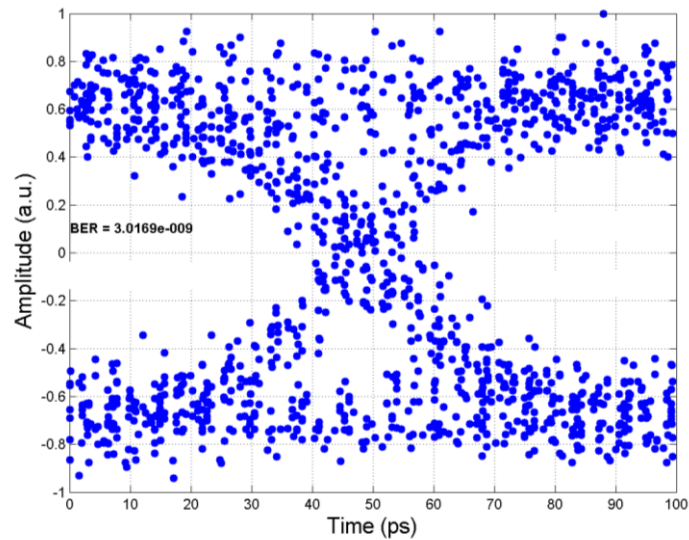
Figure 6.21. To measure the BER, noise was combined with the signal until a certain BER value

was obtained (top). The addition of noise degraded the eye (middle) and we can estimate the

BER using TiSER (bottom).

95

6.8   Advantages of using TiSER

TiSER can be used for signal integrity measurements and has been verified by comparing the performance to commercial measurement equipment. TiSER provides several advantages over similar instruments. The high effective sampling rate and temporal resolution allows TiSER to generate eye diagrams much quicker and with these tools, TiSER can be used to quickly analyze an eye diagram and measure the rise and fall times, jitter, and bit error rate. The high temporal resolution gives TiSER the capability to capture rare events and transients and time traces of data bits which are impossible to capture with a conventional sampling oscilloscope. For electronic ADCs that can achieve comparable sampling speeds as TiSER, TiSER has a much larger input bandwidth and requires far less power due to its use of photonics.

Chapter 7

Integration of TiSER into Test-bed for Optical Aggregate Networks

In the previous chapter, analysis tools were developed to evaluate signal integrity parameters and estimate the bit error rate from eye diagrams generated by TiSER offline. A time-stretch accelerated processor [99] was achieved which allowed for the generation of eye diagrams in real-time using TiSER. This new capability allowed for rapid eye diagram generation and analysis which is beneficial for monitoring next generation optical networks. This new instrument, known as real-time TiSER, was integrated into an optical test-bed studying aggregate optical networks at the University of Arizona where it was used as an optical performance monitor. In this multi-university collaborative effort consisting of the University of Arizona, University of California Los Angeles, Columbia University, University of Southern California, and Cornell University, we set out to build and demonstrate an aggregate optical network. TiSER would serve as an optical performance monitor and provide real-time feedback to a software defined network (SDN) control plane which is used to optimize optical network performance. Using real-time TiSER, amplified stimulated emission and self phase modulation effects were

97

observed. Moreover, real-time TiSER was used to demonstrate for the first time real-time, in-service monitoring of a commercial platform [99].

7.1   Introduction to Center for Integrated Access Networks

The collaboration effort was funded by the National Science Foundation Center for Integrated Access Networks (CIAN) Engineering Research Center (ERC). CIAN is a multi-institutional research effort consisting of the University of Arizona (Lead), University of California at Los Angeles, University of California at San Diego, University of California at Berkeley, University of Southern California, Columbia University, Norfolk State University, and Tuskegee University. The vision of CIAN is to create transformative technologies for optical access networks where virtually any application requiring any resource can be seamlessly and efficiently aggregated and interfaced with existing and future core networks in a cost-effective manner. Analogous to the evolution over decades of today's computer laptop using massive integration of discrete electronic components, the CIAN vision would lead to the creation of the PC equivalent of the optical access network by employing optoelectronic integration to enable affordable and flexible access to any type of service, including delivery of data rates approaching 10 Gigabits/sec to a broad population base anywhere and at any time [100].

7.2   Optical Performance Monitoring in Next Generation Networks

One of the main issues in modern communication systems is the time to repair when impairments are present. This would result in shutting down portions of the optical network to debug, repair, and then verify that the fix worked which could take hours to days. In the event of

a disaster, this could mean service could be down for extended periods of time while the optical links are rerouted [93]. Customers require a certain quality of service and performance monitors are needed to ensure they receive excellent service.

Next generation fiber optic communication networks need to be "smart", robust, reconfigurable, flexible, and secure [93], [101]. This means that future smart networks need to be able to measure its physical state and the quality of propagating signals and take action if any degradation occurs. These networks will need to automatically diagnose and repair failures and take actions before data loss and failures take place. In the event of a failure, the network is able to allocate resources by changing the wavelength or amount of power transmitted, channel bandwidths, and data modulation formats. If impairments are affecting a certain link, the network can immediately change the routing tables and redirect traffic based on physical layer conditions. In terms of security, the network should be able to detect any accidental and malicious security risks [93], [101].

With faster transmission rates and more advanced modulation formats, impairments can bring down entire networks and the window for error is getting smaller. Optical performance monitoring is able to help widen and maintain that window for channel operations. Faster data rates and multiple data formats can lead to systems having multiple impairments that affect over performance. These impairments must be isolated, localized, and compensated which requires rapid monitoring and dynamic feedback control. In order to enable robust and cost-effective "self managed" operations, next generation optical networks need to be able to detect and compensate for these impairments. An optical performance monitor (OPM) that can perform rapid measurements is needed for next generation intelligent networks. Real-time TiSER is a solution

99

that can perform rapid signal quality measurements by providing BER estimations and generate eye diagrams in real-time for further analysis.

7.3   Insertion of TiSER into Test-bed for Optical Aggregate Networks

In this collaborative effort, different technology insertions from the University of Arizona, University of California at Los Angeles (UCLA), Columbia University, University of Southern California (USC), and Cornell University were incorporated into the Test-bed for Optical Aggregate Networks (TOAN). This test-bed was specially designed to study and demonstrate the ability of an optical network to quickly adapt to impairments. As Internet traffic grows, more than half of traffic will be over metropolitan networks rather than long-haul backbone due to streaming services. New mesh grid architectures are being designed and with the invention of optical space switches and reconfigurable optical add-drop multiplexer (ROADM), communication networks have the ability to be increasingly flexible.

The test-bed consists of a four nodes topology designed to simulate a metropolitan network as shown in Figure 7.1. A major challenge in enabling network agility is that transmission impairments and dynamics result in instability and uncertainty, making dynamic networks harder to predict and control. To study the effects of transients, the nodes are connected using distance emulators. The distance emulators enable the creation of transmission impairments that accumulate over multiple hops, while only using a single span of networking equipment. These impairments such as amplified stimulated emission (ASE) and self phase modulation (SPM) could be injected into the network.

The architecture of each node, called the CIAN Box, consists of three different planes. The first plane is the switching plane in which a Calient 260x260 fiber switch was utilized to

build a colorless, contentionless, and directionless ROADM architecture. This is the most flexible way to allow the network to switch wavelengths quickly. However, the CDC ROADM architecture is not enough to enable dynamic reconfiguration capabilities, and the OPM plane is used to monitor the quality of the signals.

To monitor the optical performance of the network, two complementary methods were employed. The first method was a real-time optical signal to noise ratio (OSNR) monitor using delay line interferometry developed by USC. This monitor performed measurements on the OSNR which gave coarse measurements of the optical signal, but nothing about the electric signal. The second method was using TiSER developed by UCLA. TiSER is able to perform finer measurements and provide more detailed information such as BER, jitter, and rise and fall times about the electric signal. TiSER was able to send the BER via XMPP to a SDN controller. This SDN controller is able to make decisions and make any necessary adjustments to the network based on the information provided.
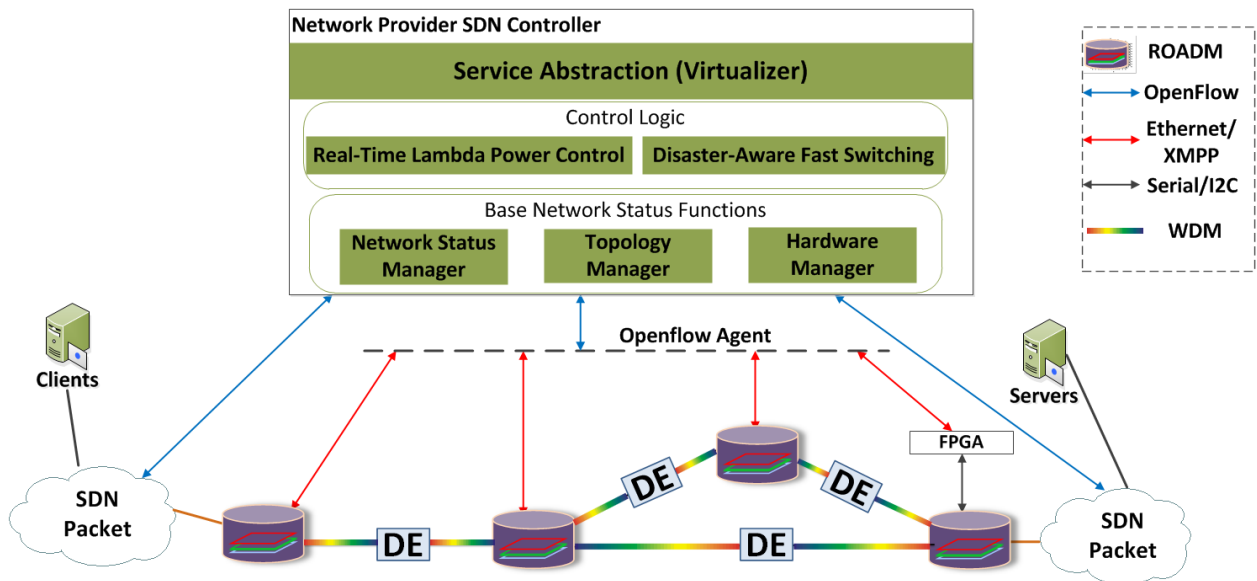
Figure 7.1. The SDN plane that receives feedback from the OPM layers for dynamic network control.
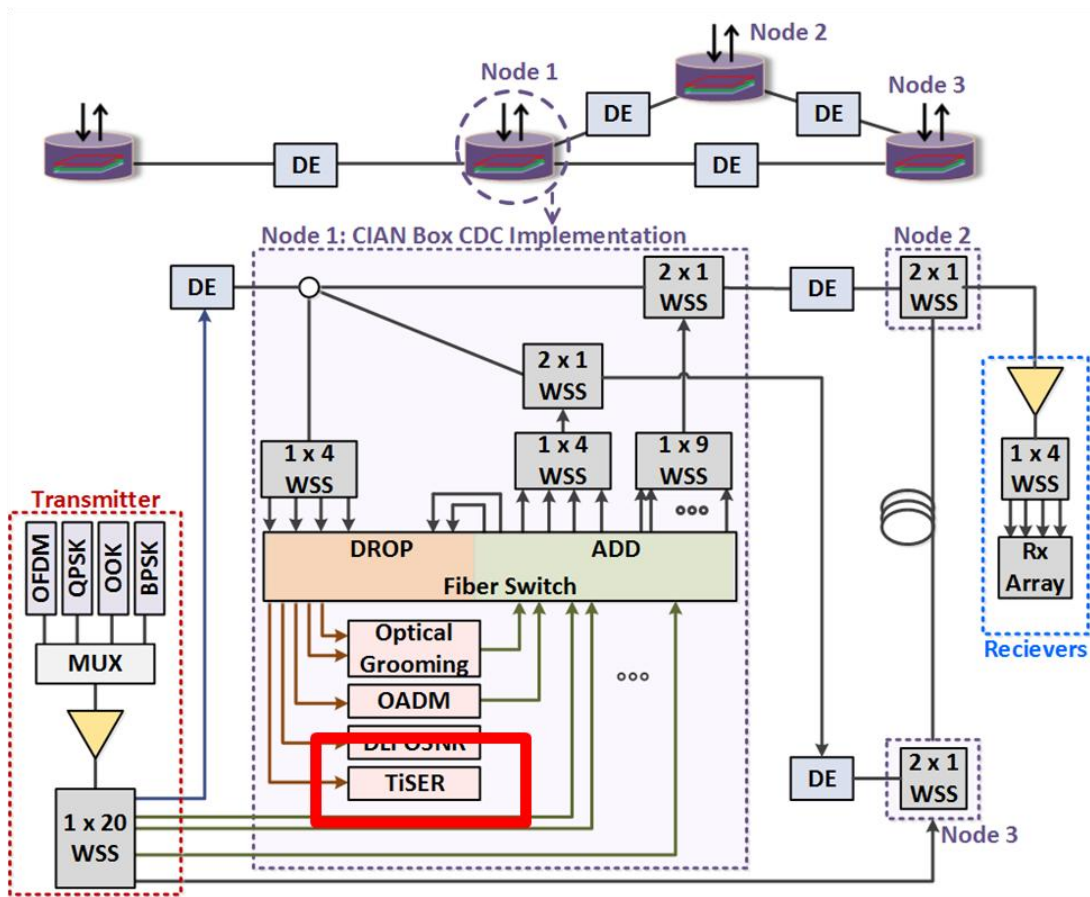
Figure 7.2. The CIAN box architecture where TiSER is inserted into the OPM layer. A

wavelength selective switch drops an optical channel to TiSER to monitor.
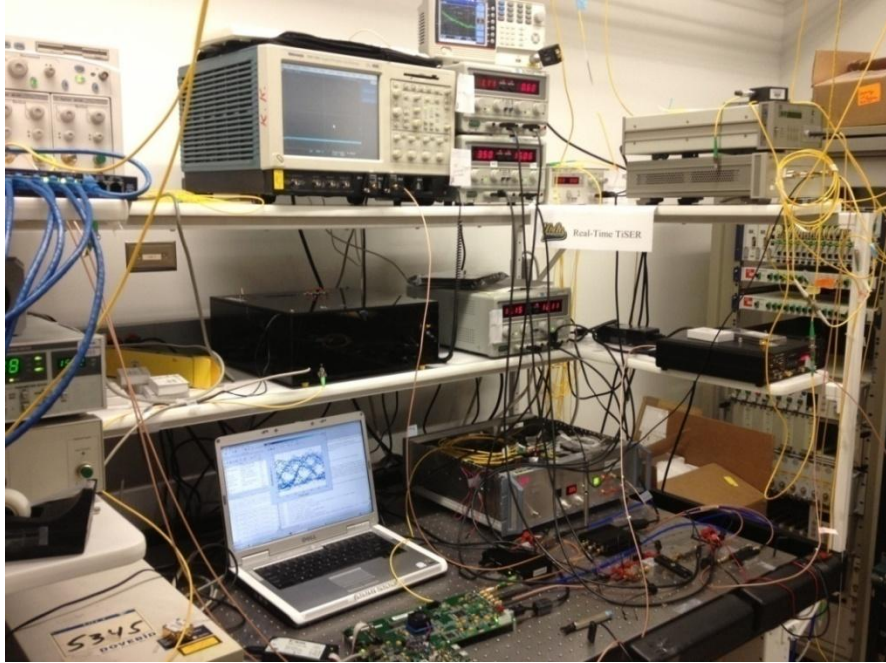
Figure 7.3. Set up of TiSER at CIAN TOAN.
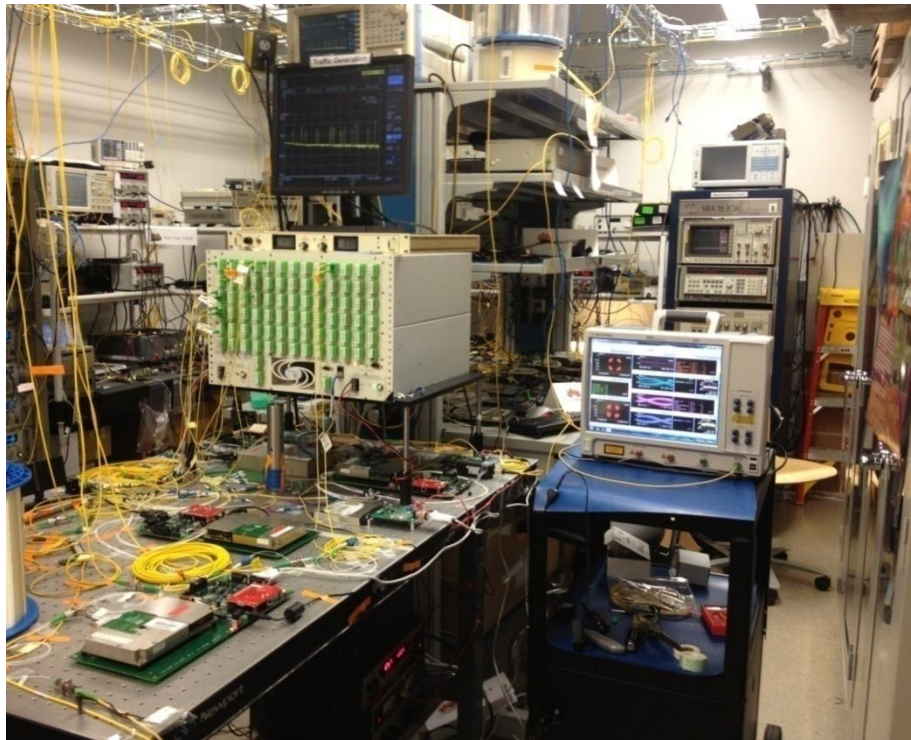
Figure 7.4. CIAN TOAN collaborative effort simulated ability to compensate for impairments in

next generation optical communication networks.

In the CIAN box architecture, TiSER was inserted into the OPM layer as shown in Figure 7.2. A wavelength selective switch would drop an optical wavelength for TiSER to measure. One of the benefits of using a wavelength selective switch is different wavelengths can be sent to TiSER without the need to reconnect fibers, reducing complexity. The optical channel would be sent to a clock and data recovery circuit where the clock and data would be input to TiSER. The clock serves as the timer for eye diagram generation and the eyes can be created from the data. While monitoring, TiSER is capable of producing eye diagrams in real-time and analyze the eye diagram rapidly to estimate BER. The BER values would then be sent to the control plane through XMPP. Pictures of TiSER inserted into TOAN are presented in Figures 7.3 and 7.4.

7.4   Optical Performance Monitoring using TiSER

With TiSER successfully inserted into TOAN and used to generate real-time eye diagrams and estimate signal integrity parameters, TiSER can be used for OPM. To verify the performance of TiSER, the eye diagram produced by TiSER would be compared to the eye generated by a sampling oscilloscope. The BER value was also verified by comparing it to a BERT. It was observed that the BER value is more accurate when more noise is injected into the system compared to when no noise is injected due to the estimation technique used.

In addition to being able to perform signal integrity analysis on the real-time eye diagrams, we were able to observe ASE and SPM effects on the signal. Because TiSER can sample so quickly and generate eye diagrams approximately every 27 μs as opposed to several seconds or minutes with a sampling oscilloscope, these effects could be observed as ASE and SPM was being added into the distance emulators. Furthermore, TiSER was also able to

demonstrate for the first time real-time, in-service monitoring and signal integrity analysis on a commercial platform [99]. A video stream was transmitted by a Fujitsu Flashwave 9500 across an optical network, and TiSER was able monitor this data stream in real-time. During transmission, TiSER was able to generate real-time eye diagrams and rapidly analyze the eye for a corresponding BER value.
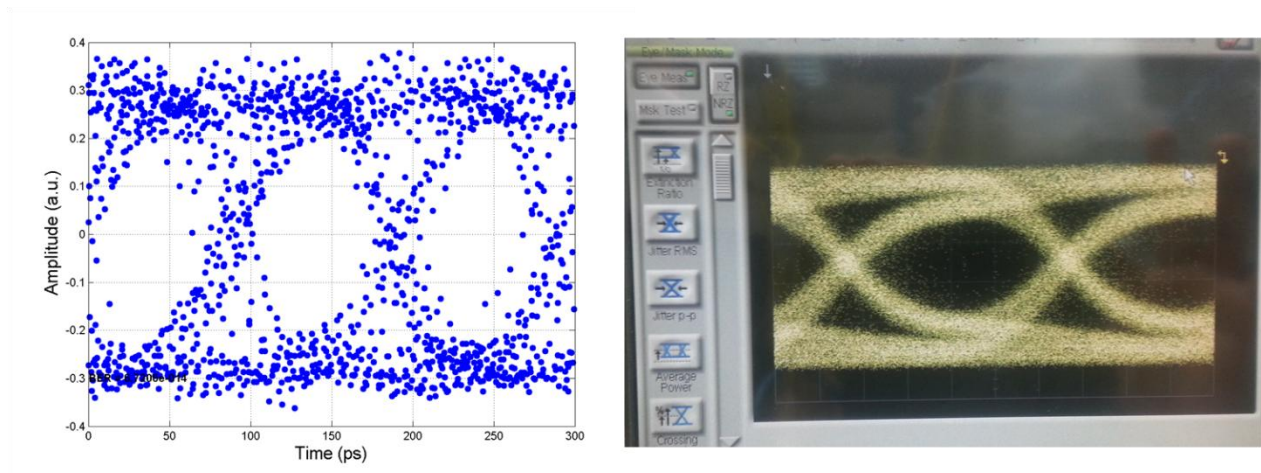
Figure 7.5. (Left) TiSER generated eye diagram and (right) sampling oscilloscope generated eyes for the 10 Gbit/s video UDP packets with stretch factor of 50. TiSER is able to generate eyes in 27 μs as opposed to many seconds or minutes using the sampling oscilloscope [99].

7.5 Conclusions

Next generation optical networks need real-time OPM that can relay information about the health of the network quickly, and TiSER is a solution that can be used. TiSER can be used to monitor the signal integrity along the transmission line, provide feedback to optimize optical devices or along the transmission line, and the rapid feedback will enable system management to detect optical link failures. This section has highlighted many features in TiSER that make it an attractive platform for OPM applications. These include real-time eye diagram generation and analysis, the ability to capture time-traces whereas sampling oscilloscopes cannot, and the ability to capture transients with its high temporal resolution that would otherwise be missed by conventional electronic digitizers.

Chapter 8

Concluding Remarks

Several new developments have been presented that improve the linearity of optical links and enable high speed measurements on ultra-fast signals. A digital broadband linearization algorithm is developed and used to linearize optical links by reducing intermodulation products and experimentally demonstrating a record 120 dB.Hz$^{2/3}$ SFDR across 6 GHz of bandwidth. This algorithm, currently realized for offline processing, could be implemented into real-time. The architecture for the real-time implementation of this algorithm on a FPGA was designed, and a Matlab simulation of the real-time implementation matches well with the Verilog simulation showing proof of concept.

An ultra-wideband instantaneous frequency estimator termed time-stretch instantaneous frequency measurement receiver (TS-IFM) was demonstrated. By combining both time-stretch and windowing and quadratic interpolation, the TS-IFM capable of rapidly sweeping across ultra-wide bandwidths and measuring the frequency of signals with higher accuracy was achieved. Moreover, the TS-IFM has the capability to measure multiple frequencies simultaneously whereas current IFM can only measure one signal at a time as long as it is within

hardware and software capabilities. The TS-IFM is able to improve on many weaknesses exhibited by many current IFM receivers.

Lastly, results were presented from experiments highlighting the impact of TiSER in telecommunication applications. TiSER is capable of analyzing eye diagrams and performing rapid signal integrity measurements of high speed signals. TiSER is able to quickly measure rise and fall times, bit error rate, and jitter, and it can be expanded to measure other performance parameters are well. The analysis program was integrated into the backend of real-time TiSER and was used during our collaboration effort when TiSER was inserted into CIAN TOAN. From our collaboration, we demonstrated that TiSER can be used as an optical performance monitor for next generation agile networks.

Appendix A: Real-time Simulation of Digital Broadband Linearization Technique

In this appendix, a detailed description of the overall architecture and blocks for real-time simulation of the digital broadband linearization technique will be discussed.

9.1 Digital Broadband Linearization Technique Architecture
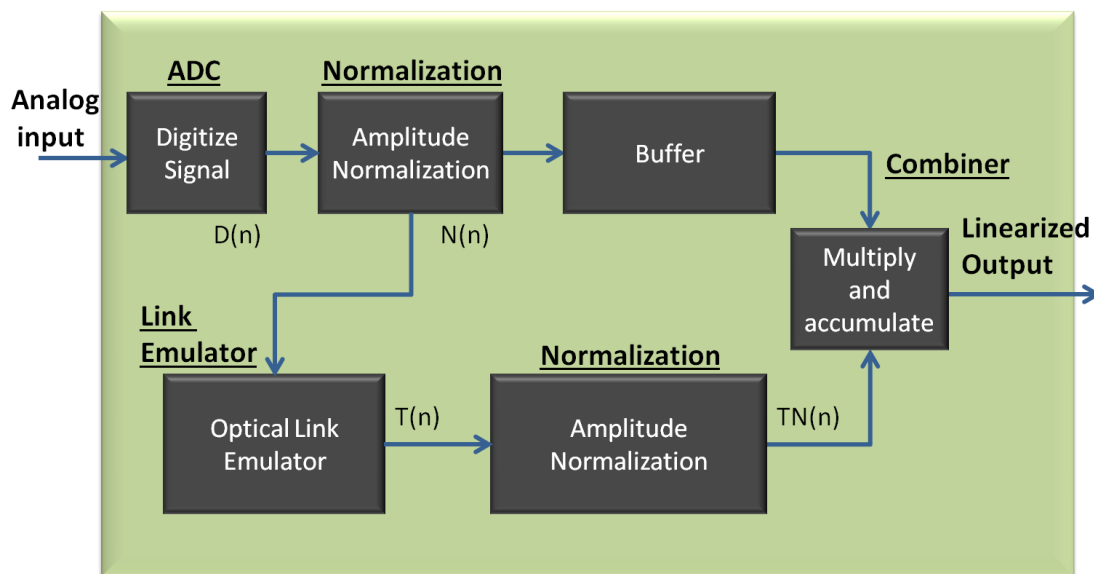
Figure 9.1. Block diagram of the architecture for digital broadband linearization technique.

Figure 9.1 shows the general architecture used to implement the digital broadband linearization technique. The ADC digitizes the signal, the normalization block will perform amplitude normalization on the sampled signal, the link emulator emulates the optical link, and the buffer holds the data in memory for a number of clock cycles before it reaches the multiply and accumulate block. There are two data paths after the first normalization block and they

recombine at the multiply and accumulate block where the output is the linearized output with nonlinearities removed. The architecture is designed to be used on a SP Devices TIGER 108 (ADQ108). The ADQ108 is an 8-bit ultra-high speed digitizer with a sampling rate of 7 GSamples/s enabled by SP Devices ADC interleaving technology. The acquisition bandwidth is 2 GHz. The digitizer has a four channel input which can collect 32 samples per clock cycle. The four channels are labeled from A to D, and each sample is 1 byte in size, and the samples are arranged as shown in Figure 9.2.

Channel	[63:56]	[55:48]	[47:40]	[39:32]	[31:24]	[23:16]	[15:8]	[7:0]
C	25	29	17	21	9	13	1	5
A	26	30	18	22	10	14	2	6
D	27	31	19	23	11	15	3	7
B	28	32	20	24	12	16	4	8

Figure 9.2. The four input channels of the ADQ108 with the order of the samples along with the size of each sample in bits.

9.1.1 Detailed Architecture

The sizes of the input and outputs that are passed to each block in the architecture is shown in Figure 9.3 below. There are four buffers that hold the data from each clock cycle and transfer them to the next block. The Y Axis shift and second normalization blocks have 80 bit buffers instead of 64 bit buffers due to the Cordic block that does a cosine operation. The output is 10

bits per sample, thus the buffer size is increased to 80 bits. By using a larger number of bits, we

can increase the precision as well for other math operations. When converting back from 10 bits

to 8 bits, the samples are truncated.

For each of the main blocks, the Verilog support files are listed. Many of these support

files are generic files that can be generated by Xilinx CORE generator. These are the

Add_sub.v, Div_gen_v3_0.v, Cordic.v, and Multi.v files. The other files are custom code written

for this application.
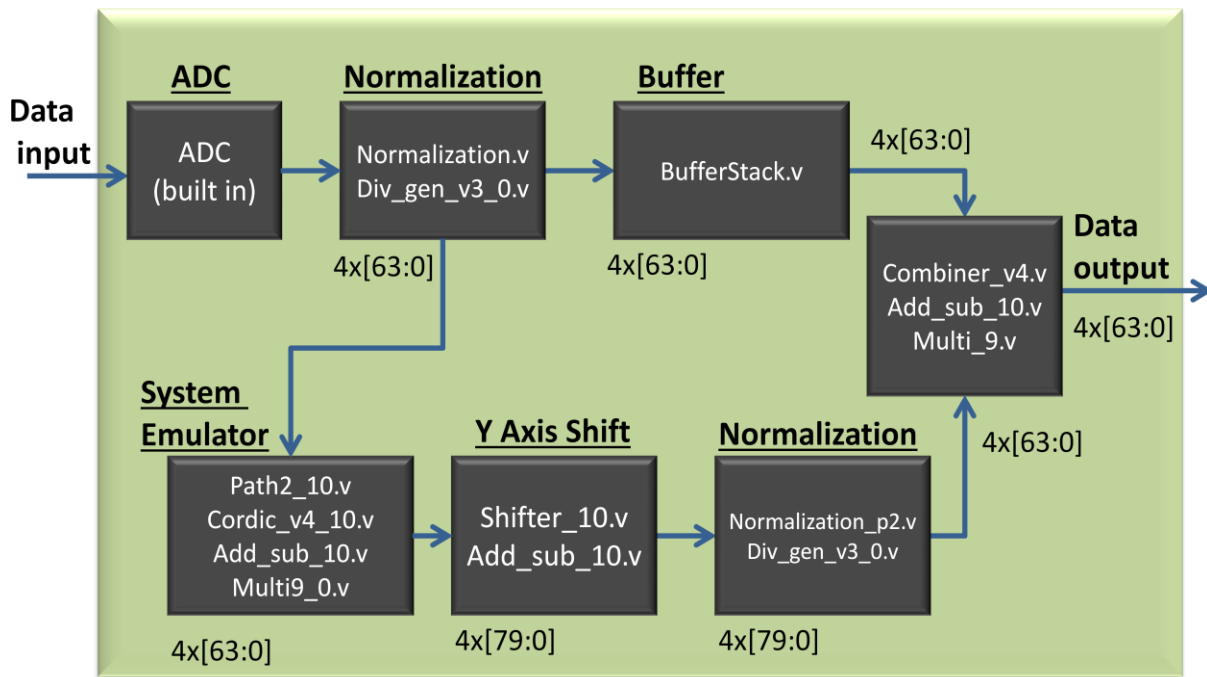
Figure 9.3. The bit size inputs to each block of the architecture.

9.1.2 Normalization Block

The normalization block diagram is shown in Figure 9.4. Each block represents one clock cycle.

At the input, 32 data samples are collected each clock cycle. The absolute value of each sample

point is taken which means that if the 8th bit is a 1, then the result will be the two's complement

111

plus one to make it a positive number. At the same time, the largest value is found and saved to memory. This is repeated for four clock cycles where the largest value from four clock cycles is used to normalize data points. This value is moved to the big value (BV) block where it will be the divisor for four clock cycles. After four clock cycles, 128 samples are normalized and outputted.
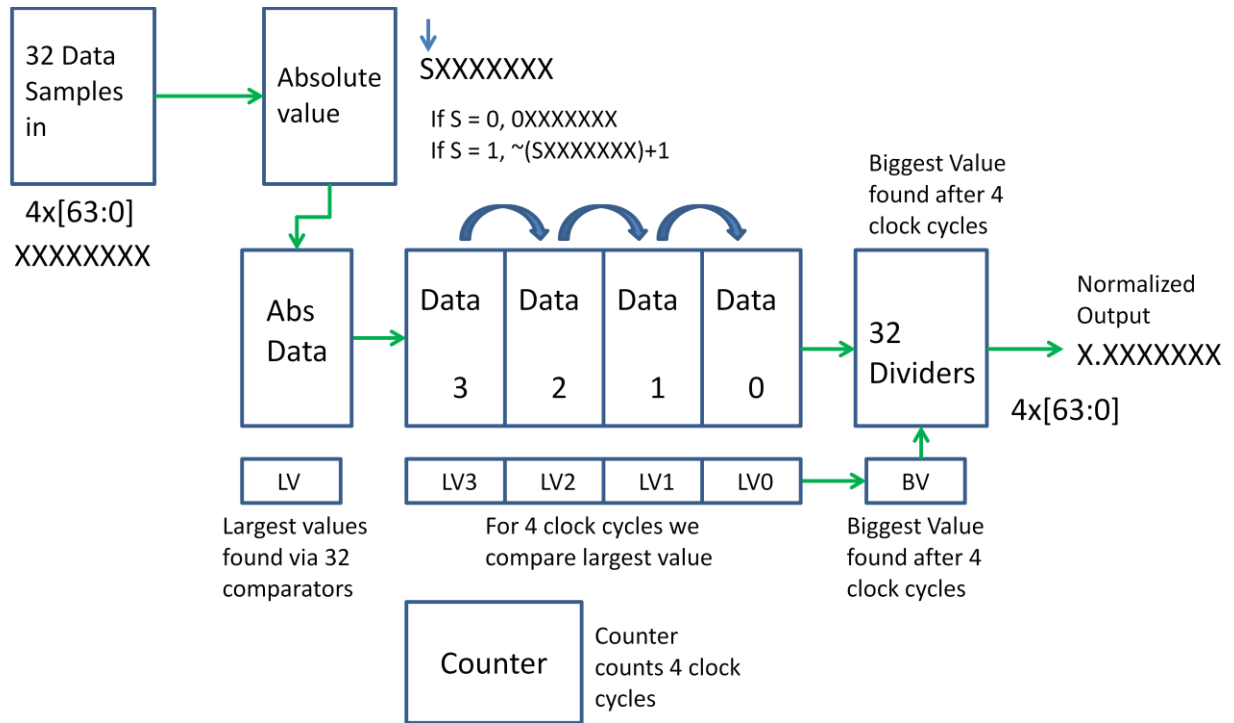
Figure 9.4. Normalization block diagram. This shows how every 128 sample points are normalized at a time.
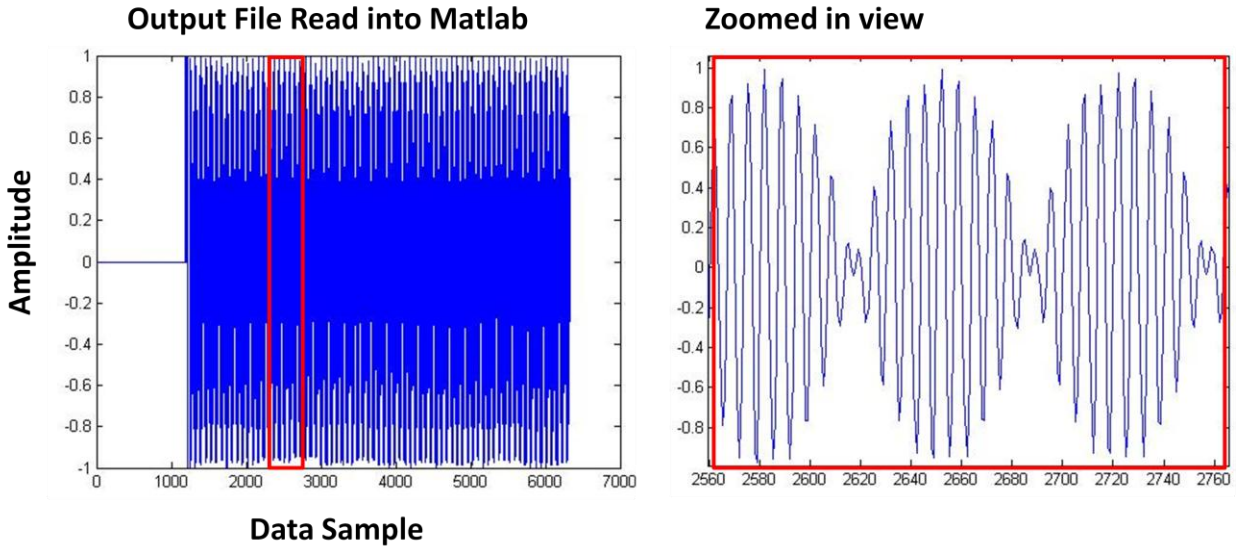
Figure 9.5. Verification in simulation of the normalization block. It can be seen that the signal is

normalized as shown by the plot on the right.

The normalization block appears to be working after checking the output text file. The first set of

points at 0 is from the block initialization which can be removed by setting a trigger for the block

as shown in Figure 9.5. However, this block does not work on the ADQ108 system. This is

probably due to some timing error in the code.

9.1.3   Buffer Block

After the first normalization block the data is divided into two paths which combine at a later

point. The buffer block stores all the sample points for several clock cycles until the data points

are ready to be recombined. The buffer stores 32 sample points for 53 clock cycles in this design.

For each clock cycle, the data points are moved to the next buffer level. To determine the

number of buffer levels, a flag was put into the system which allowed me to adjust the number of

buffer layers until all the data points lined up at the correct clock cycle as shown in Figure 9.7.

113
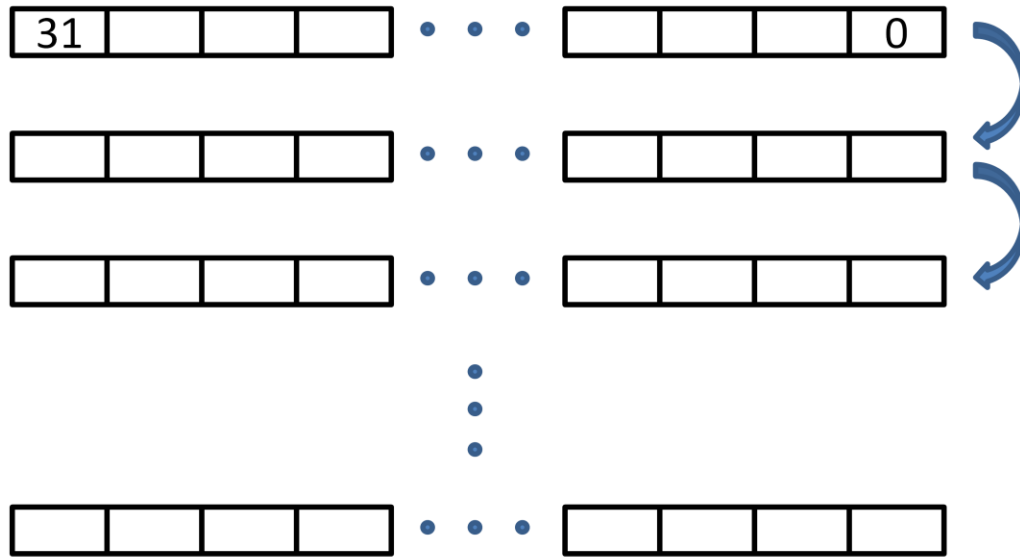
Figure 9.6. Buffer block diagram where 32 sample points are stored and shifted to each buffer level at each clock cycle.
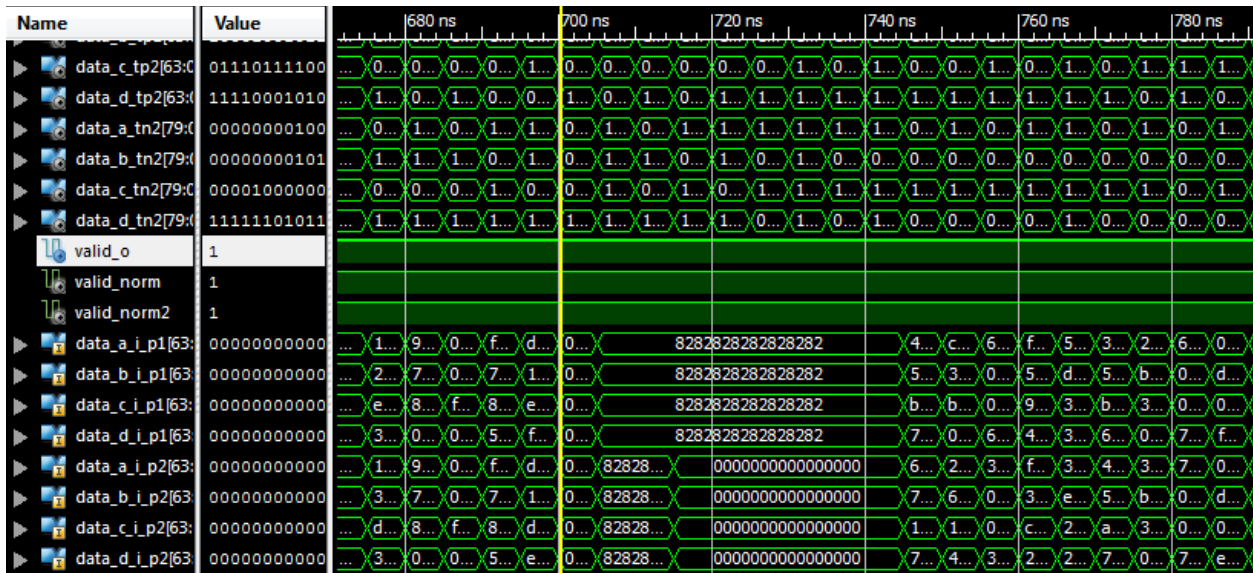
Figure 9.7. Determining the number of buffer levels by lining up the data points.

9.1.4 System Emulator Block

The details of the system emulator block are shown in Figure 9.8, and it utilizes Cordic, add_sub, and multiplication blocks. In each stage of this block, we can see how the bit size changes and which bits are utilized for the next stage. In this block, the equation is $Output = \cos^2\left(0.5\ V_{in} - \frac{\pi}{4}\right)$. The Cordic block performs the cosine operation but requires a ten bit input. The output from the Cordic is shown and the result is squared. The resulting output is twenty bits long and the bits of interest extracted are colored in blue.
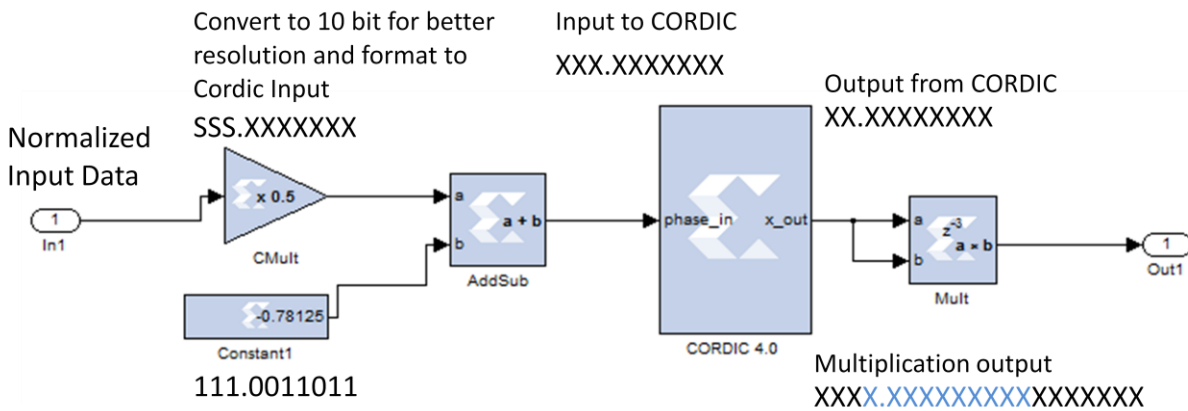
Figure 9.8. The block diagram for the system emulator.

9.1.5 Y Axis Shift Block

This block shifts the data so that it is centered on the Y axis. Similar to the normalization block, this block normalizes all the data, finds the largest and smallest values, finds the median value and shifts the data so that it is centered around y = 0.
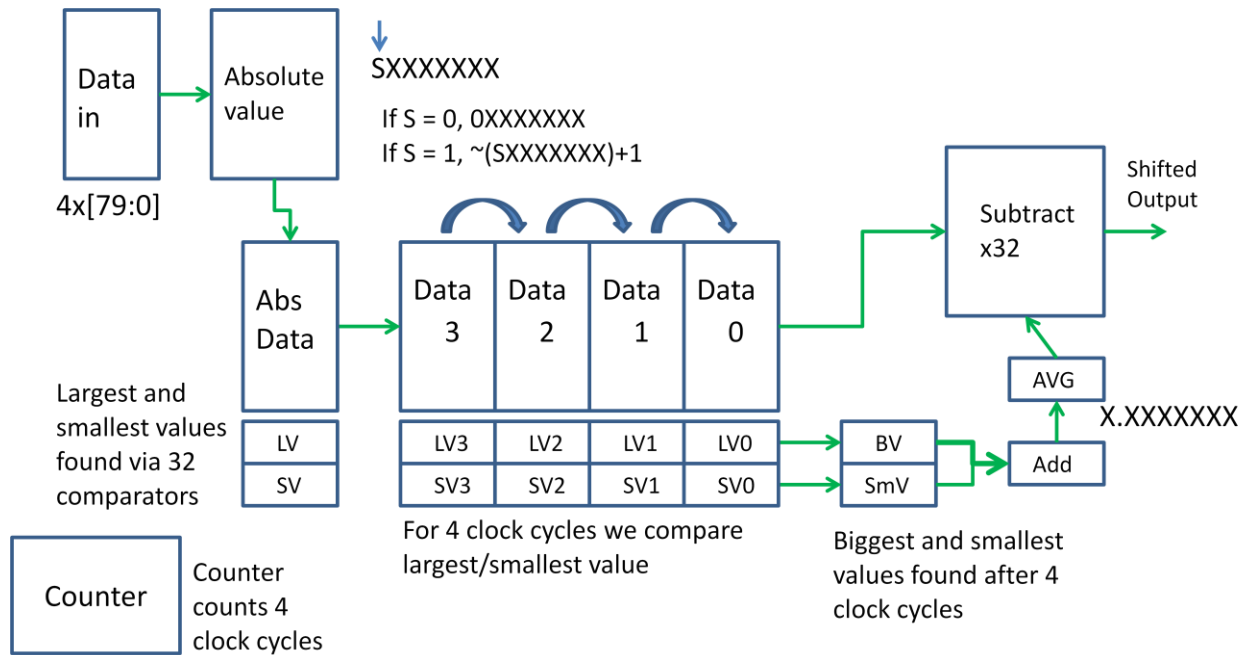
Figure 9.9. Block diagram for the Y-shifter block. This block finds the max and min values in a data set and shifts all the values by the median value.

9.1.6   Multiply and Accumulate Block

This block combines the two data paths from the buffer block and from the optical link emulator. In each path a constant is multiplied to each path. In this technique a 2 and -1 are ideally multiplied, but the -1 may need to be optimized. The data points are then multiplied by this constant and added together. The bits of interest are highlighted in blue and taken as the output.
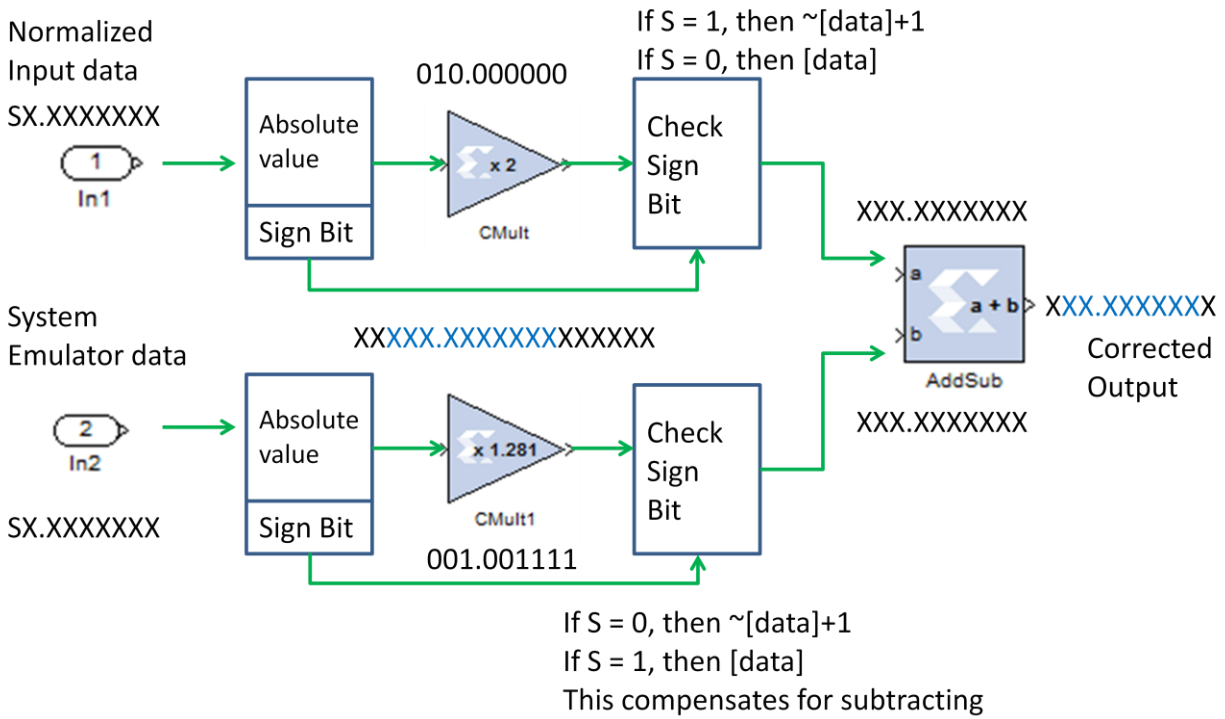
Figure 9.10. Multiply and accumulate block that combines the two data paths and produces the

corrected output.

Appendix B: Extracting Data from TiSER

This appendix will describe how to extract data from TiSER. For all output files obtained prior to 2014, the mode locked pulses containing modulated data had to be manually aligned in time. This meant manually adjusting the timing until all the pulses lined up on top of each other which was very tedious and time consuming. Afterwards, a function was built into the TiSER FPGA to calculate the laser repetition rate, and by using this value, we could then automatically line up the pulses.

10.1 Overlaying Pulses from TiSER

An output file from TiSER will show many pulses when plotted. However, the useful information is modulated onto the pulses and this information needs to be extracted. To do this, the frequency of the pulses needs to be modified manually until all the pulses line up on top of each other. This value should be close to the 36.6 MHz mode locked laser frequency used, but it needs to be slightly adjusted otherwise the pulses will not line up. When the pulses are aligned, the resulting image is shown in Figure 10.1. We also calculate the pulse envelope by determining the mean of the pulses. This envelope is shown in blue in Figure 10.1. By dividing out the envelope from the output file, the original data can be demodulated from the pulse.
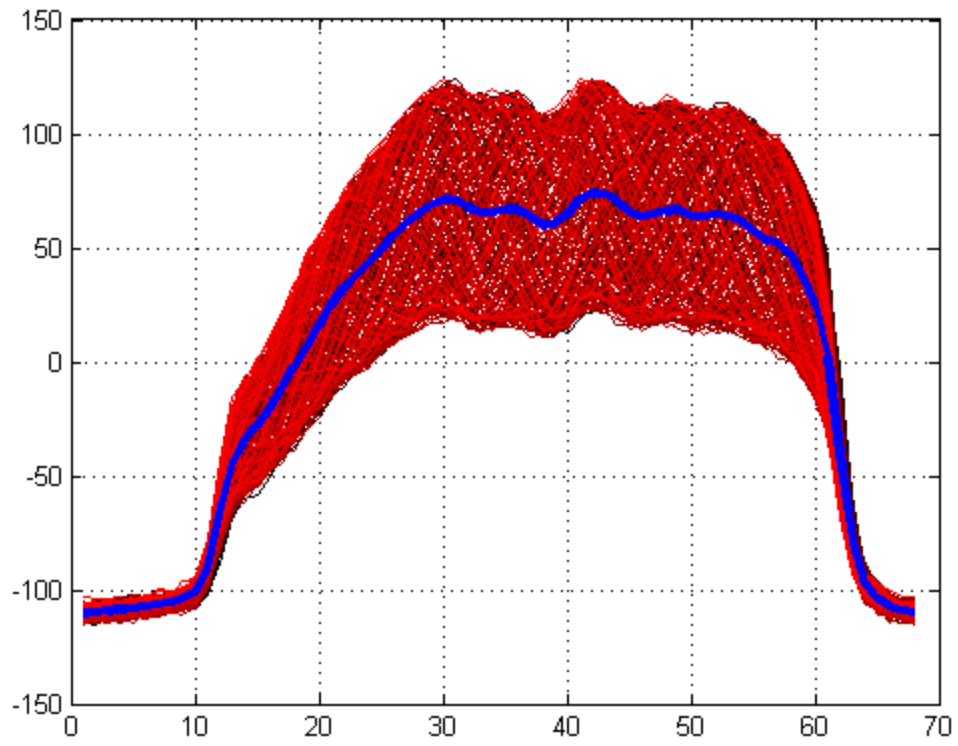
Figure 10.1. Aligned pulses from TiSER and the pulse envelope (blue).

11 References

References

[1]   A. M. Zin, M. S Bongsu, S. M. Idrus, and N. Zulkifli, "An Overview of Radio-over-Fiber Network Technology," *IEEE Conference on Photonics*, pp.1-3, March 26, 2010.

[2]   X. Fernando, "Radio over Fiber- An Optical Technique for Wireless Access" *IEEE Comm. Soc.*, Oct 16, 2009. [Online].
http://cms.comsoc.org/SiteGen/Uploads/Public/Docs_Globecom_2009/XavierROFT16.p df. [Accessed Oct 30, 2014].

[3]   D. Opatic, "Radio over Fiber Technology for Wireless Access," Ericsson Nikola Tesla d.d., [Online]. http://www.ericsson.com/hr/etk/dogadjanja/mipro_2009/12_1112_F.pdf. [Accessed Oct 10, 2014].

[4]   H. Kim, "Radio-over-Fiber Technology for Wireless Communication Services", Samsung Electronics, 2005. [Online].
http://www.tspd.com.tw/images/fbfiles/files/ROF_for_wireless_comm_Hoon_Kim_.pdf. [Accessed Oct 12, 2014].

[5]   Cisco, "Cisco Visual Networking Index: Forecast and Methodology, 2013–2018", Cisco, June 10, 2014. [Online]. http://www.cisco.com/c/en/us/solutions/collateral/service-provider/ip-ngn-ip-next-generation-network/white_paper_c11-481360.html. [Accessed Oct 10, 2014].

[6]   L. Alloatti, et al., "100 GHz Silicon-Organic Hybrid Modulator," *Light Sci. Appl.*, vol. 3, p.e173, 2014. DOI:10.1038/lsa.2014.54

[7]   R. H. Walden, "Analog-to-digital converter survey and analysis," *Selected Areas in Communications, IEEE Journal on*, vol.17, no.4, pp.539-550, Apr 1999.

[8]   R. Walden, "Analog-to-digital conversion in the early twenty-first century," in Wiley Encyclopedia of Computer Science and Engineering (Wiley, 2008), pp. 126–138.

[9]   N. Gray, "Interleaving ADCs for Higher Sampling Rates", Texas Instruments, 2011. [Online]. http://www.ti.com/lit/wp/snaa111/snaa111.pdf. [Accessed Oct 13, 2014].

[10]   A. S. Bhushan, F. Coppinger, and B. Jalali, "Time-stretched analogue-to-digital conversion," *Electronics Letters* vol. 34, no. 9, pp. 839–841, April 1998.

[11]   Y. Han and B. Jalali, "Photonic Time-Stretched Analog-to-Digital Converter: Fundamental Concepts and Practical Considerations," *Journal of Lightwave Technology*, Vol. 21, Issue 12, pp. 3085–3103, Dec. 2003.

[12]   A. Fard, S. Gupta, and B. Jalali, "Photonic time-stretch digitizer and its extension to real-time spectroscopy and imaging," *Laser & Photonics Reviews* vol. 7, no. 2, pp. 207-263, March 2013.

[13]   S. Gupta and B. Jalali, "Time-warp correction and calibration in photonic time-stretch analog-to-digital converter," *Optics Letters* vol. 33, no. 22, 2674–2676, 2008.

[14]   J. Chou, O. Boyraz, D. Solli, and B. Jalali, "Femtosecond real-time single-shot digitizer", *Appl. Phys. Lett.*, vol. 91, no. 16, pp.161105-1 -161105-3 2007.

[15]   K. Goda, et al., "Serial time-encoded amplified imaging for real-time observation of fast dynamic phenomena," *Nature*, vol. 458, pp. 1145-1149. Apr. 2009.

[16]   K. Goda, et al., "High-throughput single-microparticle imaging flow analyzer," *Proc. Natl. Acad. Sci. USA,* vol. 109, pp. 11630-11635. Jun. 2012.

[17]   D. R. Solli, et al., "Optical rogue waves," *Nature*, vol. 450, pp. 1054-1057, Dec 2007.

[18]   E. Diebold, et al., "Digitally synthesized beat frequency multiplexing for submillisecond fluorescence microscopy," *Nature Photonics*, vol. 7, no. 10, pp. 806-810 2013.

[19]   Asad M. Madni and E. J. Nyiri, "Fast Fourier Transform and Digital Filtering Solution to Transmission Line Analysis" *1982 Military MicrowavesConference*, 1982.

[20]   M. K. Carson. *Alexander Graham Bell: Giving Voice To The World*. Sterling Biographies. New York: Sterling Publishing. 2007, pp. 76–78.

[21]   A. G. Bell, "On the Production and Reproduction of Sound by Light". *Am. Jour. of Sci*., vol. Series 3, Vol. 20, no. 118, pp. 305–324. Oct. 1880.

[22]   J. Hecht, *City of Light*, 1999 : Oxford Univ. Press.

[23]   G. P. Agrawal, *Fiber Optic Communication Systems*, 2002 : Wiley.

[24]   J. Hayes, *Fiber Optics Technician's Handbook*, 2006 : Delmar Publishers.

[25]   C. K. Kao and G. Hockham, "Dielectric fiber surface waveguides for optical frequencies", *Proc. IEE*, vol. 113, pp.1151 -1158 1966.

[26]   V. Alwayn. "Fiber-Optic Technologies – A Brief History of Fiber-Optic Communications". Cisco Press. Apr. 23, 2004. [Online]. http://www.ciscopress.com/articles/article.asp?p=170740. [Accessed Oct 14, 2014].

[27]   Transmode, "Transmode's Flexible Optical Network," Transmode, 2014. [Online]. http://www.transmode.com/en/technologies/flexible-optical-networks. [Accessed Oct 14, 2014].

[28]   S. Perrin, "The need for next generation ROADM networks," Heavy Reading, White

        Paper, Sep. 2012.

[29]   D. C. Kilper, et al., "Optical Performance Monitoring", *IEEE/OSA J. Lightwave Tech.*,

        vol. 22, no. 1, pp.294 -304 2004.

[30]   G. C. Valley, "Photonic analog-to-digital converters", *Opt. Exp.*, vol. 15, no. 5,

        pp.1955 -1982 2007.

[31]   C. H. Cox, III, *Analog Optical Links*, 2004: Cambridge University Press.

[32]   D. Lam, A. M. Fard, B. Buckley, and B. Jalali, "Digital broadband linearization of optical

        links", *Opt. Lett.*, vol. 38, no. 4, pp.446-448 2013.

[33]   D. Hall, "Understanding intermodulation distortion measurements," National

        Instruments, Oct 9, 2013. [Online].

        http://electronicdesign.com/communications/understanding-intermodulation-distortion-

        measurements. [Accessed Oct 15, 2014].

[34]   C. Henn, "Intermodulation Distortion (IMD)," Burr-Brown, Apr. 1993. [Online].

        http://www.ti.com/lit/an/sboa077/sboa077.pdf. [Accessed Oct 15, 2014].

[35]   B. Jasper, "IP3 (3rd Order Intercept)," TestEdge, [Online]. testedgeinc.com. [Accessed

        2012].

[36]   G. C. Valley, G. A. Sefler, J. Chou, and B. Jalali, "Continuous time realization of time-

        stretch ADC", *Dig. Tech. Papers Microw. Photon.*, pp.1-3 2006.

[37]   J. Chou, G. A. Sefler, J. Conway, G. C. Valley, and B. Jalali, "4-channel continuous-time

        77 GSa/s ADC using photonic bandwidth compression", *Proc. IEEE Int. Top. Meet.*

        Microw. Photon., pp.54 -57 2007.

[38] Y. Han, O. Boyraz, and B. Jalali, "Ultrawide-band photonic time-stretch A/D converter employing phase diversity", *J. Lightw. Technol.*, vol. 53, no. 4, pp.1404 -1408 2005.

[39] A. Tarighat, S. Gupta, A. H. Sayed, and B. Jalali, "Two-Dimensional Spatio-Temporal Signal Processing for Dispersion Compensation in Time-Stretched ADC," *J. Lightwave Technol.* 25, 1580-1587 (2007).

[40] R. N. Bracewell, *The Fourier Transform and Its Applications (3rd ed.)*, 2000: McGraw-Hill.

[41] D. L. Jones, "Spectrum Analysis using the Discrete Fourier Transform," OpenTax-CNX module, 2014. [Online]. http://cnx.org/contents/e23c86ab-f737-49e3-9e6a-f47172e3f688@6/Spectrum_Analysis_Using_the_Di. [Accessed Oct 16, 2014].

[42] F. J. Harris, "On the use of windows for harmonic analysis with the DFT", *Proc. IEEE*, vol. 66, pp. 51-83 1978.

[43] D. Lam, A. Fard and B. Jalali, "Digital broadband linearization of analog optical links", *Proc. IEEE Photon. Conf.*, pp.370-371 2012.

[44] J. Capmany and D. Novak, "Microwave photonics combines two worlds", *Nat. Photon.*, vol. 1, pp.319 -330 2007.

[45] A. J. Seeds, "Microwave photonics", *IEEE Trans. Microw. Theory Tech.*, vol. 50, no. 3, pp.877 -887 2002.

[46] W.S. Chang, *RF Photonic Technology in Optical Fiber Links*, 2002: Cambridge Univ. Press.

[47] T. E. Darcie and G. E. Bodeep "Lightwave subcarrier CATV transmission systems", *IEEE Trans. Microwave Theory Tech.*, vol. 38, pp.524 -533 1990.

[48]   C. H. Cox, "Gain and noise figure in analogue fiber-optic links", *Inst. Elec. Eng. Proc. J.*, vol. 139, no. 4, pp.238 -242 1992.

[49]   C. Cox III, E. Ackerman, R. Helkey, and G. Betts, "Techniques and performance of intensity modulation direct detection analog optical links", *IEEE Trans. Microwave Theory Tech.*, vol. 45, pp.1375 -1383 1997.

[50]   C. H. Cox III, E. I. Ackerman, G. E. Betts, and J. L. Prince, "Limits on the performance of RF-over-fiber links and their impact on device design", *IEEE Trans. Microw. Theory Tech.*, vol. 54, no. 2, pp.906 -919 2006.

[51]   Y. Takahashi, K. Nagano, and Y. Takasaki, "Optical receiver for VHF multichannel video transmission", *IEEE J. Sel. Areas Commun.,* vol. 8, no. 7, pp.1382 -1386 1990.

[52]   G. Betts, "Linearized modulator for suboctave-bandpass optical analog links*", IEEE Trans. Microwave Theory Tech.*, vol. 42, pp.2642 -2649 1994.

[53]   E. I. Ackerman, "Broad-band linearization of a Mach Zehnder electro-optic modulator", *IEEE Trans. Microw. Theory Tech.*, vol. 47, no. 12, pp.2271 -2279 1999.

[54]   H. F. Chou, A. Ramaswamy, D. Zibar, L. A. Johansson, J. E. Bowers, M. Rodwell, and L. A. Coldren, "High-linearity coherent receiver with feedback", *IEEE Photon. Technol. Lett.*, vol. 19, no. 12, pp.940 -942 2007.

[55]   R. Sadhwani and B. Jalali, "Adaptive CMOS predistortion linearizer for fiber-optic links", *J. Lightw. Technol.*, vol. 21, no. 12, pp.3180 -3193 2003.

[56]   A. R. Shah and B. Jalali, "Adaptive equalisation for broadband predistortion linearisation of optical transmitters", *Proc. IEEE—Optoelectron.*, vol. 152, pp.16 -32 2005.

[57]   J. Chou, et al. "Adaptive optical post distortion linearization," *Optics Express*, vol. 13, no. 15, pp. 5711-5718, July 2005.

[58]   A. Karim and J. Devenport, "Noise figure reduction in externally modulated analog fiber-optic links", *IEEE Photon. Technol. Lett.*, vol. 19, no. 5, pp.312 -314 2007.

[59]   P. Juodawlkis, J. Twitchell, G. Betts, J. Hargreaves, R. Younger, J. Wasserman, F. O'Donnell, K. Ray, and R. Williamson, "Optically Sampled Analog-to-Digital Converters," *IEEE Trans. Microw. Theory Tech.*, vol. 49, no. 10, pp.1840 -1853 2001.

[60]   A. Fard, S. Gupta, and B. Jalali, "Digital broadband linearization technique and its application to photonic time-stretch analog-to-digital converter," Opt. Lett. , vol. 36, pp. 1077-1079, Mar. 2011.

[61]   A. Lab Systems LTD., "AFL-500 Analog Fiber Optic Link," 2006. [Online]. http://www.lab-systems.com/products/fib-opt/afl500/index.html. [Accessed Dec 2012].

[62]   Photonic Systems, Inc., "PSI-1600-10L Series," 2011. [Online]. http://www.photonicsinc.com/1600_10L_series.html. [Accessed Dec 2012].

[63]   Optical Zonu, "RF over Fiber Optic Link," 2013. [Online]. http://www.opticalzonu.com/rfofproducts/standalone/oz1606. [Accessed Dec 2012].

[64]   Y. Li and P. Herczfeld., "Coherent PM Optical Link Employing ACP-PPLL," J. Lightwave Technol., vol. 27, no. 9, pp. 1086-1094 2009.

[65]   Xilinx, "What is a FPGA?" 2014. [Online]. http://www.xilinx.com/fpga/index.htm. [Accessed Oct 20, 2014].

[66]   Altera, "FPGAs," 2014. [Online]. http://www.altera.com/products/fpga.html. [Accessed Oct 20, 2014].

[67]   Z. Que et al, "Implementing Medical CT algorithms on stand-alone FPGA based systems using an efficient workflow with SysGen and Simulink," 10th International IEEE Conference on Computer and Information Technology (CIT), pp.2391-2396, 2010.

[68]   Mathworks, "FPGA Design and Codesign," 2014. [Online].

         http://www.mathworks.com/fpga-design/simulink-with-xilinx-system-generator-for-

         dsp.html. [Accessed Oct 20, 2014].

[69]   W. B. Sullivan, "Instantaneous Frequency Measurement Receivers for Maritime Patrol,"

         Jour. of Electronic Defense, vol. 25, no. 10, pp. 55, Oct. 2002.

[70]   W. B. Sullivan, "Simultaneous Signal Errors in Wideband IFM Receivers," *Microw.*

         Jour., vol. 38, no. 9, Sept. 1995.

[71]   H. Gruchala and M. Czyzewski, "The instantaneous frequency measurement receiver in

         the complex electromagnetic environment," *MIKON-2004.*, Warsaw, Poland, 2004, pp.

         155-158.

[72]   H. Emami, et al., "Amplitude independent RF instantaneous frequency measurement

         system using photonic Hilbert transform," *Opt. Exp.,* vol. 16, no. 18, pp. 13707-13710.

         Sept. 2008.

[73]   PK Avionics GmbH, "Digital receiver technology for RWR, ESM and ELINT

         applications." March 1, 2014. [Online]. www.pk-avionics.ch/ppt/ghz.pdf. [Accessed Oct

         30, 2014].

[74]   Fields, T.W.; Sharpin, D.L.; Tsui, J.B., "Digital channelized IFM receiver," Microwave

         Symposium Digest, 1994., *IEEE MTT-S International* , vol., no., pp.1667,1670 vol.3, 23-

         27 May 1994.

[75]   Elisra Electronic Systems Ltd., Microwave Division, "A Digital Instantaneous Frequency

         Measurement Receiver," *Microwave Journal*. 1 Mar. 2014. [Online].

         http://www.microwavejournal.com/articles/4772-a-digital-instantaneous-frequency-

         measurement-receiver. [Accessed Jul 20, 2014].

[76]   N. Sarkhosh , H. Emami , L. Bui and A. Mitchell, "Reduced cost photonic instantaneous frequency measurement system", *IEEE Photon. Technol. Lett.*, vol. 20, no. 18, pp.1521 -1523 2009.

[77]   N. Sarkhosh, H. Emami, L. Bui, and A. Mitchell, "Microwave photonic instantaneous frequency measurement with simultaneous parallel operation within a single optical fiber", *Proc. IEEE IMS*, pp.368 -372 2010.

[78]   X. Zou, et al., "Photonic approach for multiple-frequency-component measurement using spectrally sliced incoherent source," *Opt. Lett.*, vol. 35, no. 3, pp. 438-440, Feb. 2010.

[79]   L.V.T. Nguyen, "Microwave Photonic Technique for Frequency Measurement of Simultaneous Signals," *IEEE Photonics Tech. Lett.*, vol.21, no.10, pp.642-644, May 2009.

[80]   B. Buckley, "Ultra-high Throughput Real-time Instruments for Capturing Fast Signals and Rare Events," Ph.D. dissertation, Univ. of Ca., Los Angeles, Los Angeles, CA, 2013.

[81]   Asad M. Madni, "Frequency domain reflectometry and digital signal processing solution to transmission lines/antenna systems analysis," Ph.D. dissertation, Cal. Coast. Univ., Santa Ana, CA, 1987.

[82]   Asad M. Madni and Z. Hornoch, "Microprocessor Based Fault Finder Pinpoints Transmission Line Faults Within Inches…and Within Minutes," *Microwave Journal, Intl Ed.*, vol. 24, no. 11, pp. 49 - 57, Nov. 1981.

[83]   Asad M. Madni and R. B. Windle, "Microprocessor Based Hardware and Digital Signal Processing Algorithm Provide a State-Of-The-Art Approach to Transmission Line/Antenna Systems Analysis," *Proc. 1982 IEEE EMC- S Intl*, 1982.

[84]   Asad M. Madni and L. A. Wan, "Digital Signal Processing Techniques for Transmission Lines/Antenna Systems Analysis," *Proc. AMTA*, pp. 10.1-10.8, Sept. 1983.

[85]   VOPcz, "IFM-Broadband Receiver with Instantaneous Frequency Measurement," 12 Mar. 2014. [Online]. http://www.vop.cz. [Accessed Mar. 2014].

[86]   Wide Band Systems, Inc., "Wide Band Products: Instantaneous Frequency Measurement Receiver Systems (IFM)," 12 Mar. 2014, [Online]. http://www.widebandsystems.com/ifm.html. [Accessed Mar. 2014].

[87]   Mercury Systems, "Frequency Measurement", 12 Mar. 2014. [Online]. http://www.mrcy.com/products/microwave-rf/frequency-measurement/. [Accessed Mar 2014].

[88]   Rockwell Collins, "IFMR-6070 Instantaneous Frequency Measurement Receiver," 12 Mar. 2014. [Online]. https://www.rockwellcollins.com/sitecore/content/Data/Products/EW_and_Intelligence/SIGINT/IFMR-6070_Instantaneous_Frequency_Measurement_Receiver.aspx. [Accessed Mar. 2014].

[89]   S. Gupta and B. Jalali, "Time stretch enhanced recording scope," *Appl. Phys. Lett*., vol. 94, no. 4, pp. 041 105-041 105-3, Jan. 2009

[90]   R. Y. Chen, "Chapter 14: Signal Integrity," [Online]. http://www.csee.umbc.edu/csee/research/vlsi/reports/si_chapter.pdf. [Accessed Oct 2014].

[91]   Tektronix, "Anatomy of an eye diagram," Nov. 22, 2013. [Online]. http://www.tek.com/application-note/anatomy-eye-diagram. [Accessed Mar 2014].

[92]   D. Behera, S. Varshney, S. Srivastava, and S. Tiwari. "Eye Diagram Basics: Reading and applying eye diagrams," Freescale Semiconductor. Dec. 16, 2011. [Online]. http://www.edn.com/design/test-and-measurement/4389368/Eye-Diagram-Basics-Reading-and-applying-eye-diagrams. [Accessed Mar 2014].

[93]   C.C.K. Chan, *Optical Performance Monitoring: Adv Tech for Next-Gen Photonic Networks*, 2010: Academic Press.

[94]   K. Willox, "Q Factor: The Wrong Answer for Service Providers and NEMs," Agilent Technologies. Apr. 25, 2013. [Online]. http://cp.literature.agilent.com/litweb/pdf/5988-8925EN.pdf. [Accessed Oct. 2014].

[95]   J. Hancock, "Jitter--Understanding it, Measuring it, Eliminating it Part 1: Jitter Fundamentals" High Frequency Electronics, Apr. 2004. [Online]. http://www.highfrequencyelectronics.com/Apr04/HFE0404_Hancock.pdf. [Accessed Feb 2014].

[96]   National Instruments, "Understanding and Characterizing Timing Jitter", National Instruments. Apr. 17, 2013. [Online]. http://www.ni.com/white-paper/14227/en/. [Accessed Feb 2014].

[97]   Agilent Technologies, "Understanding Jitter and Wander Measurements and Standards," Agilent Technologies. Feb. 1, 2013. [Online]. http://cp.literature.agilent.com/litweb/pdf/5988-6254EN.pdf. [Accessed Oct 2014].

[98]   W. S. Levine, *The control handbook*, 1996: CRC Press, p. 1548.

[99]   C. K. Lonappan, B. Buckley, J. Adam, D. Lam, A. M. Madni, and B. Jalali, "Time-Stretch Accelerated Processor for Real-time, In-service, Signal Analysis," *IEEE Conference on Signal and Information Processing*, December 3-5, 2014.

[100]   Center for Integrated Access Networks, "Center for Integrated Access Networks," 2014. [Online]. http://cian-erc.org/. [Accessed Oct 2014].

[101]   Z. Q. Pan, C. Y. Yu, and A. E. Willner, "Optical performance monitoring for the next generation optical communication networks", *Opt. Fiber Technol.*, vol. 16, pp.20 -45 2010.